論文 / 著書情報
Article / Book Information

題目(和文)	
Title(English)	Exploration of shallow S-wave velocity profile in Bandung basin, Indonesia, using surface-wave phase velocity and microtremor horizontal-to-vertical ratio with linear velocity increase assumption
著者(和文)	AndiMuhamaPramatadie
Author(English)	Andi Muhamad Pramatadie
出典(和文)	学位:博士(学術), 学位授与機関:東京工業大学, 報告番号:甲第12141号, 授与年月日:2021年11月30日, 学位の種別:課程博士, 審査員:山中 浩明,淺輪 貴史,中村 恭志,海江田 秀志,盛川 仁,松岡 昌志
Citation(English)	Degree:Doctor (Academic), Conferring organization: Tokyo Institute of Technology, Report number:甲第12141号, Conferred date:2021/11/30, Degree Type:Course doctor, Examiner:,,,,,
学位種別(和文)	博士論文
Type(English)	Doctoral Thesis

Exploration of shallow S-wave velocity profile in Bandung basin, Indonesia, using surface-wave phase velocity and microtremor horizontal-to-vertical ratio with linear velocity increase assumption

A doctoral thesis presented by

Andi Muhamad Pramatadie

Supervised by

Prof. Hiroaki Yamanaka

Department of Environmental Science and Technology

Tokyo Institute of Technology

November 2021

Acknowledgment

First, I wish to express my sincere appreciation to my supervisor, *Professor Hiroaki Yamanaka* at Department of Environmental Science and Technology, Tokyo Institute of Technology, who convincingly guided and encouraged me throughout my study. Without his persistent help, the goal of the study would not have been realized.

I am deeply thankful to Ph.D. thesis reviewers, *Professor Hitoshi Morikawa*, *Professor Masashi Matsuoka, Professor Takashi Asawa, Professor Takashi Nakamura* from Tokyo Institute of Technology, and also *Professor Hideshi Kaieda* from Central Research Institute of Electric Power Industry Japan, for their insightful comment and suggestions.

I am sincerely grateful to the Ministry of Education, Culture, Sports, Science and Technology *(MEXT),* Japan and the Consortium for Socio-Functional Continuity Technology Project (SOFTech) for a generous scholarship during Doctoral student at Tokyo Institute of Technology.

I am deeply grateful to *Assistant Professor Kosuke Chimoto* at Department of Environmental Science and Technology, Tokyo Institute of Technology as a tutor and friend. I am also thank to members of Yamanaka laboratory: *Sorimachi san, Imai san, Nogami san, Tsuchiya san, Hussam san, Mohamed san, Selene san, Ozlem san, Udin san, Saguchi san, Noyori san, Hirose san, Kojima san, Harigaya san, Liu san, Ishihara san, Ishige san, Shimizu san, Tuna san, Miyanaga san, Chujo san, Shinoyama san, Seita san, Yuny san, Kawai san, Muroi san, Watanabe san, Shigehara san, Mitome san, Hashimoto san, Iida san, Kasamatsu san, Miyakoshi san, and Kyuke san* for the togetherness. I also indebted to the secretary, *Shimamoto san* for her kind assistance during my study in Japan.

I am grateful to Railway Technical Research Institute (RTRI) for memorable internship opportunity, especially *Tsuno san* who has always been a tutor both before I became student at Tokyo Institute of Technology, as well as during the internship.

I am grateful to Dr.Afnimar, all the colleagues in Institut Teknologi Bandung (ITB) and Indonesian Student Association in Tokyo Institute of Technology who has supported me during doctoral study. I am also grateful to Dr.Shindy and Mrs.Lika Widiyantoro during discussion about the Bandung basin.

I wish to thank all the people whose assistance was a milestone in the completion of this project. To my beloved father and mother, *Andi Jayalangkara Tanra* and *Andi Mardiah Tahir*, my brother, *Andi Muhamad Primabudi* (Hiro), and my little sister, *Akita Dhianty* for continuous support in my study and life. I am also grateful to my father and mother in law, *Safruddin* and *Nirwana* for their encouragement in my life and education. Finally, I am grateful to my wife, *Nurmala Sari* for kept me going on and believing me that I am able to complete my thesis. Moreover, my son, *Andi Abdullah Al Hanif* as one of the sources of our happiness.

~To all of you, I am eternally grateful~

Abstract

S-wave velocities in the near-surface layers, especially in an earthquake-prone area, become one of important parameters for seismic hazard evaluation. An S-wave velocity profile can quantify the amplification and the resonant frequency of ground motion. This study aims at providing shallow S-wave velocity profiles in the Bandung basin, Indonesia, to characterize the soil amplification features for the seismic hazard evaluation in the basin using a simplified method considering a limited availability of instruments in the area.

The existing methods to estimate an S-wave velocity (Vs) profile are based on observations of the surface-wave phase velocities and microtremor horizontal-to-vertical spectral ratios (H/V). We simplify a profile representation of an estimated profile by a linear function of S-wave velocity, so that the model parameters become only the surface S-wave velocity (V1), the velocity-depth gradient, and the bedrock velocity. In this study, we defined a constant bedrock S-wave velocity with a velocity of 500 m/s. Therefore, an estimation of a Vs profile can be modelled from the V1 and the velocity gradient. In addition to accommodate the limitation of available instruments in Bandung, we propose a method to estimate a profile using H/V data and V1 from field measurements.

The applicability of the proposed method was examined in the numerical tests using soil profiles from the boreholes in the basin and compared the results with the obtained ones from the conventional method. The numerical test results confirm the applicability of the proposed method. The estimated profiles from the proposed method having a good agreement to the borehole profiles with average relative differences around or less than 20% and providing similar results with the profiles obtained using the conventional method.

We then estimated the actual profiles using the conventional and the proposed methods in the Bandung basin by deploying microtremors array measurements and V1-H/V

measurements. We examined the appropriateness of the linear profile representation in the basin from the agreement between the observed phase velocities from the array measurements and the theoretical ones of the estimated profiles from the conventional method. The observed phase velocities from the array measurements show that 23 of 25 sites of the observed phase velocities can be well explained by the theoretical phase velocities using the linear velocity increases. It indicates the appropriateness of the profile representation using the linear function in the Bandung basin. The phase velocity comparison also confirms the suitability of the assumption of the bedrock velocity of 500 m/s. Furthermore, we provided 29 additional S-wave velocity profiles in the basin using the proposed method. Finally, we use the estimated Vs profiles from the array and the V1-H/V measurements for the site characterization of the site amplification in the Bandung basin

The results of applying the methods to the data in the Bandung basin suggest that the time-averaged S-wave velocities in the top 30 m (Vs30) are below 150 m/s at sites located in the lake deposit (the central-eastern part of the basin). The soil amplification factors in the lake deposit region are higher than six at frequencies below 1 Hz, due to the existence of the low velocity layers with thick sediment deposits. Meanwhile, at the sites situated in the volcanic deposit region, especially in the northwestern part of the basin, the site amplification factors are characterized by fundamental peak frequencies of 2 to 8 Hz with amplitudes below six due to the present of the thin sediments with the high velocities layers. Our results of the Vs30s from the field measurements indicate lower values than the previous Vs30 map of the basin by Handayani et al. (2009) that derived from an empirical relation to the surface geology condition. These results also reveal a higher seismic hazard potential in the Bandung basin than the previous study.

Contents

Acknowledgment ii

Abstract iv

Contents vi

List of tables x

List of figures xii

Chapter 1 Introduction 1

1.1 Background of research 2

1.2 Geology and seismicity of Bandung basin 4

1.3 Reviews of previous studies 7

1.3.1 S-wave velocity profiles in Bandung basin 7

1.3.2 Overview of conventional S-wave velocity profile estimations 10

1.3.3 Usage of velocity-depth function for S-wave profile 11

1.4 Objectives of the research 13

1.5 Thesis organization 14

Chapter 2 Methodology 17

2.1 Overview of the proposed method 18

2.2 Profile representation using a linear S-wave velocity function 19

2.3 Examination of linear S-wave velocity representation 19

2.4 Model parameters estimation 20

Chapter 3 Numerical tests 24
3.1 Objective 25
3.2 Borehole profiles in Bandung basin 25
3.3 Synthetic data 29
3.4 Estimated profiles 31
3.4.1 Profile estimation with conventional method 31
3.4.2 Profile estimation with proposed method 32
3.4.3 Comparison of the estimated Vs profiles with the borehole profiles 33
3.5 Discussion 36
3.5.1 Difference in estimated bedrock depths 36
3.5.2 Effects of different bedrock velocities 38
3.5.3 Effects of other velocity functions 40
3.5.4 Effects of random noises in observed data 44
3.6 Investigation of difficult cases in assumption of linear velocity function 48
Chapter 4 Array measurements of microtremors in Bandung basin 56
4.1 Objective 57
4.2 Locations of microtremor arrays 57
4.3 Estimation of phase velocity 60
4.4 Evaluation of linear velocity increase assumption 63
4.5 Estimated Vs profiles 66
Chapter 5 Application of the proposed method for Vs profiles in Bandung basin 68

5.1 Objective 69
5.2 Locations of measurement sites 69
5.3 Implementation of V1-H/V measurements 71
5.3.1 Active seismic measurement for surface S-wave velocity 71
5.3.2 Observation of H/V from single-point microtremor measurements 72
5.4 Results of V1-H/V measurements 73
5.4.1 Observed surface S-wave velocities 73
5.4.2 Determination of velocity gradients from observed H/V peak frequencies 77
5.4.3 Estimated Vs profiles 80
5.5 Discussion 83
5.5.1 Comparison of the estimated profiles from phase velocities with obtained ones from surface S-wave velocity-H/V 83
5.5.2 Effects of instruments reduction on estimation of V1 88
5.5.3 A guidance to apply the proposed method in other area 92
Chapter 6 Site characterization in Bandung basin 94
6.1 Objective 95
6.2 Comparison of amplifications estimated from conventional and proposed methods 95
6.2.1 Vs30s 95
6.2.2 Site amplification factors 96
6.3 Distributions of Vs30 and site amplification factor proxies 98
6.4 Comparison with the previous PGA map 105
Chapter 7 Conclusions and future tasks 111

7.1 Conclusions 112

7.2 Future tasks 114

References 116

List of tables

Table 3.1 Soil type factors of the empirical equation in Eq. 3.1 (Ohta and Goto, 1978).....27

Table 3.2 S-wave velocity profiles of the soil column in the Bandung basin used for the numerical test 28

Table 3.3 Search limit of model parameters in the grid search to obtain the Vs profile based on the phase velocity data 31

Table 3.4 Estimated V1 and b using the conventional method in numerical tests.....31

Table 3.5 Comparison of average S-wave velocity from the surface to the top of the bedrock layer (AVS) between the borehole profile and the estimated Vs profile using the proposed method 38

Table 3.6 R-values between the borehole and the estimated Vs profiles using different bedrock velocities.....40

Table 3.7 Comparison of averaged S-wave velocities from the surface to the top of the bedrock layer of estimated Vs profiles using various velocity-depth functions. 44

Table 3.8 R values distribution from various random noise level on the observed V1 and f0 in Borehole 1. 47

Table 3.9 R values distribution from various random noise level on the observed V1 and f0 in Borehole 2. 47

Table 3.10 R values distribution from various random noise level on the observed V1 and f0 in Borehole 3. 47

Table 3.11 Evaluation of R values between the synthetic and the estimated profiles in difficult cases.....55

Table 4.1 List of site names, coordinates, triangle array side lengths, estimated V1s, estimated gradients, and Vs30s of the microtremor array measurements. 58

Table 5.1 List of site names, coordinates, observed H/V peak frequencies and its standard deviation (stdev), observed V1s, estimated gradients, and Vs30s from V1-H/V measurements. 70

Table 6.1 Comparison of the Vs30s of the Vs profiles estimated using the conventional microtremor array surveys and those estimated by the proposed method. 96

Table 6.2 Comparison of the averaged site amplification factor in a frequency range of 0.4 to 10 Hz of the Vs profiles estimated from the conventional method with those estimated from the proposed method. 98

Table 6.3 Average and standard deviation of the surface S-wave velocities, and several time-averaged S-wave velocities for the measurement points located at each geological unit in the Bandung basin. The analysed time-averaged S-wave velocities consist of the averaged S-wave velocity in the top 30 m, 20 m, 10 m, and 5 m. 103

List of figures

Figure 1.1 Map of tectonic setting and several existing plates in Indonesia (Hall, 2002).....4

Figure 1.2 Topographical map of the Bandung basin. 5

Figure 1.3 Simplified surface geological map of the Bandung basin from modification of Dam and Suparan (1992) 7

Figure 1.4 Schematic North-South cross section of the Bandung basin region, modified from Delinom (2009). 7

Figure 1.5 a) Peak ground acceleration map and b) averaged S-wave velocity at the top 30 m (Vs30) in the previous study by Handayani et al. (2009). 8

Figure 1.6 Rayleigh wave group velocities in the Bandung basin area using ambient noise tomography by Pranata et al. (2019) at period of a) 1 second, and b) 8 second. 9

Figure 1.7 Flowchart of this study 16

Figure 2.1 Flowchart of the proposed method for estimating a Vs profile 18

Figure 2.2 Illustration of the proposed method using a surface S-wave velocity (V1) and a peak frequency of microtremor H/V (f0). 23

Figure 3.1 Locations of the boreholes in the Bandung basin on the surface geological map.. 26

Figure 3.2 Soil columns of boreholes in the Bandung basin.. 26

Figure 3.3 Theoretical phase velocity at a) Borehole 1, b) Borehole 2, and c) Borehole 3....30

Figure 3.4 Ellipticity peak frequencies in a) Borehole 1, b) Borehole 2, and c) Borehole 3... 30

Figure 3.5 Estimation of the surface S-wave velocity (V1) and the velocity gradient (b) in the conventional method using phase velocity data through a grid search procedure at a) Borehole 1, b) Borehole 2, and c) Borehole 3. 32

Figure 3.6 Estimation of the velocity gradient (*b*) at a) Borehole 1, b) Borehole 2, and c) Borehole 3 from an agreement of the peak frequency of the theoretical ellipticity of the estimated profile to the peak frequency of ellipticity of the borehole profile.. 33

Figure 3.7 Profile comparison between the borehole and the estimated profiles at a) Borehole 1, b) Borehole 2, and c) Borehole 3 36

Figure 3.8 Estimation of the velocity gradient from the agreement of theoretical ellipticity peak frequency to the synthetic observed H/V peak frequency using various bedrock velocities at a) Borehole 1, b) Borehole 2, and c) Borehole 3.....39

Figure 3.9 Comparison of estimated Vs profiles using a variation in bedrock velocities. 40

Figure 3.10 Estimation of the velocity gradient at a) Borehole 1, b) Borehole 2, and c) Borehole 3 from the agreement of the peak frequencies between the observed H/V and the theoretical ellipticities using various velocity-depth functions.. 41

Figure 3.11 Comparison of estimated Vs profiles using various velocity-depth functions....43

Figure 3.12 Variation of **a)** V1, and **b)** observed peak frequency of elllipticity using various level of random noise in Borehole 1. 44

Figure 3.13 Estimated profiles in Borehole 1 case by including various random noise in the parameters of **a)** surface S-wave velocity (V1) and **b)** ellipticity‟s peak frequency (f0).....46

Figure 3.14 Synthetic profiles used in numerical tests for investigation of the difficult cases.. 49

Figure 3.15 Fundamental mode of Rayleigh wave ellipticities comparison for the cases of a) two-layer profile with high velocity contrast, b) three-layer profile with velocity increasing with depth, c) three-layer profile containing a thick second layer, d) three-layer profile with velocity inversion in a soft second layer, e) profile

represented by two linear velocity gradients, f) profile represented by the power-law function, and g) profile represented by the exponential function. 52

Figure 3.16 Comparison between the synthetic and the estimated profiles using the proposed method in the cases of a) two-layer profile with high velocity contrast, b) three-layer profile with velocity increasing with depth, c) three-layer profile containing a thick second layer, d) three-layer profile with velocity inversion in a soft second layer, e) profile represented by two linear velocity gradients, f) profile represented by the power-law function, and g) profile represented by the exponential function.. 53

Figure 3.17 Phase velocity comparison for the cases of a) two-layer profile with high velocity contrast, b) three-layer profile with velocity increasing with depth, c) three-layer profile containing a thick second layer, d) three-layer profile with velocity inversion in a soft second layer, e) profile represented by two linear velocity gradients, f) profile represented by the power-law function, and g) profile represented by the exponential function. 54

Figure 4.1 The location of microtremor array measurement on the surface geological map of Bandung basin. 59

Figure 4.2 Example of the array configuration in microtremor observation and a documentation of an array deployment in one of the site.. 60

Figure 4.3 An example of the vertical-component records and obtained SPAC coefficients. 61

Figure 4.4 Observed phase velocities from the microtremor array surveys in the Bandung basin..... 63

Figure 4.5 Phase velocity comparison between the observed phase velocities from the microtremor array survey and the theoretical phase velocity of the lowest misfit model using grid search evaluation. 65

Figure 4.6 Distribution of estimated S-wave velocity profiles in Lines 1 to 5 from microtremor array measurements in the Bandung basin.. 67

Figure 5.1 Location of the active seismic and single-point microtremor (V1-H/V) measurements on the surface geological map of the Bandung Basin. 71

Figure 5.2 Configuration of instruments in short-length active seismic measurement (V1-H/V) consists of seven geophones and a single 3-component seismometer. 73

Figure 5.3 Examples of observed waveforms at a) P2, b) P8, and c) P19 and their corresponding observed phase velocities for estimation of V1 from a short-length active seismic measurement d) P2, e) P8, and f) P19.....75

Figure 5.4 Observed frequency-phase velocity (f-c) spectra and observed Rayleigh wave phase velocities from the short-length active seismic measurements in the basin with the estimated V1s**.**. 77

Figure 5.5 Distribution of observed surface S-wave velocities on the surface geological map of the Bandung basin. 77

Figure 5.6 Observed H/V spectra from single-point microtremor measurements in the Bandung basin for determination of velocity gradient (b).. 80

Figure 5.7 Distribution of a) observed H/V peak frequencies, and b) estimated velocity gradients on the surface geological map of the Bandung basin.. 82

Figure 5.8 Estimated Vs profiles in the Bandung basin from the V1-H/V measurements.. ...83

Figure 5.9 Comparison of estimated profiles using the proposed method (V1-H/V) and the conventional method (microtremor array measurements) at the five similar sites. 86

Figure 5.10 Comparison of phase velocity at the five similar sites.. 87

Figure 5.11 Location of the array and the V1-H/V measurement points at S9.....87

Figure 5.12 Estimated F-K spectra from the recorded waveforms using various number of geophones at **a)** P2, **b)** P14, and **c)** P28 sites. 91

Figure 5.13 F-K spectrum at P2 estimated by using the 3 farthest geophones to the source..91

Figure 5.14 Variation of estimated V1 based on number of geophones.....92

Figure 6.1 Site amplification comparison of estimated profiles from the microtremor array and the V1-H/V measurements at the five similar sites.. 97

Figure 6.2 Distribution map of (a) Vs30, (b) Fundamental peak frequency of the site amplification factor, (c) Fundamental peak amplitude of the site amplification, and (d) Averaged site amplification factor in a frequency range of 0.4 to 10 Hz from all the measurement points in the Bandung basin.. 101

Figure 6.3 Site amplification factor of estimated Vs profile at the array and the V1-H/V measurements in each geological unit in the Bandung basin.. 102

Figure 6.4 Relationship of the surface S-wave velocity, the time-averaged S-wave velocities in the top 5 m, 10 m, 20 m, and 30 m with the average site amplification factor in frequency of 0.4 to 10 Hz at the sites located on **a)** lake deposit, **b)** volcanic deposit, and **c)** old and young volcanic products as represented by circle, filled square, and cross marks, respectively. 104

Figure 6.5 Comparison of Vs30s in this study and the previos study by Handayani et al. (2009).. 106

Figure 6.6 Cross-plot of Vs30 comparison between our result and the previous study by Handayani et al (2009). 106

Figure 6.7 Comparison of the PGA values from our study and the previous study in Handayani et al. (2009).. 110

Figure 6.8 Cross-plot of PGA comparison between our result and provided in Handayani et al (2009). 110

Chapter 1 Introduction

1.1 Background of the research

1.2 Geology and seismicity of Bandung basin

1.3 Reviews of previous studies

1.3.1 S-wave velocity profiles in Bandung basin

1.3.2 Overview of conventional S-wave velocity profile estimations

1.3.3 Usage of velocity-depth function for S-wave profile

1.4 Objectives of the research

1.5 Thesis organization

1.1 Background of research

The assessment of local site effects on seismic ground motions has become one of important steps in earthquake hazard assessment. Several destructive earthquakes in the past have demonstrated that the local site conditions substantially influence the amplitudes and the characteristics of strong ground motion which generated the severe damage (e.g., Tsuda et al., 2006; Zeng, 1996). Lessons learned from the past large earthquakes such as the 1985 Mexico City earthquake and the 1994 Northridge earthquake show that variation of damage area may occur even far from an epicenter of an earthquake due to the presence of shallow soft sediments that could cause an amplification of the ground motion (i.e., local site effect) (Boore, 2003; Glass, 1989; Hauksson et al., 1995). An S-wave velocity profile has been known as one of important parameters for the site amplification of seismic waves during an earthquake (Govindaraju & Bhattacharya, 2012; Quispe et al., 2014; Tsuda et al., 2006). Therefore, the estimation of shallow S-wave velocity profile becomes vital, particularly in earthquake-prone areas.

Indonesia is located in one of the highest seismicity zones in the world due to existences of several plate boundaries as shown in Figure 1.1. The Indo-Australian plate subducted the Sunda plate along the western coast of Sumatra island to the southern part of Java island and ended on the Banda sea that close to Papua island (Katili, 2018). Also, we can observe the two subduction-zones in the northeastern of Indonesia, namely the subduction zone by the Philippine sea plate along the Philippine trench in the northern of Molucca sea, and the subduction of the Caroline plate beneath the Indo-Australia plate in the northern part of Papua island (Hall, 2002). Because of this tectonic setting, the country has experiences of numerous earthquakes, e.g., the 2004 Sumatra earthquake with a moment magnitude (Mw) 9.3 on Sumatera Island, the 2006 Yogyakarta

earthquake (Mw 6.3) in Central Java, and the 2018 Sulawesi earthquake (Mw 7.5) in Central Sulawesi. Based on the earthquake catalog from the United States Geological Survey (USGS, 2020), there were 6961 earthquakes occured in the country with Mws greater than 4.5 in 2010 to 2020. 1598 of them have Mws of 5.0 to 5.9, and 108 events have with Mws of 6.0 to 6.9. 9 events have Mws more than 7.0. The intensities during 298 events were estimated as the Modified Mercalli Intensities (MMI) more than 4, which means that the events generated slight to significant shaking on the surface.

Many big cities in Indonesia including Bandung have high earthquakes hazard as they are located near the plate boundaries and active faults. Bandung is the capital city of West Java province and recognized as the third populous city in the country with a population of around 2.5 million (Bandung City Statistics, 2021). The city is situated on the Bandung basin. The concern of the seismic risk in the city has been raised due to the existence of an active 24 km-long Lembang fault in the northern part of the basin (Afnimar, 2014; Afnimar et al., 2015; Brahmantyo, 2005; Syalsabilla et al., 2020). Since the Bandung basin region is regarded as a national strategic area for business and trade centers, we should consider threads from the seismic hazard for the intensive use of a space in the area (Surahman, 2000). Moreover, Bandung is in the first rank in the National Priority Location for earthquake and ground movement disaster (BNPB, 2014). Thus, the assessment of potential seismic hazards in the Bandung basin becomes more urgent for future urban planning in the country.

As an effort of the seismic hazard assessment for the Bandung basin, it is important to have the basic data on physical models of the subsurface condition especially the S-wave velocity data that control the soil amplification. Therefore, providing the S-wave velocity profiles of the sediments in the basin becomes an essential

task to understand the soil amplification characteristics as efforts of the seismic hazard mitigation in the Bandung basin.

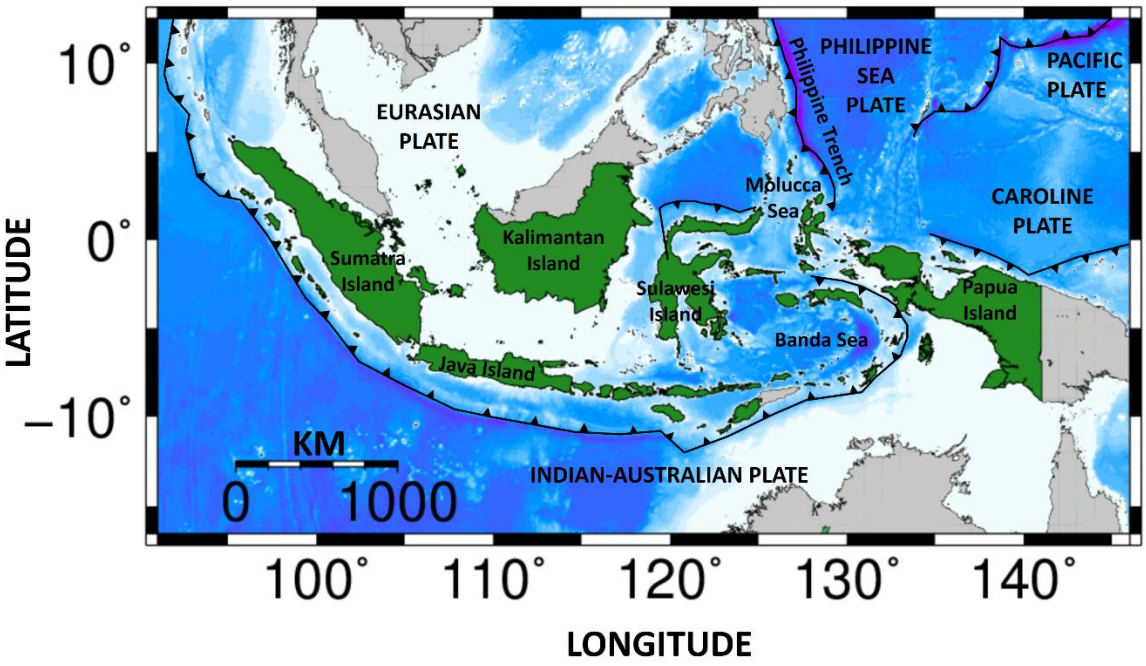

Figure 1.1 Map of tectonic setting and several existing plates in Indonesia (Hall, 2002)

1.2 Geology and seismicity of Bandung basin

The topographical map of the Bandung basin can be shown in Figure 1.2. The basin has a flat elevation of 665 m above the sea level at the center and is surrounded by Late Tertiary and Quaternary volcanic regions, reaching altitudes more than 1000 m (Dam et al., 1996). The Lembang fault is one of the prominent geological features in the area with a clear geomorphological expression of the tectonic activity around the Bandung basin. Geomorphologically, the Lembang fault is formed with a north-facing fault scarp with a slope steeper than 40 degrees (Meilano et al., 2012).

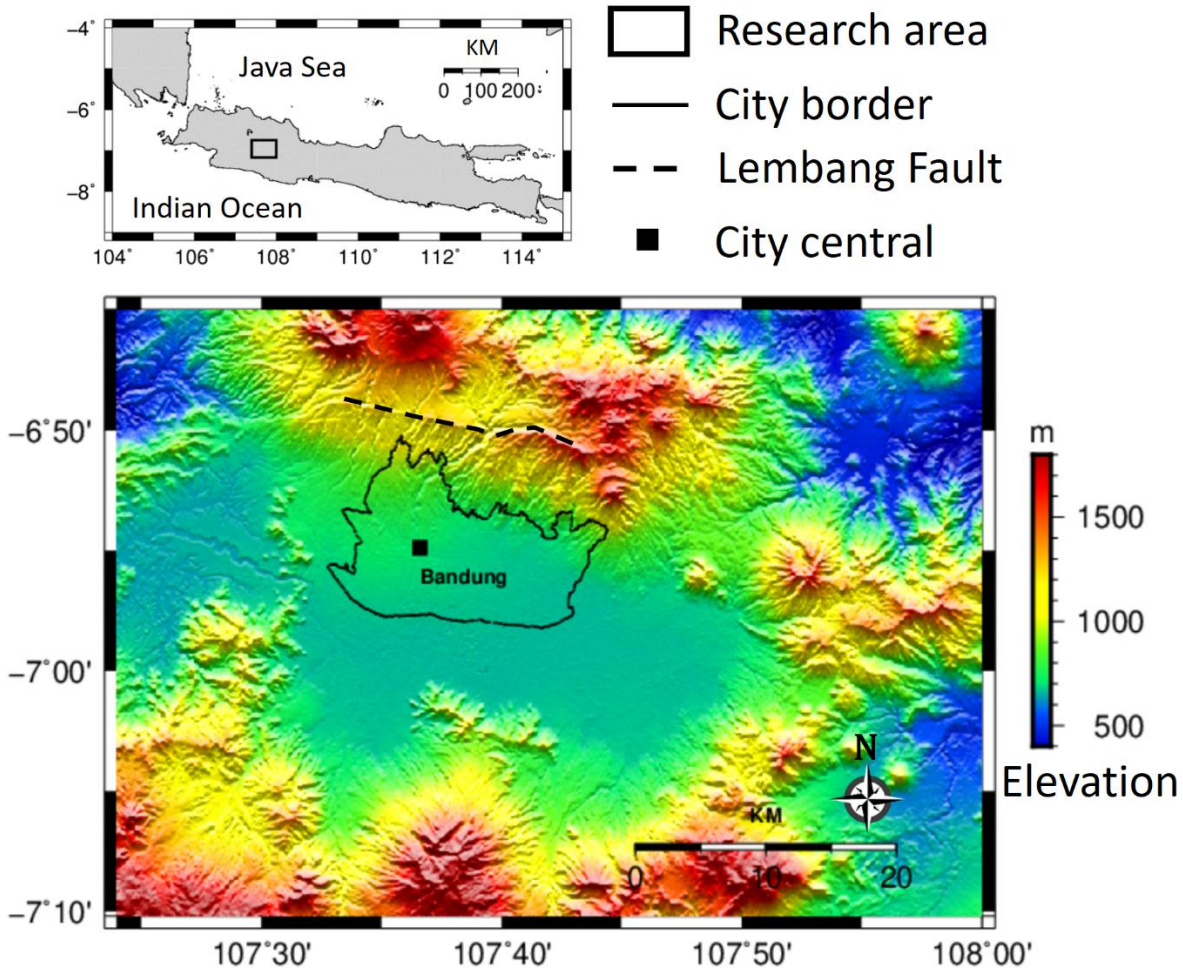

Figure 1.2 Topographical map of the Bandung basin. Thin solid and dashed black lines correspond to the administrative border of Bandung city and location of Lembang fault, respectively. Location of the Bandung basin is shown in a rectangle in the upper map

The surface geological map of the Bandung basin (Dam & Suparan, 1992) is shown in Figure 1.3. The Bandung basin consists of two main features of the rock types of the geological units in the map. The first feature is the lake deposit or lacustrine sediment in the centeral part of the basin that is characterized by a flat area with an elevation of 665 m. The second feature is various volcanic deposits and products that surround the lake deposit, and reaching elevations more than 1000 m. The schematic north-south cross-section of the Bandung basin in Figure 1.4 indicates that the basin is mostly composed of the lake deposits and it is overlied by the volcanic rocks as the bedrock. Lake deposit in the basin is characterized by thick organic silt and clay (Dam et

al., 1996; Desiani & Rahardjo, 2017). Meanwhile, the volcanic products and deposits that surround the lake deposit are composed of tuff, basalt, andesite, dacite, breccia, and lava.

The seismicity in this area is dominated by moderate to strong earthquakes from the subduction zone in the southern part of Java Island, e.g., the 2009 West Java earthquake (Mw7.0) with an epicenter distance of 160 km from the Bandung basin (Afnimar et al., 2015). The event was felt in the Bandung basin with an intensity of 5 (MMI), which corresponds with moderate shaking. Moreover, another potential of an earthquake source in the basin is coming from an existence of a 24 km-long Lembang fault in the northern part as an active fault. The seismicity around the Lembang fault is generally infrequent and very low in magnitude (Afnimar et al. 2015). However, there is evidences of the fault movement with a slip rate of 6 mm/year from geodetic observations (Meilano et al., 2012) that shows a high potential of the seismic risk caused by the fault. From the empirical relationship of an earthquake magnitude with a surface rupture length (e.g., Wells & Coppersmith, 1994), it could be assumed that the Lembang fault is capable of producing an M6.5 – 7.0 class event in a worst-case scenario (Daryono et al., 2019).

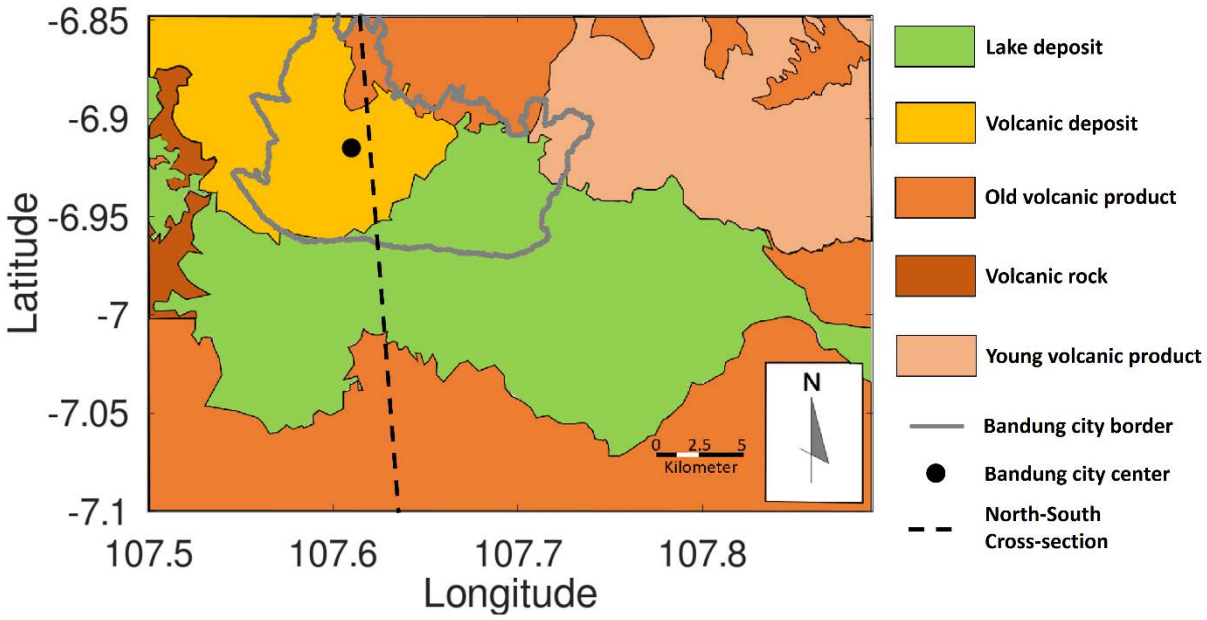

Figure 1.3 Simplified surface geological map of the Bandung basin from modification of Dam and Suparan (1992)

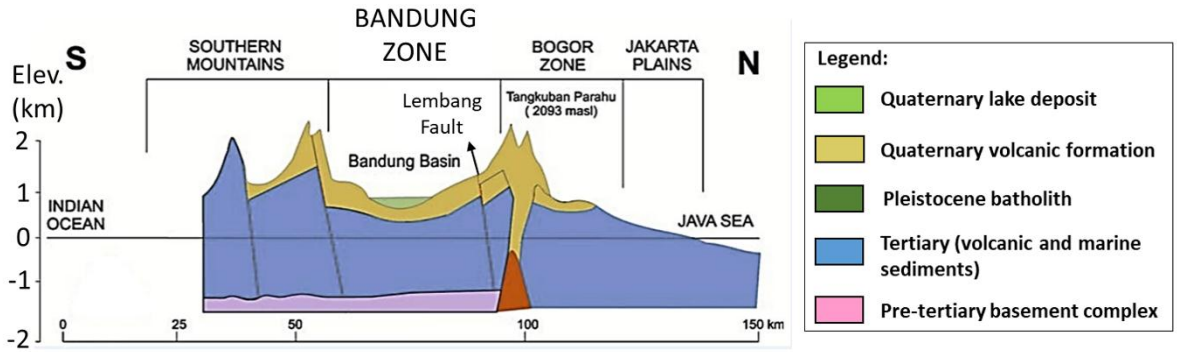

Figure 1.4 Schematic North-South cross section of the Bandung basin region, modified from Delinom (2009). The Bandung basin is situated on Quaternay volcanic formation.

1.3 Reviews of previous studies

1.3.1 S-wave velocity profiles in Bandung basin

Several investigations have been conducted regarding S-wave velocity profile information in the Bandung basin. First, Handayani et al. (2009) simulated a horizontal peak ground acceleration (PGA) in the basin from an earthquake in the Lembang fault

using an empirical attenuation relationship proposed by Boore et al. (1997). Figure 1.5a shows their PGA map. A high PGA region is represented by red color and it concentrates in the epicentral region and also in the eastern part of the basin. However, a calculation of the empirical relationship requires the averaged S-wave velocities in 30 m depth (Vs30) which are not available in the basin. Therefore, they referred an established Vs30 relation with geological units in California (Wills et al., 2000) to classify ranges of the Vs30 based on the surface geological units in the Bandung basin as shown in Figure 1.5b. A low Vs30 range can be seen for the lake deposit area that is represented by yellow color with a velocity range of 180 to 360 m/s. On the other hand, the volcanic region represented by pink colors has a velocity range from 500 to 1000 m/s. Unfortunately, their study does not mention in details about the distribution of Vs30s in the basin for the calculation of the PGA map. This indicates limited Vs profile information in the basin.

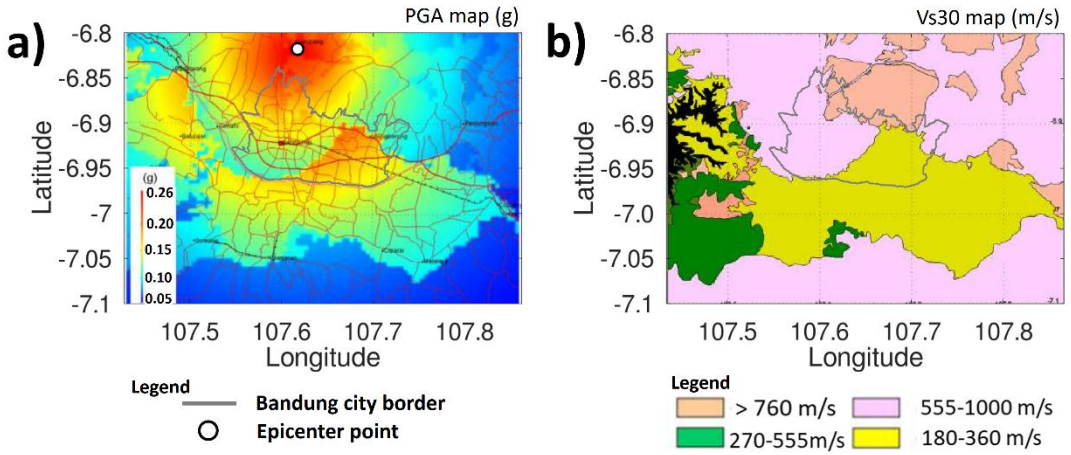

Figure 1.5 a) Peak ground acceleration map and b) averaged S-wave velocity at the top 30 m (Vs30) in the previous study by Handayani et al. (2009).

A recent study of the S-wave velocity profile information in the Bandung basin has been provided by Pranata et al. (2019) in a collaboration with the Australian

National University who provide the broadband seismometers to apply the ambient noise tomography technique. They obtained an S-wave velocity structure of the upper crust beneath the Bandung basin to depths of 10 km from an inversion of the observed Rayleigh wave group velocities in a period range of 1 to 8 seconds. Examples of the group velocities distribution in the basin for periods of 1 and 8 seconds are illustrated in Figure 1.6. They found a relatively low velocity zone in the western part of the Tangkuban Perahu volcano which is associated with fluid or partial melt of the volcanic products that are trapped in the underneath of the volcanic system. Moreover, they found low velocity anomalies below the western part of the lacustrine deposit at 5 to 10 km. However, since the lowest period of the observed Rayleigh wave group velocity is 1 second, the obtained S-wave velocity profiles have a low resolution in the shallow part (< 1 km) of the basin.

The above previous studies suggest the lack of the shallow S-wave velocity profile information in the Bandung basin which is necessary to understand the characteristics of soil amplification in this area.

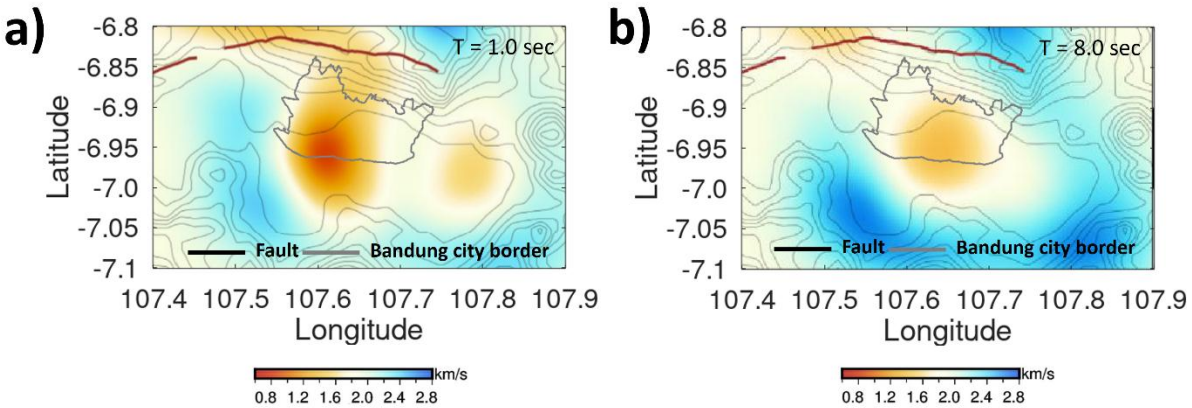

Figure 1.6 Rayleigh wave group velocities in the Bandung basin area using ambient noise tomography by Pranata et al. (2019) at period of a) 1 second, and b) 8 second. The colormap in the background illustrate the group velocity variation. Gray thick, black thick and thin lines correspond to city boundary of the Bandung, the Lembang fault, and countour lines of the same topographic elevation.

1.3.2 Overview of conventional S-wave velocity profile estimations

An S-wave velocity (Vs) profile is generally obtained from a seismic measurement on the field either using invasive or non-invasive methods. The invasive methods require a borehole to insert sensors (sources or receivers) in the soil, e.g. cross-hole, down-hole, and P-S logging. Cross-hole method is capable to measure S-wave velocity directly by inserting source and receiver(s) in the same depth. The velocity is calculated on the basis of travel time between source and receiver(s). Therefore, the method can provide a reliable and accurate profile. However, the method is quite expensive due to requirement of a borehole.

In other hand, non-invasive methods gain popularity because it is conducted only at the surface and can provide Vs profile in the wide area which is cheaper than the invasive method. Among available non-invasive methods, the surface wave and the microtremor measurements are commonly used as the conventional methods to obtain the Vs profiles (Foti et al., 2014; Foti et al., 2011; Lontsi et al., 2016; Park et al., 2005). In principle, these measurements are intended to obtain the Rayleigh wave phase velocity in a wide frequency range that indicates a variation of frequency-dependent surface wave velocity. This observed phase velocity can be inverted to obtain a Vs profile. In an inversion process, a Vs profile is commonly represented by a horizontally-layered model (1D Vs profile). An S-wave velocity and a thickness of each layer are determined to obtain the theoretical phase velocity that fit the observed phase velocity.

In the surface wave measurement, the multichannel analysis of surface wave (MASW) method by Park et al., (1999) is commonly used. The method utilizes a line array of geophones to measure the surface waves that artificially generated using an impact source. The method also require to set a large distance of the line array using

many instruments with typically 24 geophones or more to obtain a wide frequency range of observed phase velocity.

In the microtremor measurement, it utilizes the microtremor that naturally emerged from human or natural activity like traffic, construction activity, ocean waves and atmospheric pressure variation (Okada, 2003; Jafari et al., 2005). Several signal processings are available for analysis of microtremor records to obtain the phase velocity, such as frequency-wavenumber (f-k) (Capon, 1969) and the spatial autocorrelation (SPAC) (Aki, 1957) methods. The measurement is usually conducted by setting an array consist of more than three idential microtremors sensors to apply the methods.

Event though the above methods are conventionally used to provide shallow S-wave velocity profile, we may face a difficulty to implement the methods in the Bandung basin due to limitation of available instruments. Such large number of geophones and expensive broad-band microremors sensors are not commonly available in Indonesia. This situation also cause a lack of the shallow S-wave velocity information in the country. Therefore, another approach of S-wave velocity profile estimation is required to overcome the limitation of available instruments.

1.3.3 Usage of velocity-depth function for S-wave profile

To accommodate the observed data that can be obtained from the reduction of required instruments for Vs profile estimation, we need to simplify the representation of Vs profile from a layered model to a single layer over a half-space model by using the velocity-depth function. A profile representation with the velocity-depth function can reduce the number of the model parameters to become only 2 parameters, namely a

surface S-wave velocity and a velocity gradient. With a smaller number of the model parameters, the inversion can be simplified and making the Vs profile estimation easier.

A usage of Vs profile representation by velocity-depth function is based on the fact that the S-wave velocities of a soil deposit increase gradually with depths due to continuous sedimentation and compaction which is old sediments have a relatively higher velocity than young sediments. Early usages of the velocity-depth function for profile representation (e.g., Slotnick, 1936; Al-Chalabi, 1997; Vrettos, 1996) had been conducted to derive a time-depth relation of subsurface condition in a seismic exploration method using P or S waves (e.g., seismic reflection, and seismic refraction). Moreover, the usage of a velocity-depth function in Vs profile estimation has been considered by several studies (Scherbaum et al., 2003; Wathelet et al., 2004). In Scherbaum et al. (2003), they estimated the surface S-wave velocity and the thickness as the model parameters by applying a grid search method to evaluate the optimal model parameters that having the lowest misfit between the observed data and the theoretical ones. They utilize a wide frequency range of phase velocity or horizontal-to-vertical spectral ratio (H/V) amplitude as the observed data. However, the usage of the observed H/V amplitude in the profile estimation is not straightforward since the amplitude of the H/V is controlled by contribution of Rayleigh and Love waves, which may vary at each site (Dal Moro 2014).

The velocity-depth functions have also been used to establish empirical relations between thicknesses of sediment and observed H/V peak frequencies. Ibs-von Seht and Wohlenberg (1999) conducted a study in the western Lower Rhine Embayment in Germany in an effort to map the sediment thicknesses from observed H/V spectra. The study used a fixed surface velocity and a fixed velocity gradient of the velocity-depth

function from a priori information. This method was also applied by Parolai et al. (2002) and D‟Amico et al (2008) to assess the thickness of the sediment in the areas they investigated. However, this method could not accommodate a local velocity variation of soil conditions from site-to-site as it caused errors in anticipating the soil amplification.

There are various kinds of velocity-depth functions in Vs profile representations have been used to represent sediment profiles from borehole observations. For example, a linear velocity increment is observed in the profiles of Holocene Bay mud sediments in Oakland, California (Holzer et al., 2005), and in soil deposits at Shimousa deep borehole observatory Japan (Yamamizu et al., 1983). In other studies, a power-law of velocity increment is observed in profiles of Tertiary sediments in the Cologne area, Germany (Parolai et al., 2002) and Quaternary-Tertiary sediments in the Almaty basin, Kazakhstan (Parolai et al., 2019). However, Wang et al. (2018) show an advantage of the profiles represented by a linear velocity increment that have a better estimation of the fundamental peak frequencies than profiles represented by a power-law velocity increment based on the evaluation using Kik-net site‟s profiles in Japan.

1.4 Objectives of the research

Due to the lack of the shallow Vs profiles information in the previous studies, the main objective of this study is to provide shallow S-wave velocity profiles in the Bandung basin for a seismic hazard assessment. However, the conventional methods are difficult to be applied in the area due to the limitation of available instruments. Therefore, we propose a method of Vs profile estimation in this study that can overcome the limitation of available instruments based on utilization of a linear function in the Vs profile representation. We also conduct numerical tests to examine

the features of the proposed method. Furthermore, we analyze the site amplification features from the estimated shallow Vs profiles as an effort to assess the potential seismic hazard in the Bandung basin.

1.5 Thesis organization

This thesis presents shallow Vs profiles estimation in the Bandung basin using a simplified method to accommodate the limitation of the available instruments. The applicability of the proposed method is examined in the numerical tests. Moreover, we evaluate the profile representation with a linear function in the basin using phase velocities obtained by the conventional method before the implementation of the proposed method to provide Vs profiles in the basin. The flowchart of the study is illustrated in Figure 1.7.

Chapter 1 presents the background about the importance to obtain shallow S-wave velocity profiles in the Bandung basin. The geological condition and seismicity in the Bandung basin are described. Previous studies related to the S-wave velocity profiles in the basin, the conventional Vs profile estimation methods, and the usage of velocity-depth function for a profile representation is discussed respectively. Finally, the objectives in this study are given in this chapter

Chapter 2 describes the methodology that we used in this study to estimate a Vs profile. This chapter explains a usage of linear S-wave velocity function to simplify profile parameters as the basis of the proposed method. We then describe the profile parameters estimation of the proposed methods.

Chapter 3 demonstrates the numerical tests to investigate the applicability of the proposed method by using synthetic data generated from borehole profiles in the

Bandung basin. The comparison of the borehole profiles with the estimated Vs profiles from the conventional method using phase velocity data and the proposed method is also explained. In the end, characteristics of the proposed method are investigated with the applicable limitation of the proposed method.

Chapter 4 illustrates a distribution of the observed Rayleigh wave phase velocities in the Bandung basin from the conventional microtremor array measurements. The comparison between the observed and the theoretical phase velocities of a profile assuming a linear velocity increase is discussed to evaluate an appropriateness of the profile representation with a linear function of velocity in the area. The Vs profiles estimated using the observed phase velocities are also explained.

Chapter 5 shows the implementation of the proposed method in the actual field measurement in the Bandung basin. The variation of the observed surface S-wave velocities, H/Vs, and the estimated Vs profiles in the basin are described. Furthermore, we discuss results of the comparison between the Vs profiles estimated from the conventional and the proposed methods. We also investigate the smallest number required in the estimation of the surface S-wave velocity. A guidance to apply the proposed method in other area is also explained in the end of the chapter.

Chapter 6 describes site characterization of site amplification features in the Bandung basin from the estimated Vs profiles in Chapters 4 and 5. Comparison of the estimated site amplifications from the obtained Vs profiles using the conventional method and the one estimated from the proposed method is discussed. Based on the similarity in several site amplification proxies, characteristic of the site amplification in the basin is explained. We also calculate the horizontal peak ground acceleration (PGA) in the basin considering Vs30s of our results by using an empirical attenuation

relationship as conducted in the previous study (Handayani et al., 2009). We then describe the comparison of PGA values between the previous study and our results.

Chapter 7 presents conclusions and possible future tasks of the study.

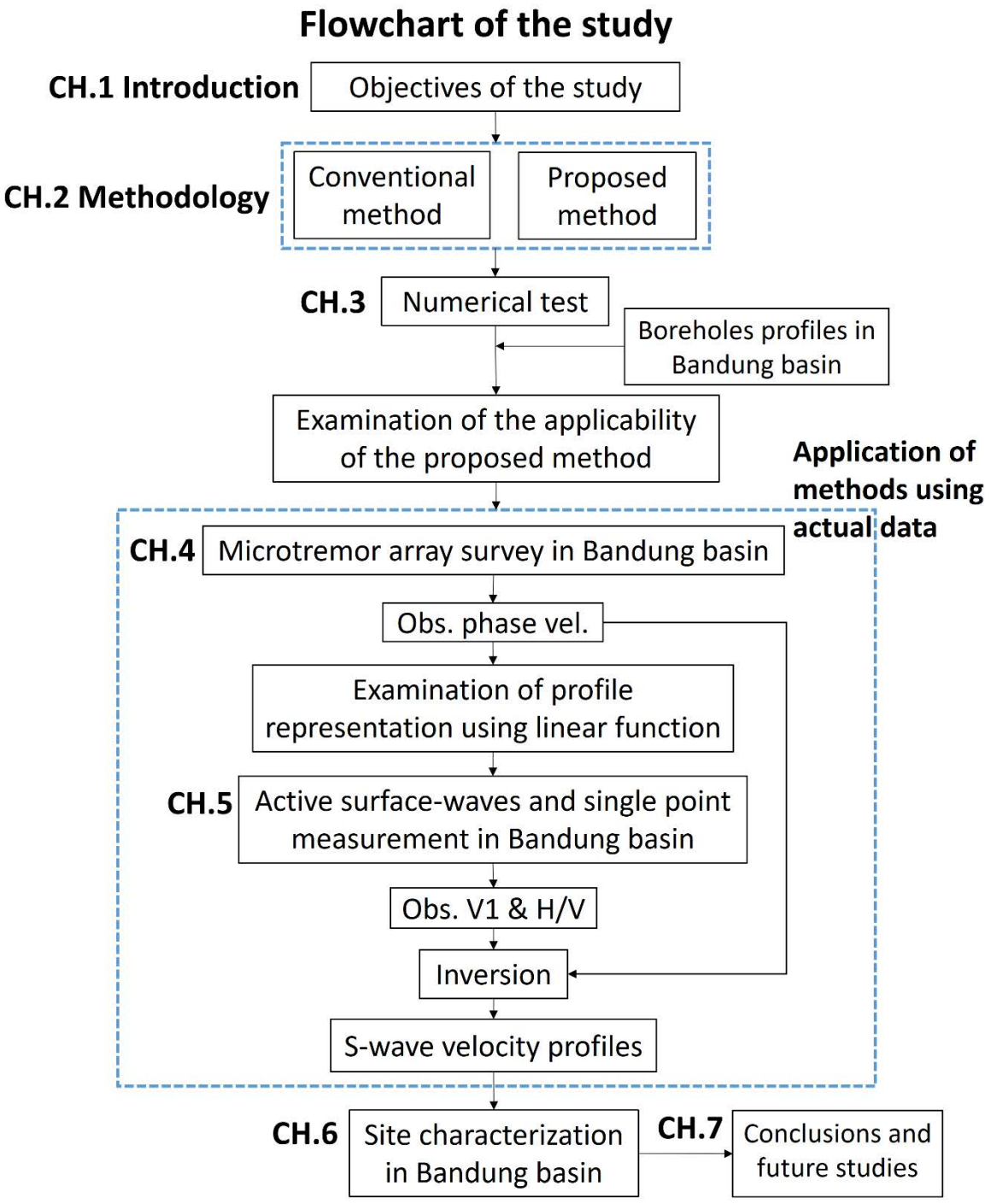

Figure 1.7 Flowchart of this study

Chapter 2 Methodology

2.1 Overview of the proposed method

2.2 Profile representation using a linear S-wave velocity function

2.3 Examination of linear S-wave velocity representation

2.4 Model parameters estimation

2.1 Overview of the proposed method

The new proposed method of Vs profile estimation utilized a linear Vs profile representation because a better resonant frequency can be provided than a power-law profile representation. Furthermore, the number of the profile parameters becomes only two with this Vs profile representation. Consequently, the proposed method could provide a simple Vs profile estimation. Figure 2.1 illustrates the overview of the proposed method. The procedure of the proposed method consists of three main steps. At first, we assume a profile with the linear function of S-wave velocity. Next, the appropriateness of the linear profile representation can be examined using available P-S logging or observed phase velocities in an investigated area. If the observed data can be well approximated by the linear profile representation, we can conduct Vs profiling at sites in whole an area by estimating the two profile parameters from field surveys. The detailed description of the three steps is provided in the following subchapters.

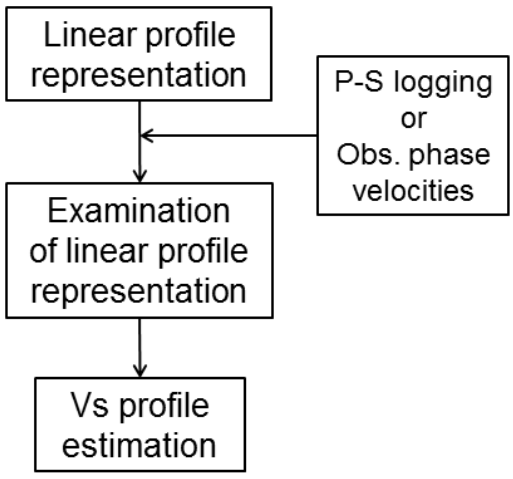

Figure 2.1 Flowchart of the proposed method for estimating a Vs profile

2.2 Profile representation using a linear S-wave velocity function

We represent an estimated Vs profile in the proposed method using the linear function of S-wave velocity in depth as expressed in Equation 2.1 (Slotnick, 1936; Wang & Wang, 2016).

$$Vs(z) = \begin{cases} V1 + bz, & \text{for } 0 \le z < z_B \\ V_B, & \text{for } z \ge z_B \end{cases} \quad \dots (2.1)$$

$$z_B = \frac{V_B - V1}{b}$$

where Vs(z) is an S-wave velocity at depth *z*. V1, *b*, and V_B are surface S-wave velocity, velocity gradient, and bedrock S-wave velocity. Z_B is a bedrock depth which is derived from the linear function. In actual representation, we discretized the linear profile into numerous thin layers, each with a thickness of 0.1 m.

Based on equation 2.1, the profile parameters are a surface S-wave velocity (V1), a velocity gradient (*b*), and a bedrock S-wave velocity (V_B). In this study, the bedrock S-wave velocity is given considering *a priori* information from geological or geophysical surveys. Therefore, a Vs profile can be provided by only estimating the V1 and the velocity gradient. Similar model parameters have also been used in the previous studies of the Vs profiles estimation (e.g. Scherbaum et al. 2003; Wathelet et al. 2004) even though their estimated profiles are represented using a power-law function.

2.3 Examination of linear S-wave velocity representation

Since a type of the velocity-depth functions to represent an estimated profile will be depend on a region (i.e. sedimentation process, ages, and soil types), the appropriateness of the linear profile representation in an investigated area must be confirmed before applying the proposed method. We examine the linear profile representation using

available borehole profiles or a wide frequency range of observed phase velocities in an investigated area. The evaluation is conducted by finding the lowest misfit profile parameters (i.e. a pair of V1 and gradient) to the available borehole profiles or observed phase velocities through a grid-search procedure. The misfit (ε) is calculated using equation 2.2 if we only have observed phase velocities.

$$\varepsilon = \sqrt{\left(\sum_{i=1}^{n}(c_{obs}(f_i) - c_{theo}(f_i))^2\right)/n} \qquad (2.2)$$

where ε is the misfit. C_{obs} (f_i), and C_{theo} (f_i) are the observed and the theoretical phase velocities at the i-th frequency and n is the number of the observed phase velocity. If we have a borehole profile, the phase velocities in Equation 2.2 can be replaced by S-wave velocity of the borehole profile for each depth. The profile representation using a linear function is appropriate if the lowest misfit pair of the V1 and the gradient could explain most of the features of the borehole profiles or observed phase velocities.

2.4 Model parameters estimation

After we confirmed the appropriateness of the linear profile representation through the examination, we can further provide the Vs profiles by only estimating the V1 and the gradient. The V1 and the gradient can be estimated conventionally by using a wide frequency range of observed phase velocities (e.g. Scherbaum et al. 2003; Wathelet et al. 2004). However, a wide frequency range of the phase velocity is not easy to be obtained when available instruments are limited in number. Hence, we utilize an observed phase velocity at a high-frequency for the V1, and the gradient is estimated from an observed microtremor H/V in the new proposed method to overcome the limitation of available

instruments. The procedure of the model parameters estimation in the proposed method is illustrated in Figure 2.2.

We assume that the V1 is the same as observed fundamental mode Rayleigh wave phase velocities at the high-frequency end of its dispersion curve. Therefore, the V1 can be measured using an active seismic measurement. A few geophones are set along a short surveying line to observe the phase velocity of the Rayleigh wave at high frequency from an impact source. The measurement becomes simpler by utilizing fewer geophones than used in conventional seismic or surface-wave methods in which phase velocity was observed in a wide frequency range. Since we intend to observe a phase velocity in a high-frequency range in the measurements, the observed phase velocity is insufficient to apply the conventional phase velocity inversions. We also take into consideration that the observed Rayleigh wave phase velocity at high-frequency range could be contaminated by a higher wave mode, which may cause the observed values to become larger than those of the fundamental mode (Tokimatsu et al., 1992; Foti el al. 2018). Therefore, we used alternatively the minimum value of an observed phase velocity as the V1 for the fundamental mode of a Rayleigh wave.

Next, the velocity gradient is determined from an H/V observed from a 3-component microtremor record. The procedures to calculate the H/V are started with choosing several time segments of most stationary part from the observed 3-component microtremors that are uncontaminated with transient noises. Then, the Fourier amplitude spectra for each time segment are computed at all the components. The H/V for each time segment is calculated using equation 2.5, which took a quadratic mean of the two horizontal spectra (Arai & Tokimatsu, 2000).

$$\mathrm{H/V(f)} = \frac{\sqrt{NS(f)^2 + EW(f)^2}}{UD(f)} \quad \ldots(2.5)$$

where NS(f), EW(f), and UD(f) are Fourier amplitude spectra of microtremor records in the north-south, east-west, and up-down components. The final H/V was obtained from averaging of the entire H/Vs for all the time segments.

We determine the velocity gradient using a peak frequency of the observed microtremor HVSR. We used the peak frequency of the observed H/V in this study instead of its amplitude as was conducted in Scherbaum et al. (2003) to consider only the fundamental mode of Rayleigh wave ellipticity (Yamanaka et al., 1994; Konno and Ohmachi 1998; Fäh et al., 2001) and for a more robust estimation of the gradient. A grid search procedure was applied to determine the gradient based on an agreement in the peak frequencies between the observed H/V and the theoretical ellipticity for the linear-velocity model with the measured V1 and the given bedrock velocity, considering the fundamental mode of the Rayleigh wave.

The new proposed method offers a simpler procedure than the conventional microtremor array measurements for a shallow Vs profile estimation. The instrument for the V1-H/V measurement only requires inexpensive geophones with a natural frequency of 4.5 Hz and a three-component microtremor sensor. On the other hand, the conventional microtremor array survey requires several expensive broad-band instruments. Furthermore, the array survey needs several measurements with different sizes of arrays to obtain observed phase velocities in a wide frequency range. Therefore, the new proposed method can provide a Vs profile with less measurement and data processing effort than the conventional methods.

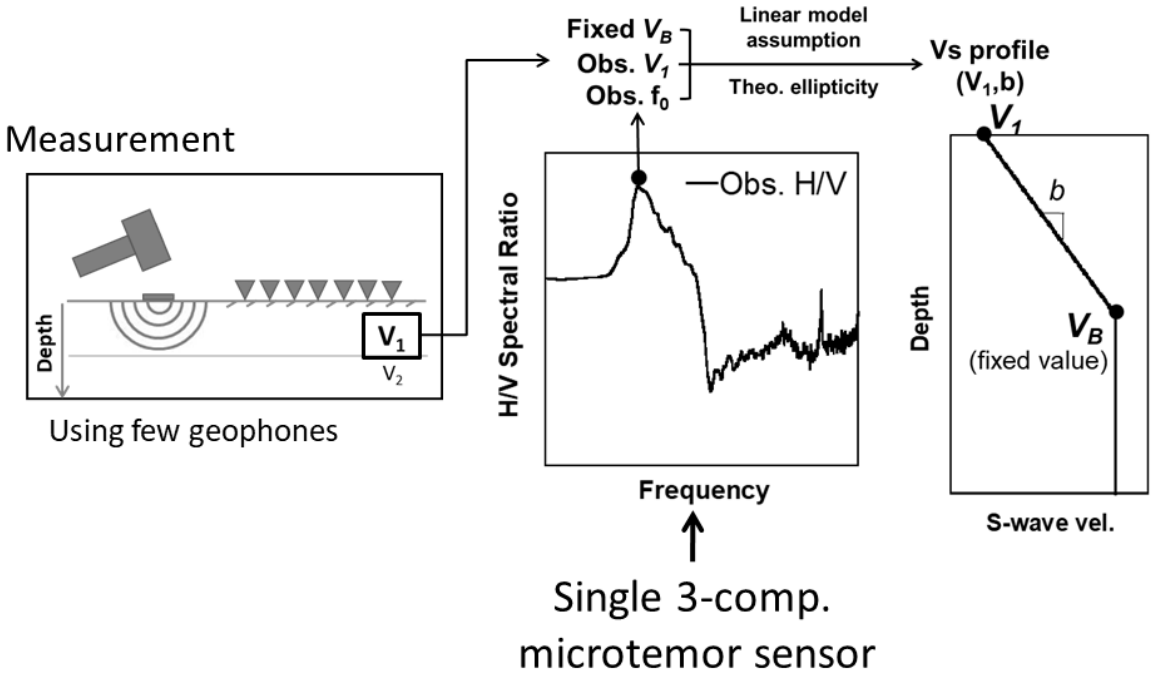

Figure 2.2 Illustration of the proposed method using a surface S-wave velocity (V1) and a peak frequency of microtremor H/V (f0). V1 is estimated from the the high-frequency end or the minimum values of the observed fundamental mode Rayleigh wave phase velocity using a short length active seismic measurement. The velocity-depth gradient (*b*) is determined from the agreement of the peak frequencies between the theoretical ellipticity of fundamental mode Rayleigh wave and the observed H/V. We assumed a profile is represented by a linear model with an assumed bedrock velocity (V_B).

Chapter 3 Numerical tests

3.1 Objective

3.2 Borehole profiles in Bandung basin

3.3 Synthetic data

3.4 Estimated profiles

3.4.1 Profile estimation with conventional method

3.4.2 Profile estimation with proposed method

3.4.3 Comparison of the estimated Vs profiles with the borehole profiles

3.5 Discussion

3.5.1 Difference in estimated bedrock depth

3.5.2 Effects of different bedrock velocities

3.5.3 Effects of other velocity functions

3.5.4 Effects of random noises in observed data

3.6 Investigation of difficult cases in assumption of linear velocity function

3.1 Objective

In this chapter, we aim to examine the applicability of the proposed method through numerical tests. Since we want to apply the method for profile estimation in the Bandung basin, we collected the borehole profiles in the basin to generate synthetic phase velocities and synthetic H/Vs. Then, the proposed method is applied to synthetic data. The appropriateness of the estimated Vs profiles from the proposed method is evaluated by comparing with the borehole profiles and the Vs profiles obtained using the conventional method. We further analyze the effects of the other velocity functions, different bedrock velocities, and contamination of random noises in the observed data to the estimation of a Vs profile. In the end, we discuss the limitation of the proposed method.

3.2 Borehole profiles in Bandung basin

We utilized three borehole profiles those only contain soil-type data from geomorphological and sedimentological studies (Dam & Suparan, 1992; Dam et al., 1996) because P-S logging data are not available in the Bandung basin. The locations and the descriptions of the boreholes are shown in Figures 3.1 and 3.2. All the boreholes are situated on the lake deposits. One borehole is located in the western part, and two are located in the central part of the basin.

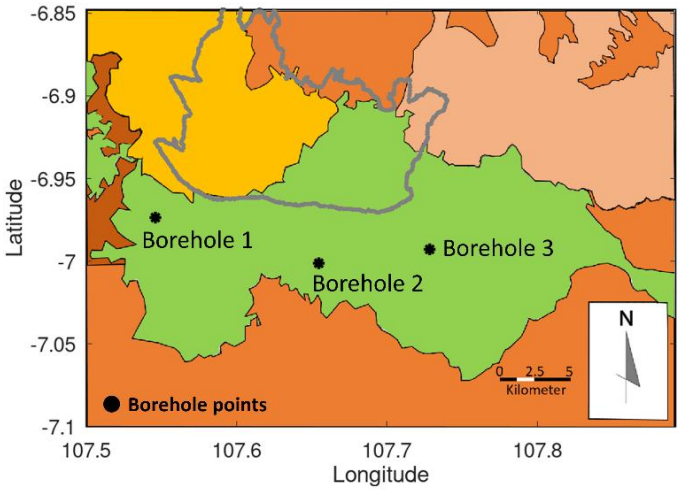

Figure 3.1 Locations of the boreholes in the Bandung basin on the surface geological map. The legend of the geological map can be seen in Figure 1.3.

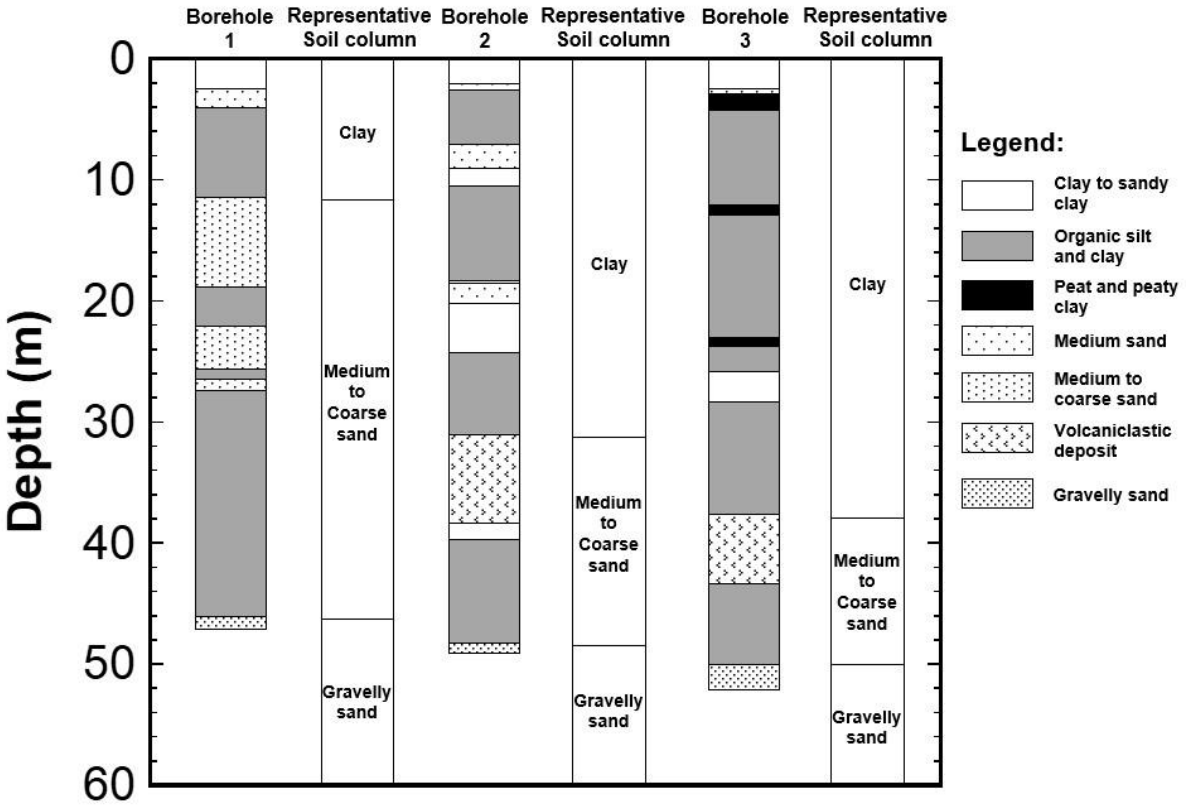

Figure 3.2 Soil columns of boreholes in the Bandung basin. Borehole 1 is taken from Dam and Suparan (1992), while boreholes 2 and 3 are taken from Dam et al. (1996).

In Figure 3.2, we observed that the soil layers are dominated by thick Quaternary lacustrine deposit that was characterized by organic silt and clay, from the surface to depths of 46 m, 48 m, and 50 m in the boreholes 1, 2, and 3 (Dam and Suparan, 1992; Dam et al., 1996). Intercalation of the volcaniclastic sediments produced by eruptions of the northern volcano were also observed in depths of 12 to 28 m, 31 to 38 m, and 38 to 43 m at borehole 1, 2, and 3, respectively.

We then converted the soil column profiles to S-wave velocity profiles by employing an empirical equation proposed by Ohta & Goto, (1978). S-wave velocity is derived from N-value, depth, soil type, and geological age with the equation established from 300 boreholes located mostly on the sedimentary rock in Japan. We utilized Equation VII in their study, which only involves the parameters of depths and soil type information to derive S-wave velocity profiles. The equation is:

$$Vs(z) = 78.98\, z^{0.312}\, SF \quad \ldots(3.1),$$

where SF is a soil type factor. The values of the factor are listed in Table 3.1. Since the empirical equation gives a null velocity at a depth of 0 m, we set the depth value (z) of the empirical equation equal to 1 to calculate an S-wave velocity at depths from 0 to 1 m. We also use the soil factor of 1.0 at these depths, considering that all of the soil columns are composed of clay. Therefore, the S-wave velocity at these depths is 79 m/s.

Table 3.1 Soil type factors of the empirical equation in Eq. 3.1 (Ohta and Goto, 1978).

Soil type	SF
Clay	1.000
Fine Sand	1.260
Medium Sand	1.282
Coarse Sand	1.422
Sand and Gravel	1.641
Gravel	2.255

Before we convert the soil column to the S-wave velocity using the empirical equation, we simplify the representation of the soil column considering its soil classification, as shown in Figure 3.2. We considered that the borehole profiles consist of two main layer-boundaries. The first layer boundary is set between the lacustrine sediments and the volcaniclastic sediments at depths of 12 m, 31 m, and 38 m in boreholes 1, 2, and 3, respectively. The S-wave velocities of the lacustrine sediment are from 79 m/s to 171 m/s, 230 m/s, and 246 m/s in boreholes 1, 2, and 3. Regarding the volcaniclastic sediment layers, we set the soil type factor in the empirical equation with 1.352 as the average value between „medium sand" and „coarse sand". The second layer boundary is set at the top of the gravelly sand at depths of 46 m, 48 m, and 50 m in boreholes 1, 2, and 3. At these depths, we assumed the gravelly sand layers as the bedrock layers with S-wave velocities of 508 m/s, 515 m/s, and 521 m/s in boreholes 1, 2, and 3, respectively. The bedrock velocities were obtained from the empirical equation using the depth of the gravelly sand layers in each borehole and a soil type factor of 1.948 as the average value of the factor between 'sand and gravel' and 'gravel'. The corresponding S-wave velocity profiles are summarized in Table 3.2.

Table 3.2 S-wave velocity profiles of the soil column in the Bandung basin used for the numerical test

Layer	**S-wave velocity (m/s)**			**The thickness of layer (m)**			**Density (g/cm^3)**	**Soil type**
	Br. 1	**Br. 2**	**Br. 3**	**Br. 1**	**Br. 2**	**Br. 3**		
First	$78.98\ z^{0.312}$			12	30.8	38	1.5	Clay
Second	$106.78\ z^{0.312}$			34	17.2	12	1.7	Medium to coarse sand
Bedrock	508	515	521	-	-	-	1.8	Gravelly sand

*** Br. = Borehole, z = depth**

3.3 Synthetic data

The S-wave velocity profiles are further used to generate the synthetic phase velocities and ellipticities of the fundamental mode of Rayleigh waves in Figures 3.3 and 3.4 to apply the conventional and the proposed methods. The calculations of the phase velocities and the ellipticities are based on Haskell (1953). P-wave velocities (Vp) were derived from S-wave velocities (Vs) using an empirical relationship from Kitsunezaki et al. (1990), as shown:

$$Vp = 1.11Vs + 1290 \ldots (3.2)$$

with the unit of Vp and Vs in m/s. The surface S-wave velocity (V1) required for the proposed method is decided from the convergent value of the fundamental mode Rayleigh wave phase velocity at a high-frequency end. We set the frequency range of the synthetic phase velocity from 0.5 Hz to 40 Hz considering typical frequency range of observed phase velocities from microtremor array measurements in previous studies (e.g. Satoh et al. 2001; Karagoz et al. 2015). We observed in Figure 3.3 that the phase velocity at a frequency of 40 Hz is convergent to a velocity of 78 m/s which is close to the V1 of the borehole profiles.

In this study, we assumed the synthetic observed phase velocity by contaminating the theoretical phase velocities of the borehole profiles with ±10% random noises. The synthetic observed V1s for boreholes 1, 2, and 3 were taken from the synthetic observed phase velocities at a frequency of 40 Hz with velocities of 80 m/s, 83 m/s, and 72 m/s, respectively. Moreover, the synthetic ellipticity peak frequencies for the boreholes 1, 2, and 3 are 2.6 Hz, 1.5 Hz, and 1.4 Hz, respectively. We then contaminated the ellipticity peak frequencies of the borehole profiles with random noises of ±10% as the observed H/V peak frequencies. The synthetic observed H/V peak frequencies of the boreholes 1,

2, and 3 are 2.9 Hz, 1.7 Hz, and 1.5 Hz, respectively. The usage of ±10% random noises in the phase velocity and the ellipticity peak frequency is to illustrate an existence of observational errors. The synthetic observed phase velocities in a wide frequency range were used for the conventional method. Furthermore, the synthetic observed V1s and the H/V peak frequencies were used for the proposed method.

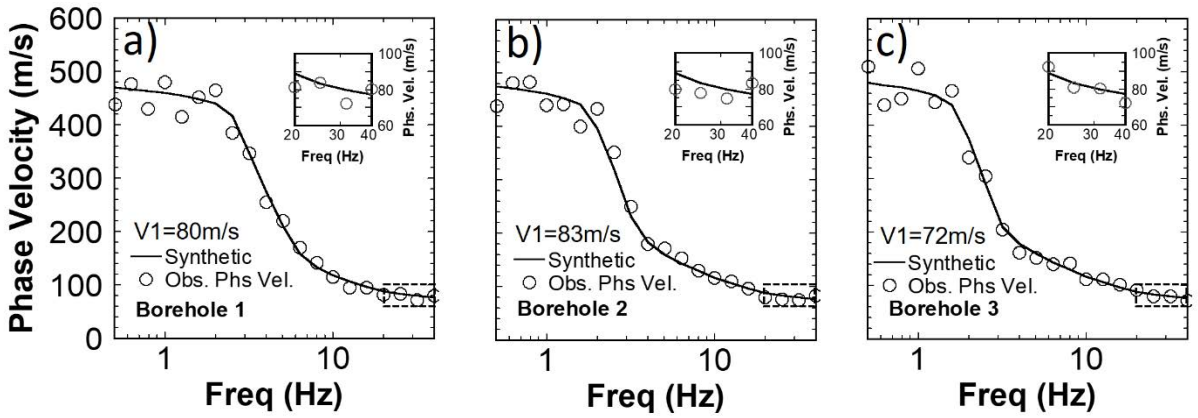

Figure 3.3 Theoretical phase velocity at a) Borehole 1, b) Borehole 2, and c) Borehole 3. Solid black lines and circles correspond with the synthetic fundamental mode of Rayleigh wave phase velocity from the borehole profiles in Table 3.2 and the synthetic observed phase velocity from the contamination of ±10% random noises to the synthetic phase velocity, respectively. The inset figure shows a high-frequency range of the phase velocity. The observed V1 is decided from the observed convergent phase velocity at a frequency of 40 Hz.

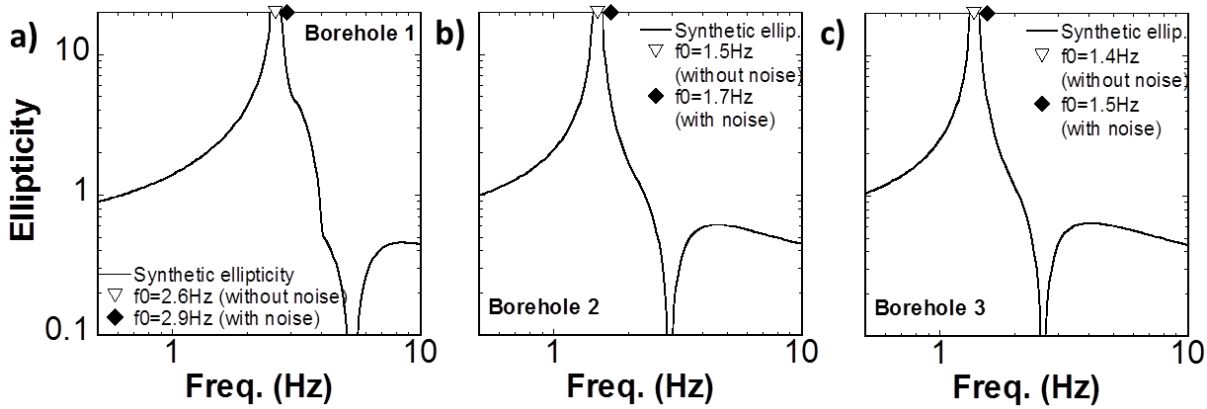

Figure 3.4 Ellipticity peak frequencies in a) Borehole 1, b) Borehole 2, and c) Borehole 3. Solid black line and reversed triangle mark indicate the synthetic fundamental mode of Rayleigh wave ellipticity from the borehole profiles in Table 3.2 and their ellipticity peak frequency, respectively. Diamond mark corresponds to the observed H/V peak frequency after contamination of ±10% random noise to the peak frequency of the synthetic ellipticity.

3.4 Estimated profiles

3.4.1 Profile estimation with conventional method

In the conventional method, the V1 and the gradient were estimated using a wide frequency range of phase velocity through a grid search procedure. The search limits and the parameter increments for V1 and the gradient were defined as listed in Table 3.3. The fundamental mode of Rayleigh wave phase velocity was calculated for each V1 and gradient pair assuming the bedrock velocity of 500 m/s to evaluate its misfit. Figure 3.5 illustrates the contour map of the misfits for all V1 and gradient pairs. The V1 and the gradient of the lowest misfit (star mark) were chosen for the optimal Vs profile. The obtained V1 and gradient at boreholes 1, 2, and 3 are listed in Table 3.4. We observed that the theoretical phase velocities of the optimal Vs profiles at all borehole cases could fit well the synthetic observed phase velocities suggesting the appropriateness of the estimated profile represented with the linear function.

Table 3.3 Search limit of model parameters in the grid search to obtain the Vs profile based on the phase velocity data

Parameter	Search limit	Parameter increment
V1 (m/s)	60-250	$\Delta V1 = 1$
B	1-40	$\Delta b = 1$

Table 3.4 Estimated V1 and b using the conventional method in numerical tests

Profile	Estimated V1 (m/s)	Estimated *b*
Borehole 1	74	10.0
Borehole 2	85	7.0
Borehole 3	85	6.0

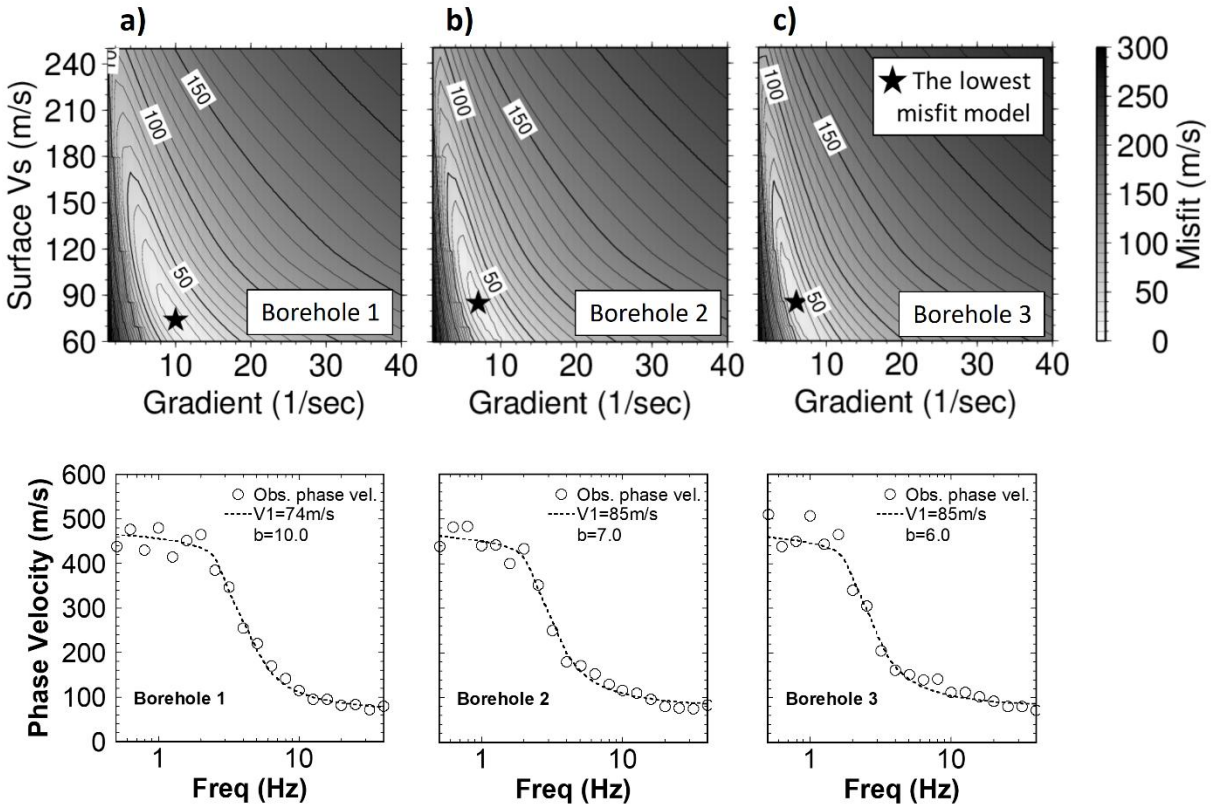

Figure 3.5 Estimation of the surface S-wave velocity (V1) and the velocity gradient (b) in the conventional method using phase velocity data through a grid search procedure at a) Borehole 1, b) Borehole 2, and c) Borehole 3. The upper figures show the misfit contour for all V1-b pairs for the search limit in Table 3.3. The star mark indicates the V1-b pair that gives the lowest misfit to the observed phase velocity, as shown in the phase velocity comparison in the bottom figure. The circle and the dashed line are the observed phase velocity and the theoretical phase velocity of the lowest misfit model parameter (V1 and b), respectively.

3.4.2 Profile estimation with proposed method

The profile estimation using the proposed method was conducted by estimating the gradient because the V1 has been assumed from the observed phase velocity at frequency of 40 Hz, and an S-wave velocity of 500 m/s for the bedrock velocity is given. The gradient is obtained from a comparison of the peak frequencies between the theoretical ellipticity and the observed H/V. Since the gradient controls the thickness of a profile, a smaller gradient corresponds to a thicker thickness of the profile (see Z_B in eq. 2.1). Therefore, the ellipticity for a profile with a small gradient shows the peak at a

low frequency. This suggests that the relation between the gradient and the peak frequency of the ellipticity is proportional.

We illustrate the results of the gradient estimation for all the boreholes in Figure 3.6. We first calculated the theoretical fundamental mode Rayleigh wave ellipticity using an initial gradient. If the initial gradient gives a higher peak frequency of the theoretical ellipticity than the observed one, we gradually decrease the gradient until the peak frequency of the theoretical ellipticity agrees with the observed one. The estimated gradients are 12.6, 7.4, and 7.3 for the boreholes 1, 2, and 3, respectively.

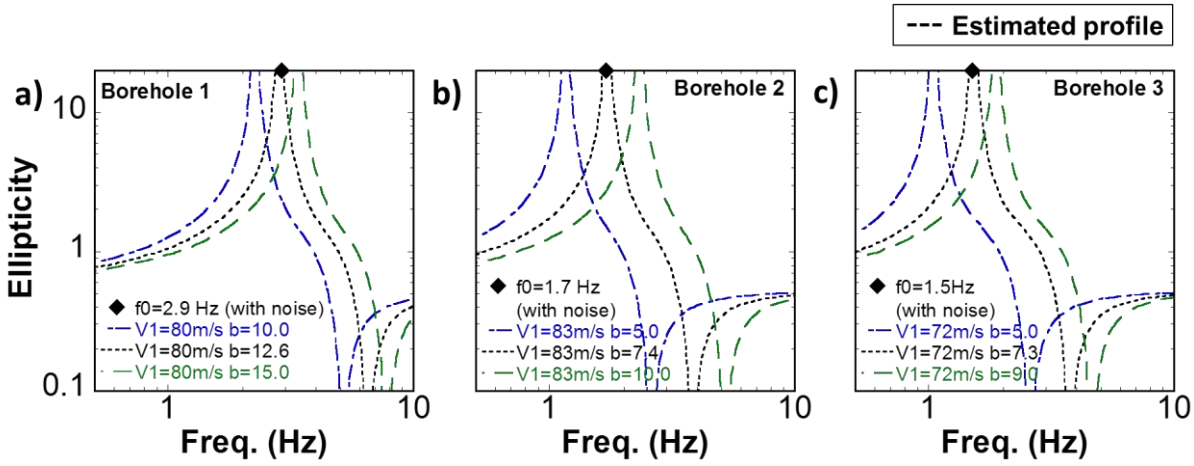

Figure 3.6 Estimation of the velocity gradient (*b*) at a) Borehole 1, b) Borehole 2, and c) Borehole 3 from an agreement of the peak frequency of the theoretical ellipticity of the estimated profile to the peak frequency of ellipticity of the borehole profile. Diamond marks indicated the contaminated peak frequencies of the theoretical ellipticities of the borehole profiles. Blue, green, and black dashed lines correspond to the theoretical ellipticities with small *b*, large *b*, and appropriate *b*.

3.4.3 Comparison of the estimated Vs profiles with the borehole profiles

A comparison of the estimated and borehole Vs profiles is shown in Figure 3.7. The Vs profiles in the figure contain the obtained one using the conventional method, the estimated one by the proposed method, and the borehole profile. Figure 3.7 also shows that the gradients and V1s of the profiles from the conventional and the proposed method are similar.

We observed that the both estimated Vs profiles from the conventional and the proposed methods at borehole 1 show a good approximation to the velocity variation of the first layer of the borehole Vs profile. However, the velocities of the both estimated Vs profiles at depths 20 to 46 m are higher than those of the borehole Vs profile. Meanwhile, the velocity variation of the both estimated Vs profiles at boreholes 2 and 3 well approximate the velocity variation of the first and the second layers of the borehole Vs profiles. However, the both estimated Vs profiles could not accurately estimate the bedrock depths of all the borehole Vs profiles. The estimated Vs profile at borehole 1 has a shallower bedrock depth; meanwhile, the estimated Vs profiles at boreholes 2 and 3 have deeper bedrock depths than the borehole Vs profiles.

Furthermore, we evaluate the quantitative comparison of the profiles by calculating the average relative difference (R) in Equation 3.3 as was used in Xia et al. (2000).

$$R = \frac{100}{n}\sum_{k=1}^{n}\left(\frac{\left|V_{br_k} - V_{c_k}\right|}{V_{br_k}}\right) \quad \ldots (3.3)$$

where V_{br_k} and V_{c_k} are S-wave velocities of the borehole profile and the estimated Vs profile at the *k*-th depth. *N* is the number of samplings of S-wave velocity at every 1 m. Here, the depth range involved in the R-value calculation is started from the surface ($z=0$) to the top of the bedrock layer ($z=z_B$) since we assumed the bedrock layer of the borehole Vs profiles as a half-space layer with a constant velocity.

Agreement of the estimated profile to the borehole profile can be categorized into three groups depending on the R value as described by Xia et al. (2000). The R value at around 10% or less indicates an excellent agreement. The second category of the R value in between 10% to 20% is defined as a good agreement. A fair agreement is

determined if the R value is greater than 20%. The R values of the estimated Vs profiles using the conventional method are 17%, 10%, and 10% for boreholes 1, 2, and 3, respectively. On other hand, the R values of the estimated Vs profiles with the proposed method are 31%, 13%, and 16% for boreholes 1, 2, and 3, respectively. The estimated Vs profile at borehole 1 is categorized as fair agreement with an R-value more than 20%. While the estimated Vs profiles at boreholes 2 and 3 are classified as good agreement with R values less than 20%.

We confirm from this comparison that the conventional or the proposed methods with a linear function profile representation could be applied to estimate the 1D S-wave velocity profiles. We also confirm the appropriateness of the profile representation with the linear function in the tests because the theoretical phase velocities of the estimated Vs profiles could well approximate the observed phase velocities as shown in Figure 3.5. Moreover, we show that the estimated profiles from the proposed method are similar to the obtained ones using the conventional method, indicating that the proposed method could estimate a similar profile with the conventional method.

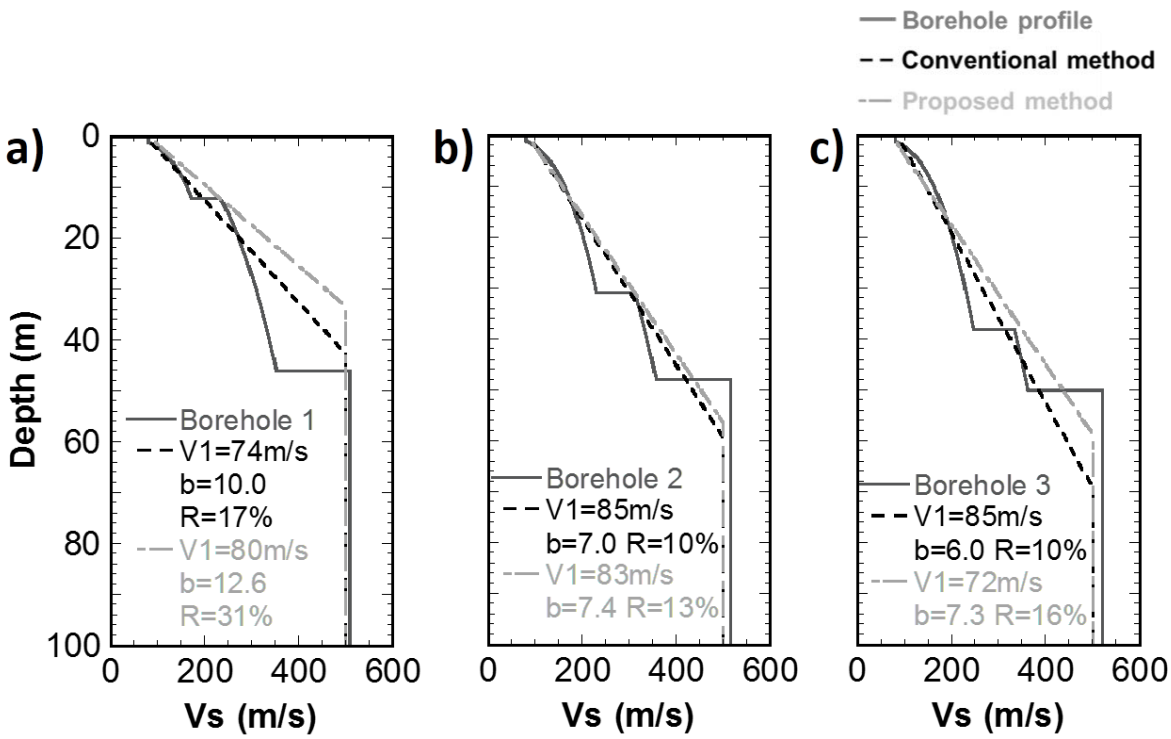

Figure 3.7 Profile comparison between the borehole and the estimated profiles at a) Borehole 1, b) Borehole 2, and c) Borehole 3. Solid gray, dashed black, and dashed gray indicate the borehole profile, the Vs profile obtained using the conventional method, and the Vs profile estimated using the proposed method, respectively. The R-values of each estimated Vs profile is indicated at each plot.

3.5 Discussion

3.5.1 Difference in estimated bedrock depths

We consider the relation of the peak frequency of a theoretical ellipticity (f0) as the ratio of averaged Vs profile from the surface to the top of the bedrock and the total thickness or the bedrock depth (H) of a profile in Equation 3.4 (Konno & Ohmachi, 1998; Ibs-von Seht & Wohlenberg, 1999; Tuan et al., 2011) to investigate the difference of the bedrock depth between the estimated Vs profile from the proposed method and the borehole Vs profile, as shown in Figure 3.7.

$$f0 = Vs/4H \ldots (3.4)$$

Since the profiles in the proposed method are estimated from the agreement of the peak frequency of the observed H/V, the estimated Vs profiles and the borehole profiles

may have similar peak frequencies. However, both Vs profiles are different in the profile representations. The estimated Vs profile is represented by a linear function. Meanwhile, the S-wave velocities of the borehole profiles are represented by the layered models with the power-law velocity increment in each layer. The different profile representation might cause the differences in the bedrock depths.

We further compare the average Vs from the surface to the top of the bedrock between the both profiles in Table 3.5 to confirm the cause of the bedrock depth difference. The average Vs is often used to represent the Vs of "a multi-layered over half-space" into "a layer over half-space" for analysis of the resonance frequency of a profile (Tuan et al., 2011). We calculate the average Vs (AVS) of the linear model and the layered model as follow:

$$\text{AVS (linear model)} = \frac{V_1 + V_{bedrock}}{2} \quad (3.5)$$

where V_1, and $V_{bedrock}$ are the surface S-wave velocity and the bedrock velocity of the linear model, respectively.

$$\text{AVS (layered model)} = \frac{\sum_{i=1}^{n} V_i h_i}{\sum_{i=1}^{n} h_i} \quad (3.6)$$

where V_i, h_i, n are the S-wave velocity of the *i*-th layer, the thickness of the *i*-th layer above the bedrock, and the total number of the layers above the bedrock, respectively.

The comparison in Table 3.5 shows that the estimated Vs profiles represented by linear function have a larger AVS than the borehole profiles. Therefore, it confirms the difference in the bedrock depth comparison between the estimated and the borehole profiles as shown in Figure 3.7.

Table 3.5 Comparison of average S-wave velocity from the surface to the top of the bedrock layer (AVS) between the borehole profile and the estimated Vs profile using the proposed method

Site	AVS of borehole Vs profile (m/s)	AVS of estimated Vs profile by proposed method (m/s)
Borehole 1	257	290
Borehole 2	233	292
Borehole 3	226	286

3.5.2 Effects of different bedrock velocities

We have assumed the bedrock velocity with an S-wave velocity of 500 m/s in the prior numerical test. In this section, we investigate the results of the profile estimation using different bedrock velocities. Figures 3.8 and 3.9 show the results of the theoretical ellipticities and the estimated Vs profiles with the bedrock velocities of 500 m/s, 600 m/s, and 700 m/s. We observed that the gradients of the estimated Vs profiles are slightly different from each other even though the theoretical ellipticity of each estimated profile has the same peak frequency in the ellipticity comparison. These phenomena can be explained by considering the relation of the peak frequency of a theoretical ellipticity that controlled by the ratio of an average S-wave velocity and the thickness of a Vs profile (Eq. 3.4). The variation of the bedrock velocity could cause a change in the average velocity from the surface to the top of the bedrock layer of the estimated Vs profile. Consequently, the thickness of the sediments over the bedrock that controlled by a gradient must be adjusted to produce a similar peak frequency of a theoretical ellipticity. Therefore, we found slight differences in the estimated gradient by changing the bedrock velocity as shown in Figure 3.8.

We also evaluate the effect of the different bedrock velocities by comparing the R-values of the estimated Vs profiles, as shown in Table 3.6. The R-value was calculated between the borehole profiles and the estimated Vs profiles having the

bedrock velocities of 500 m/s, 600 m/s and 700 m/s. From the R-value comparison, we observed that an increase of the bedrock velocities cause an increase of the R-value. The R-values of the estimated profiles in Table 3.6 show that the influence of different bedrock velocities may be significant for the estimated profile with additional R value 30% for a case with 200 m/s bedrock velocity difference (from 31% to 61%) as shown for Borehole 1 case. However, we observed that the influence of different bedrock velocities is insignificant for the estimated profiles at shallower depths.

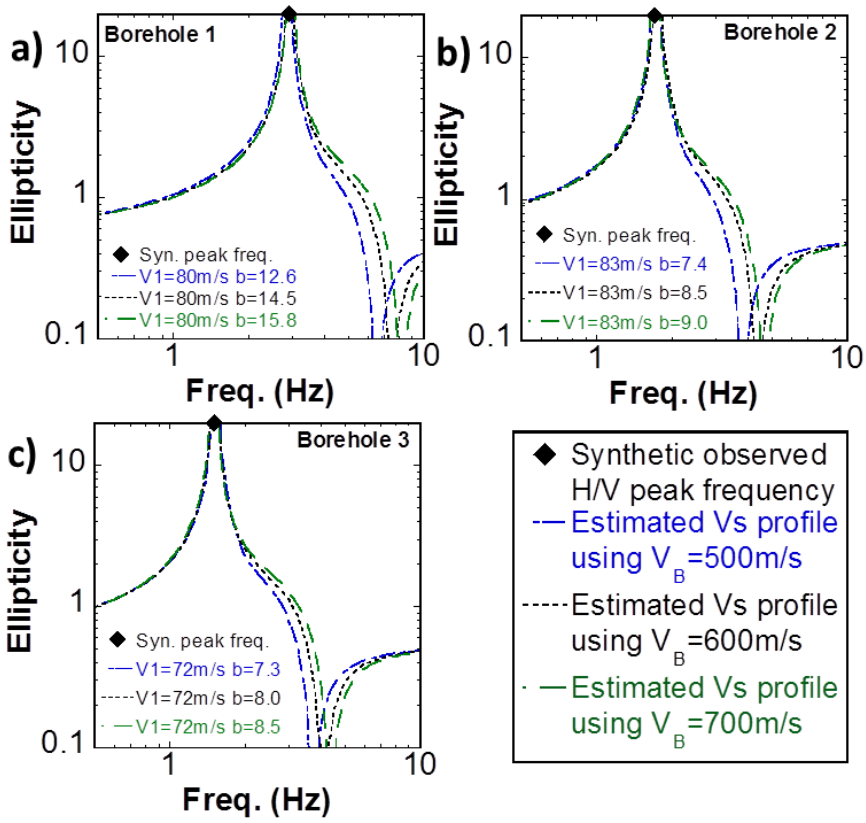

Figure 3.8 Estimation of the velocity gradient from the agreement of theoretical ellipticity peak frequency to the synthetic observed H/V peak frequency using various bedrock velocities at a) Borehole 1, b) Borehole 2, and c) Borehole 3. The diamond mark corresponds to the synthetic observed H/V peak frequency at each Borehole site. Blue, black, and green dashed lines correspond to the theoretical fundamental mode Rayleigh wave ellipticity of the estimated Vs profile using bedrock velocities of 500 m/s, 600 m/s, and 700 m/s, respectively.

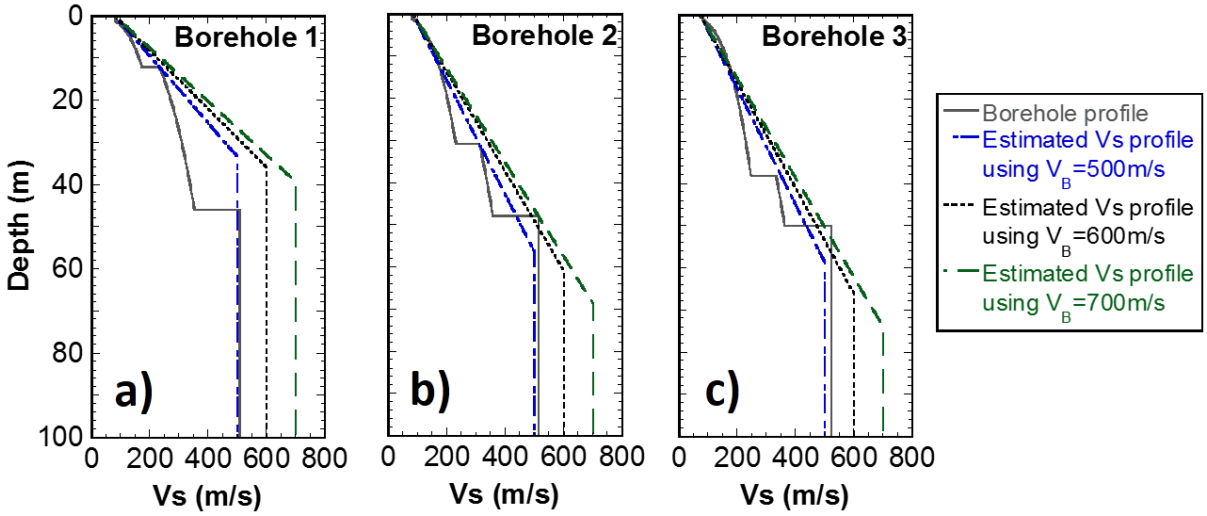

Figure 3.9 Comparison of estimated Vs profiles using a variation in bedrock velocities. The estimated Vs profiles using the proposed method with bedrock velocities of 500 m/s, 600 m/s, and 700 m/s are shown by blue, black, and green dashed lines, respectively. The borehole Vs profiles are corresponded by solid gray lines. Model parameters of the estimated Vs profiles are listed in Figure 3.8.

Table 3.6 R-values between the borehole and the estimated Vs profiles using different bedrock velocities.

Site	Averaged relative difference between the borehole and the estimated profiles		
	V_B=500m/s	V_B=600m/s	V_B=700m/s
Br. 1	31%	48%	61%
Br. 2	13%	20%	25%
Br. 3	16%	21%	25%

3.5.3 Effects of other velocity functions

In this section, we investigate the usage of different velocity-depth functions in the Vs profile estimation. We use the same V1s and H/V peak frequencies from the borehole profiles in section 3.3 for the profile estimation. The velocity functions that we consider in this analysis are the power-law function in Equation 3.7 (Parolai et al., 2002; Parolai et al., 2019) and the exponential function in Equation 3.8 (Bullen, 1965).

$$Vs(z) = V1\ (1+z)^{b2} \ldots (3.7)$$

$$Vs(z) = V1 \exp(b_3 z) \ldots (3.8)$$

where b_2 and b_3 are velocity-depth gradients for power-law and exponential functions, respectively.

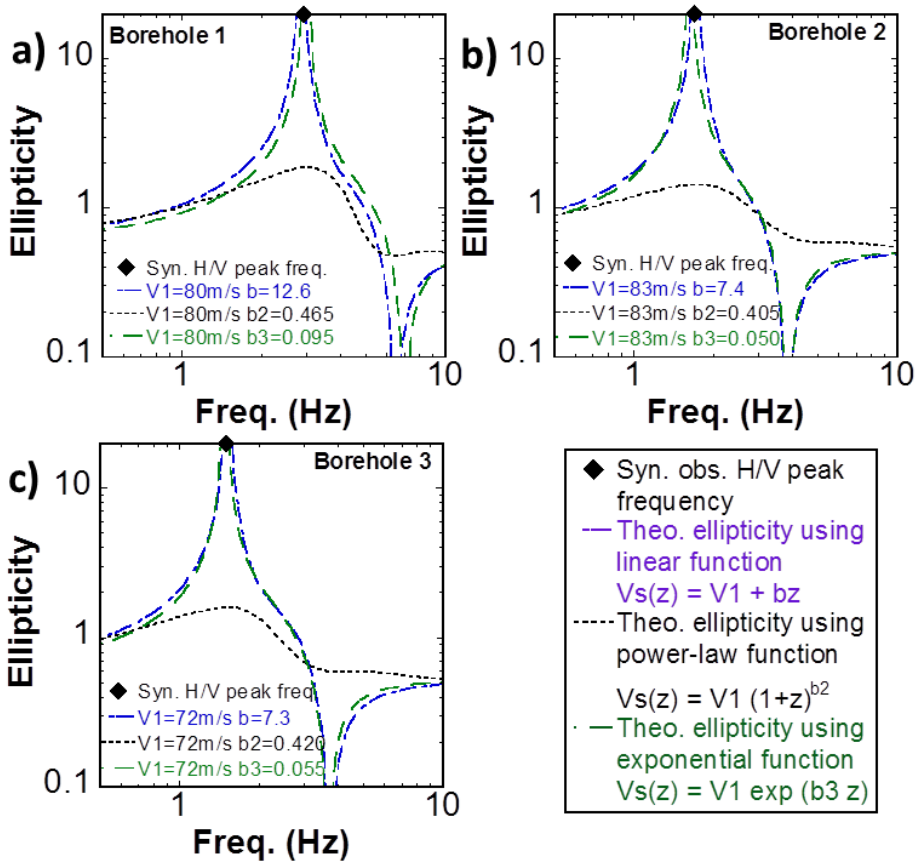

Figure 3.10 Estimation of the velocity gradient at a) Borehole 1, b) Borehole 2, and c) Borehole 3 from the agreement of the peak frequencies between the observed H/V and the theoretical ellipticities using various velocity-depth functions. The diamond mark corresponds to the synthetic observed H/V peak frequency. Blue, black, and green dashed lines indicate the theoretical fundamental mode Rayleigh wave ellipticity using the linear, power-law, and exponential functions, respectively.

Figure 3.10 shows the gradient estimations from the agreement of the peak frequencies between the observed H/Vs and the theoretical ellipticities using the various functions. We observed that the theoretical ellipticity of the power-law function has lower peak amplitude than the other functions, while the theoretical ellipticity of the exponential function has similar peak amplitude with the theoretical ellipticity of the

linear function. Since the variation of the peak amplitude ellipticities are controlled by the velocity contrast (Konno & Ohmachi, 1998), we will investigate the velocity contrast between the layers above the bedrock and the bedrock layer after estimating the Vs profiles for each function.

The estimated Vs profile for each borehole is shown in Figure 3.11. The estimated Vs profile using the power-law function overestimates the velocities of the first and the second layers of borehole 1. The velocities of the power-law model overestimate the velocities of the first layer for the boreholes 2 and 3, while the velocities of the second layer for the borehole profiles could be well approximated by the power-law model. Moreover, the estimated Vs profile using the exponential function could well approximate the velocities of the first layer for all the boreholes, whereas a large discrepancy is observed between the velocities of the exponential model and the velocities of the second layer for all the boreholes.

From the estimated Vs profiles for the individual functions, we calculated the average S-wave velocity from the surface to the top of the bedrock layer (AVS) of the estimated Vs profile for each borehole using Equation 3.6 to investigate the lower peak amplitude of the power-law function as shown in Table 3.7. We observe that the AVS values of the power-law function profiles having the highest value with AVS of around 350 m/s compare to those of the Vs profiles of the linear and the exponential functions. This indicates the velocity contrast between the layers above bedrock and the bedrock layer with a velocity of 500 m/s for the power-law function is smaller than the other functions that cause the low peak amplitude in the theoretical ellipticty.

Next, we evaluated the R-values of the estimated Vs profiles using the power-law and the exponential functions. We observed that the R-values of the power-law model are 30% at borehole 1, 28% at borehole 2, and 21% at borehole 3, which are similar R-

values with that of the Vs profiles estimated using the linear function, especially in cases of the borehole 1 and 3. However, the estimated profiles using the power-law function have a large discrepancy in the velocities of the borehole profiles in the shallow part as a disadvantage of profile representation using a power-law function. Moreover, the R-value of the exponential model is 44% at borehole 1, 28% at borehole 2, and 38% at borehole 3. A large R-value for the exponential model is due to the exponential model has a large discrepancy with the velocities of the second layer in the borehole Vs profiles. We conclude that Vs profile representation using the linear function is the lowest R-value among all the function types and has a good approximation to the borehole profiles.

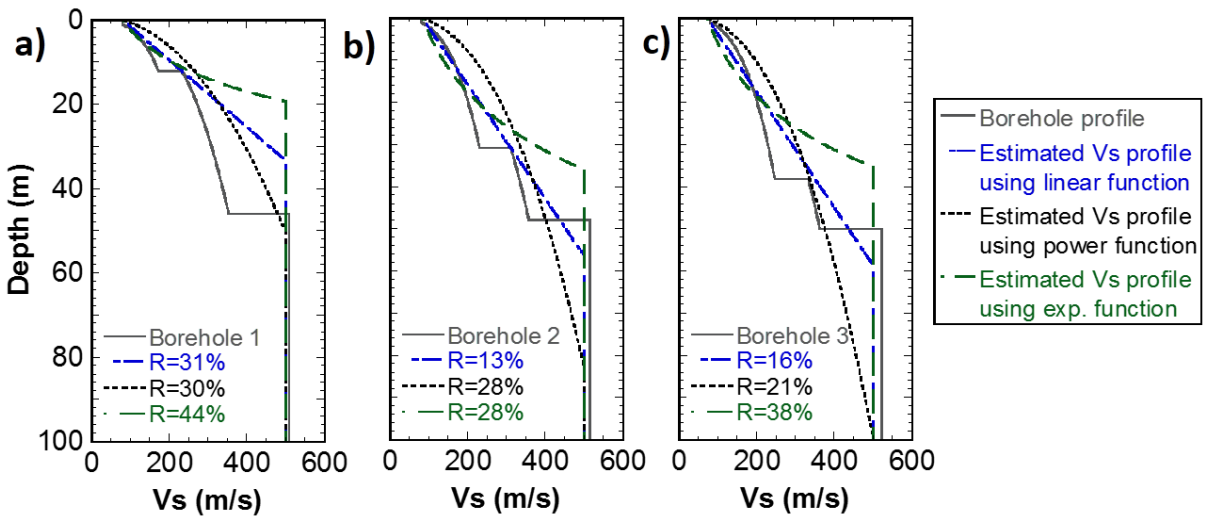

Figure 3.11 Comparison of estimated Vs profiles using various velocity-depth functions. The estimated Vs profiles from the V1-H/V data using the a) linear, b) power-law, and c) exponential functions are corresponded by solid black lines, dashed lines, and dashdotted lines, respectively. The Vs of borehole profiles are corresponded by solid gray lines. Model parameters of the estimated Vs profiles are listed in Figure 3.10.

Table 3.7 Comparison of averaged S-wave velocities from the surface to the top of the bedrock layer of estimated Vs profiles using various velocity-depth functions.

Site	AVS of estimated profile using linear function (m/s)	AVS of estimated profile using power-law function (m/s)	AVS of estimated profile using exponential function (m/s)
Borehole 1	290	350	229
Borehole 2	292	362	232
Borehole 3	286	356	220

3.5.4 Effects of random noises in observed data

As we only contaminated the synthetic V1s, and the ellipticity peak frequencies with 10% random noise for the observed data in the numerical tests using the borehole profiles, we further examine the effect of several random noise levels in the observed data to the profile estimation using the proposed method. We set random noise levels with variations of 0%, 5%, 10%, 15%, and 20% of the surface S-wave velocity (V1) and the ellipticity peak frequency (f0), as showing in Figure 3.12 for borehole 1. We then compare the R value of the estimated profile with those of the borehole profiles for each random noise level.

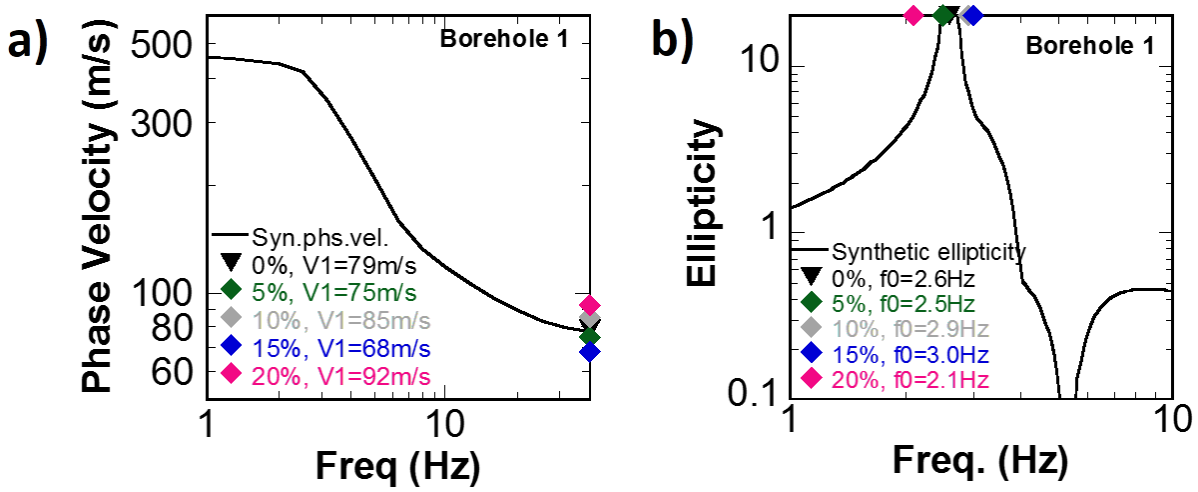

Figure 3.12 Variation of **a)** V1, and **b)** observed peak frequency of elllipticity using various level of random noise in Borehole 1. Black, green, gray, blue, and pink markers correspond to the observed data contaminated with random noise of 0%, 5%, 10%, 15%, and 20%, respectively. Please notice that the y-axis in the phase velocity graph is represented by logarithmic to clearly show the variation of V1.

Figure 3.13 shows examples of the profile comparison between the borehole and the estimated profiles in borehole 1 by using the various random noise levels. The profiles represented by solid lines in Figure 3.13a are estimated by including the random noises only for the V1s and we keep that the f0 is uncontaminated with a frequency of 2.6 Hz. Meanwhile, the estimated profiles in Figure 3.13b considered the random noises in the f0s and we set the V1 without the noise as a velocity of 79 m/s. We observed that an influence of the random noise level on the f0s causes a higher deviation in the estimated gradient than an effect of the random noise on the V1. As shown in Figure 3.13, the effect of contamination of the random noise on V1 caused the deviation of the estimated gradient from 11.7 for the uncontaminated case to 10.3 for the random noise with 20%. On the other hand, a high deviation in the estimated gradient is observed for the contamination of the random noise on f0 from 11.7 to 9.5 with the random noise of 20%.

Since the variation in the f0 causes a higher deviation in the estimated gradient of Vs profile than the variation in the V1, we can observe that the variation in the R-values caused by the random noise in f0 is higher than an influence of the random noise on the V1. The variations of the R values due to contamination of random noises with 5% to 20% in V1 indicate less than 5% from the uncontaminated case (Figure 3.13a). On the other hand, the contamination of random noises below 20% of f0 reaches the deviation of the R values below 10% relative to the uncontaminated case (Figure 3.13b). These results indicate that the noises with 15% in the parameter of f0 and 20% for the V1 are acceptable in the proposed method because the deviation of R-value is below 10% compared to the uncontaminated case.

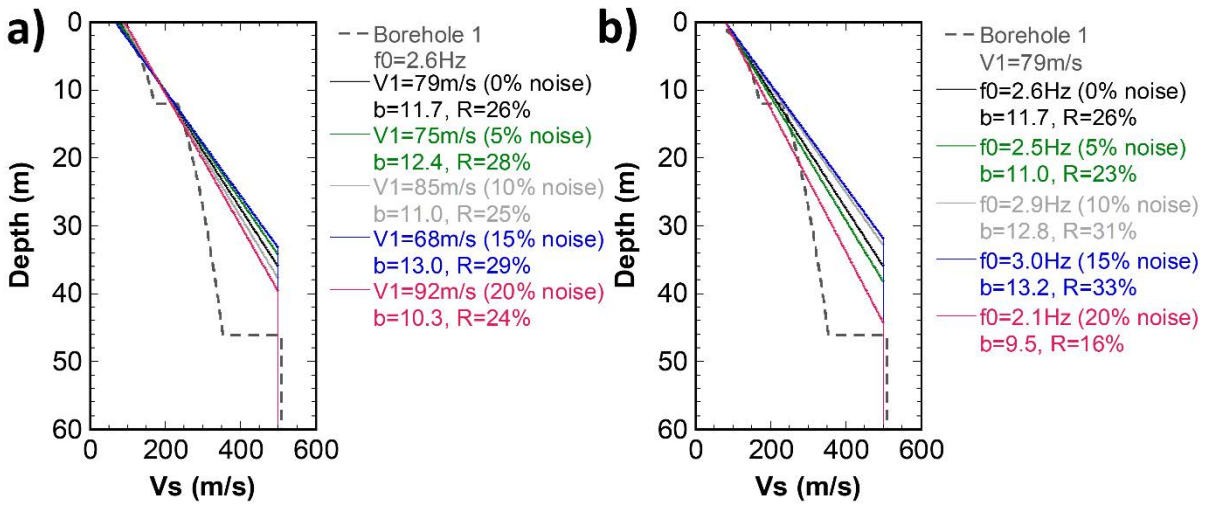

Figure 3.13 Estimated profiles in Borehole 1 case by including various random noise in the parameters of **a)** surface S-wave velocity (V1) and **b)** ellipticity"s peak frequency (f0). The V1 and f0 of uncontaminated case are using a velocity of 79 m/s and a freqeuncy of 2.6 Hz. Black, green, gray, blue, and pink lines correspond to the estimated profiles by including a random noise of 0%, 5%, 10%, 15%, and 20%, respectively to a) V1 data or in b) f0 data. Gray dashed line illustrate the borehole profile.

Furthermore, we describe the variation R values in Tables 3.8 to 3.10 to summarize the effect of the random noise levels on the f0 and V1 of the estimated profiles in boreholes 1, 2, and 3. In uncontaminated case, we observed the R-values of the estimated profiles in boreholes 1, 2, and 3 are 26%, 10%, and 11%, respectively. These results indicate that the profiles from the proposed method are in good approximation to the synthetic borehole profiles in the Bandung basin. Moreover, high R values of the estimated profiles in the borehole cases are found if the contamination random noises provide a higher observed f0 and a lower observed V1 than the uncontaminated f0 and V1 because a high velocity gradient of estimated profile is obtained. We observed the highest R value with 37% in the case of borehole 1 with a high f0 of 3.0 Hz (the case with 15% random noise) and a low V1 of 68 m/s (the case with 15% random noise).

Table 3.8 R values distribution from various random noise levels on the observed V1 and f0 in Borehole 1.

R-values (%) in Borehole 1	Random noise in obs. f0	0%	5%	10%	15%	20%
Random noise in obs. V1	f0 (Hz) / V1(m/s)	2.6	2.5	2.9	3.0	2.1
0%	79	26	23	31	33	16
5%	75	28	26	33	35	17
10%	85	25	22	30	32	14
15%	68	29	27	35	37	20
20%	92	24	21	28	30	13

Table 3.9 R values distribution from various random noise level on the observed V1 and f0 in Borehole 2.

R-values (%) in Borehole 2	Random noise in obs. f0	0%	5%	10%	15%	20%
Random noise in obs. V1	f0 (Hz) / V1(m/s)	1.5	1.6	1.7	1.4	1.3
0%	79	10	10	12	9	10
5%	81	9	10	12	8	10
10%	83	9	10	12	8	10
15%	89	9	9	11	9	10
20%	93	9	9	10	9	10

Table 3.10 R values distribution from various random noise level on the observed V1 and f0 in Borehole 3.

R-values (%) in Borehole 3	Random noise in obs. f0	0%	5%	10%	15%	20%
Random noise in obs. V1	f0 (Hz) / V1(m/s)	1.45	1.4	1.5	1.2	1.7
0%	79	11	10	13	10	18
5%	75	11	11	16	10	21
10%	72	12	12	16	11	21
15%	68	14	13	19	12	24
20%	65	16	14	19	12	24

3.6 Investigation of difficult cases in assumption of linear velocity function

In this section, we apply numerical tests using several synthetic profiles that have a different represention with the linear velocity function to investigate difficult cases for applying the proposed method. The following synthetic Vs profiles are used as shown in Figure 3.14.

1. Two-layer profile with high velocity contrast.
2. Three-layer profile with velocity increasing with depth.
3. Three-layer profile containing a thick second layer.
4. Three-layer profile with velocity inversion in a soft second layer.
5. Profile represented by two linear velocity gradients (i.e., bi-linear model).
6. Profile with power-law velocity gradient.
7. Profile with exponential velocity gradient.

We define a profile consist of a layer with velocity of 100 m/s and thickness of 20 m over a half-space layer in the first case (Figure 3.14a). In the second and the third cases (Figures 3.14b and 3.14c), we define profiles represented by two-layers over a bedrock using S-wave velocities of 100 m/s and 220 m/s for the first and second layers. The thicknesses of the first layer are set using 10 m, while the second layer thicknesses of the second and third profiles are set using 20 m and 100 m, respectively. The effect of a thick constant velocity layer is evaluated in the third case. We also set a profile that contains an inverse velocity layer in the forth case (Figure 3.14d). The velocities of the first and the second layer are 200 m/s and 150 m/s. Moreover, the profile represented by two linear velocity gradients is defined in the fifth case (Figure 3.14e). We set the gradient of the shallow part is higher than the deep part. The model parameters in the profile of two linear gradients consist of first gradient (b1), second gradient (b2), surface

S-wave velocity (V1), bedrock S-wave velocity (Vb), and middle S-wave velocity (Vmid). Vmid is defined as an intersection point of the two gradients. The synthetic profiles represented by the power-law and the exponential functions in the sixth and seventh cases (Figures 3.14f and 3.14g) are set by having a thickness of 50 m with V1 of 100 m/s. The bedrock layer of all the synthetic profiles is set by using velocity of 500 m/s.

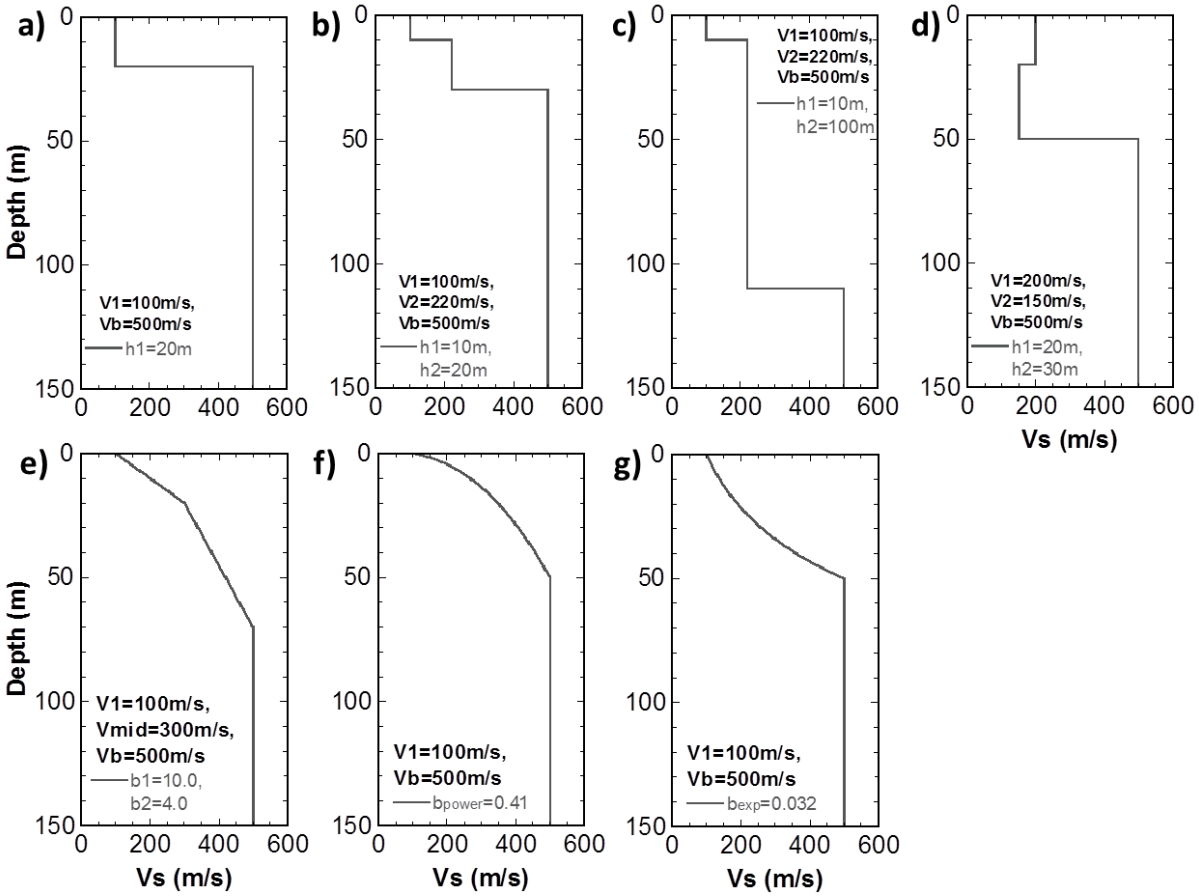

Figure 3.14 Synthetic profiles used in numerical tests for investigation of the difficult cases. a) Two-layer profile with high velocity contrast, b) three-layer profile with velocity increasing with depth, c) three-layer profile containing a thick second layer, d) three-layer profile with velocity inversion in a soft second layer, e) profile represented by two linear velocity gradients, f) profile represented by the power-law function, and g) profile represented by the exponential function.

We then use all the synthetic profiles to generate the synthetic ellipticities as illustrated by solid lines in Figure 3.15. We utilize the peak frequencies of the synthetic ellipticities and the surface S-wave velocities (V1s) of the synthetic profiles to estimate the Vs profiles using the proposed method. We did not contaminate the synthetic peak frequencies of the ellipticity with the random noise in these cases to investigate the features of the proposed method. The theoretical ellipticities to estimate the gradients are shown by black dashed lines in Figure 3.15.

The profile comparison between the synthetic profiles and the estimated ones using the proposed method can be seen in Figure 3.16. We observed the distinct profile difference on the cases of two-layer profile (case 1), the profile with the thick second layer (case 3), and the profile with an inverse velocity layer (case 4) as correspond with high R-values more than 20% in Table 3.11. The velocity variation of the estimated profile that represented by linear velocity gradient is difficult to approximate a constant velocity layer in the two-layer case (Figure 3.16a), the thick second layer with a constant velocity (Figure 3.16c), and especially to the inverse velocity layer (Figure 3.16d). However, the estimated profile in the case of three-layer profile with velocity increase with depth (Figure 3.16b) could approximate the velocity variation in of the first and the second layers of the synthetic profile. In the profile with two linear gradients (Figure 3.16e), we observed that the gradient of the estimated profiles using the proposed method are similar to the first gradient of the synthetic profile. The estimated profile could not anticipate the second gradient in the deeper part of the synthetic profile. Furthermore, the profile comparison in the power-law model (Figure 3.16f) shows that the velocity variation of the estimated profile is slightly lower than the synthetic profile in the shallow depths of 0 m to 30 m. Moreover, the velocity variation of the synthetic exponential model (Figure 3.16g) in the shallow depths of 0 m to 30 m is well

approximated by the estimated profile, whereas the distinct profile difference in the comparison is observed in the deep depths of more than 30 m.

The comparison of the synthetic and the theoretical phase velocities of the estimated profiles using the proposed method are shown in Figure 3.17 as confirmation of the estimated profiles. We observed that the theoretical phase velocity has a difficulty to match a constant synthetic phase velocity at frequencies of 3 to 6 Hz in Figure 3.17a and a plateau feature of the synthetic phase velocity at frequencies of 1.3 to 3 Hz in Figure 3.17c. The plateau feature is characterized by a constant phase velocity of 200 m/s that correspond to the existence of the thick layer of the synthetic profiles. The plateau feature in the phase velocity is clearly observed when a profile contains a significant thick layer with a constant velocity. Therefore, we did not observe the plateau feature in Figure 3.17b even though the second layer thickness of this model is 20 m which is twice of the first layer thickness. A large discrepancy in the phase velocity comparison is also shown in Figure 3.17d due to a present of the inverse velocity layer. In addition, the phase velocity comparison for the cases of the bi-linear models and the exponential model in Figures 3.17e and 3.17g, we did not observed any large discrepancies between the theoretical phase velocities of the estimated profiles and the synthetic phase velocities, even though in their profile comparisons (Figures 3.16e and 3.16g) indicating the discrepancies at the deep depths. Moreover, the large discrepancy in the phase velocity comparison is observed in the power-law model case in Figure 3.17f. The theoretical phase velocity of the estimated profile has a lower velocity in frequencies of 4 to 40 Hz than the synthetic phase velocity of the power-low model. This discrepancy corresponds to the profile difference in the shallow depth of 0 to 30 m in Figure 3.16f. Therefore, these results indicate that the estimated profile using the

proposed method has a good accuracy to estimate the shallow part of the synthetic profile, if the large discrepancies are not observed in the phase velocity comparison.

We conclude the proposed method, which assuming the estimated profile using the linear function, has difficulties to approximate the synthetic profile that represented by power-law function, and the profile containing a thick constant velocity layer, or a high velocity contrast layer, or an inverse velocity layer. These difficult cases are identified by a large discrepancy in a phase velocity comparison. Therefore, these results confirm a requirement of observed phase velocities at representative sites of an investigated area if the borehole (P-S logging) data are unavailable to examine the usage of the profile representation using the linear function before the further usage of the proposed method in the Vs profiling.

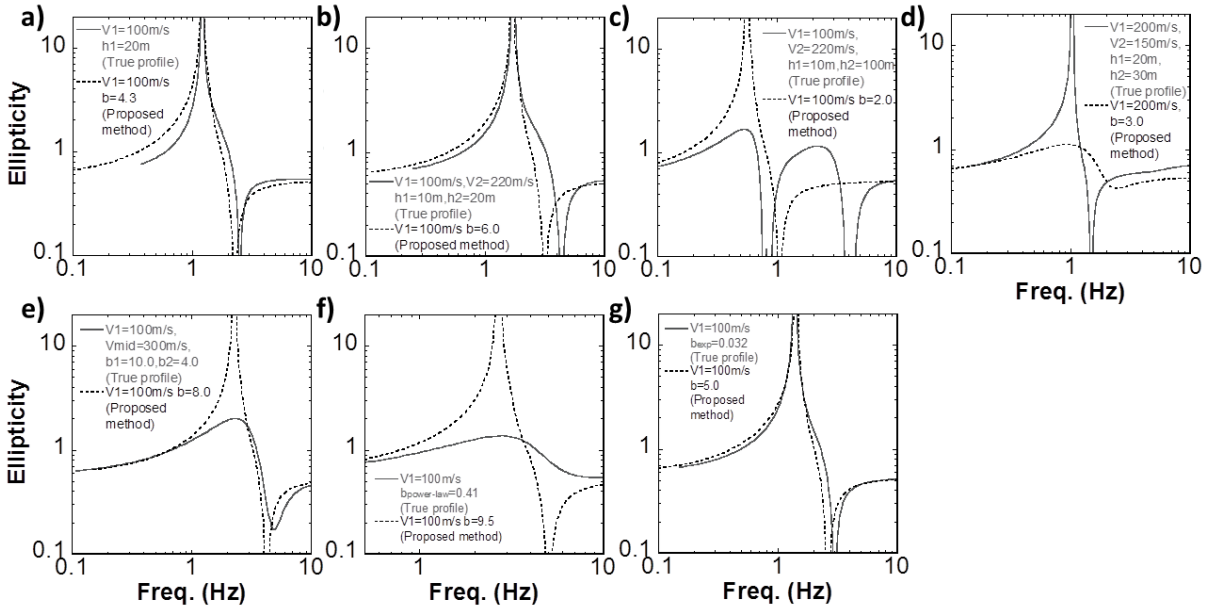

Figure 3.15 Fundamental mode of Rayleigh wave ellipticities comparison for the cases of a) two-layer profile with high velocity contrast, b) three-layer profile with velocity increasing with depth, c) three-layer profile containing a thick second layer, d) three-layer profile with velocity inversion in a soft second layer, e) profile represented by two linear velocity gradients, f) profile represented by the power-law function, and g) profile represented by the exponential function. Solid gray and dashed black lines correspond to the synthetic ellipticity of Rayleigh wave fundamental mode of the synthetic profile, and theoretical ellipticity of the estimated profile using the proposed method.

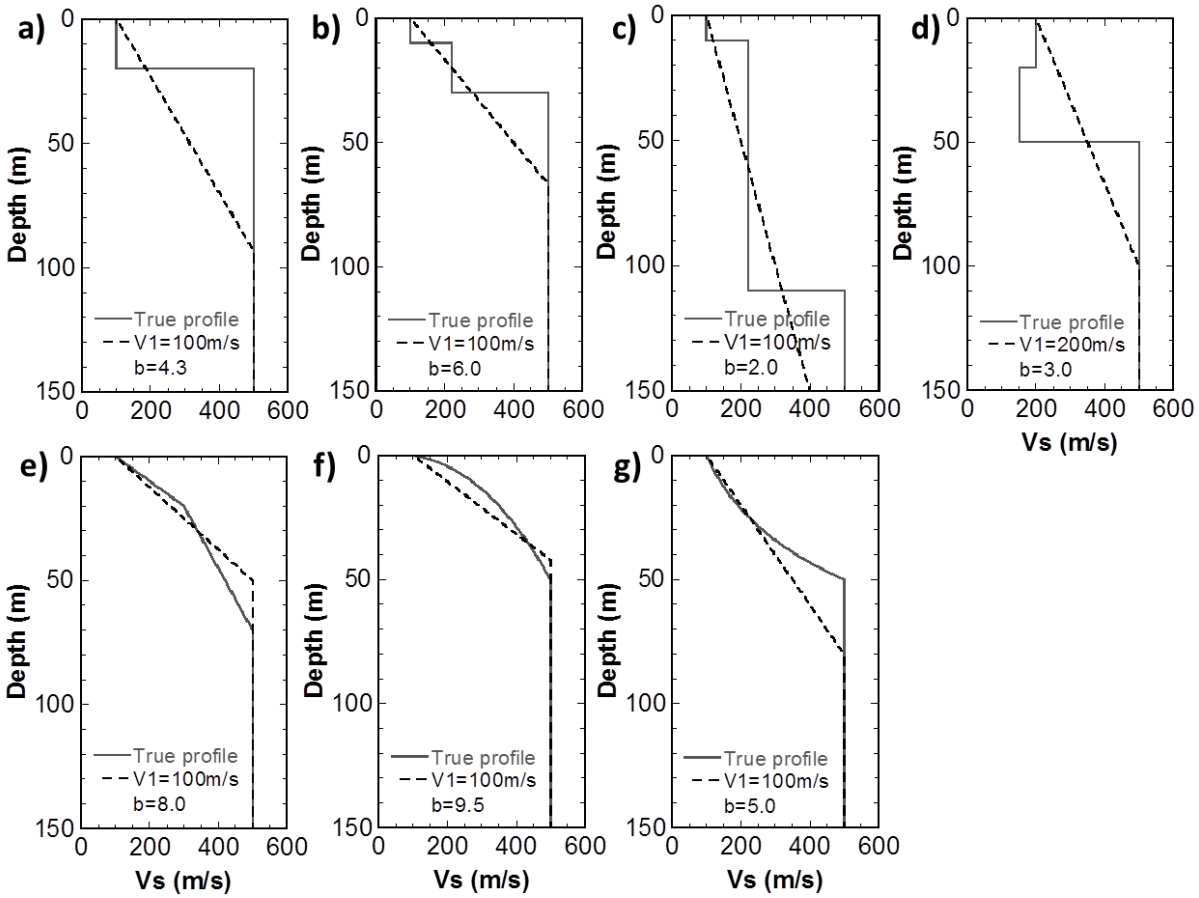

Figure 3.16 Comparison between the synthetic and the estimated profiles using the proposed method in the cases of a) two-layer profile with high velocity contrast, b) three-layer profile with velocity increasing with depth, c) three-layer profile containing a thick second layer, d) three-layer profile with velocity inversion in a soft second layer, e) profile represented by two linear velocity gradients, f) profile represented by the power-law function, and g) profile represented by the exponential function. Solid gray and dashed black lines are the synthetic profile, and the estimated profile using the proposed method, respectively.

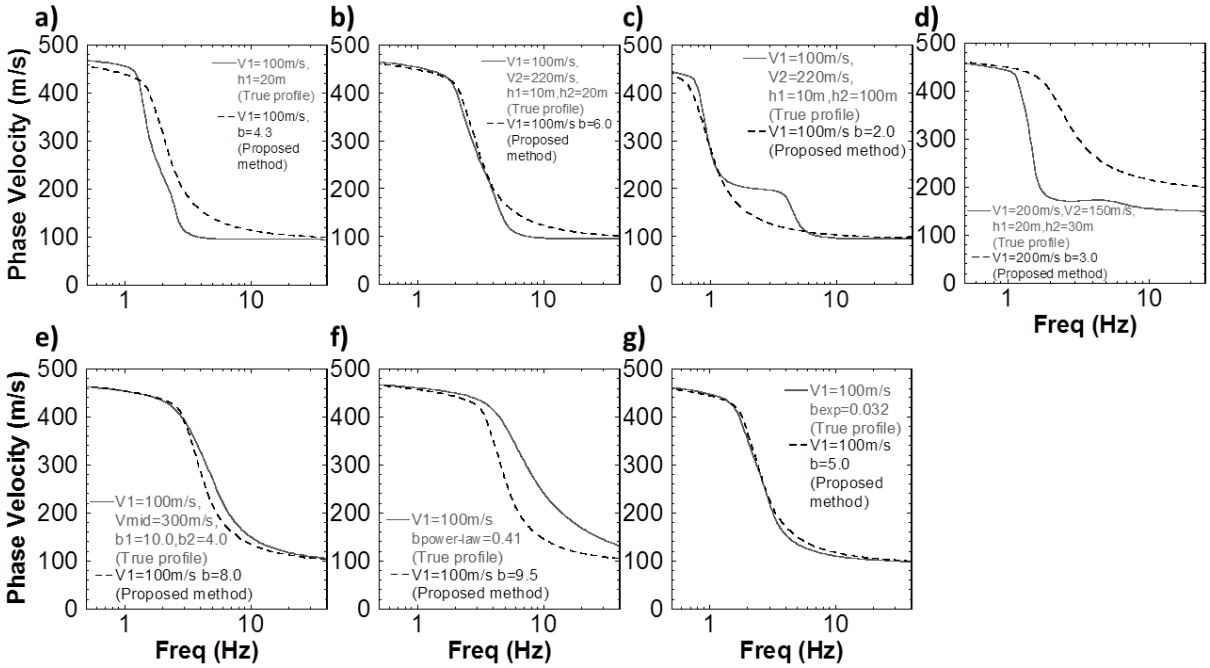

Figure 3.17 Phase velocity comparison for the cases of a) two-layer profile with high velocity contrast, b) three-layer profile with velocity increasing with depth, c) three-layer profile containing a thick second layer, d) three-layer profile with velocity inversion in a soft second layer, e) profile represented by two linear velocity gradients, f) profile represented by the power-law function, and g) profile represented by the exponential function. Solid gray and dashed black lines correspond to the synthetic phase velocity of Rayleigh wave fundamental mode of the synthetic profile, and theoretical phase velocity of the estimated profile using the proposed method.

Table 3.11 Evaluation of R values between the synthetic and the estimated profiles in investigation of difficult cases

Synthetic profile	R value of the profile estimated using the proposed method (%)
Two-layer profile V1=100m/s, h1=20m	44
Three-layer profile V1=100m/s, V2=220m/s, h1=10m, h2=20m	20
Three-layer profile V1=100m/s, V2=220m/s, h1=10m, h2=100m	22
Three-layer profile V1=200m/s, V2=150m/s, h1=20m, h2=30m	68
Two linear velocity gradients profile V1=100m/s, Vmid=300m/s b1=10.0, b2=4.0	9
Power-law gradient profile $b_{power\text{-}law}$=0.41	13
Exponential gradient profile b_{exp}=0.032	10

Chapter 4 Array measurements of microtremors in Bandung basin

4.1 Objective

4.2 Location of microtremor arrays

4.3 Estimation of phase velocity

4.4 Evaluation of linear velocity increase assumption

4.5 Estimated Vs profiles

4.1 Objective

In this chapter we explained results of the microtremor array measurements as the conventional method to delineate observed phase velocities in the Bandung basin. We describe the array measurements on the field, the distribution of the observed phase velocities, and the estimated Vs profiles. We furthermore confirm the profile representation using the linear function with the observed phase velocities and evaluate the suitability of the defined bedrock velocity for the estimated profiles in the basin.

4.2 Locations of microtremor arrays

We conducted microtremor array measurements at 29 sites in the Bandung basin to acquire the Rayleigh wave phase velocities. We could conduct the array measurements since there is an international collaboration between Tokyo Institute of Technology and Bandung Institute of Technology under the SATREPS project with theme of „Multi-disciplinary Hazard Reduction from Earthquakes and Volcanoes in Indonesia". Therefore, all the instruments required in the array measurements were provided from Tokyo Institute of Technology. There are two-measurement campaigns in 2009 with measurements at 15 sites and in 2011 at 14 sites. The locations and coordinates of the array measurement sites are shown in Figure 4.1 and in Table 4.1. The observation sites are mostly distributed in the basin region. 9 sites are located on the volcanic region and 20 sites are situated on the lake deposit. At each site, microtremors were temporarily observed using seven vertical microtremor sensors arranged into two arrays. Each array has a configuration of two equilateral triangles with a common central station. The instruments used in the measurements are the vertical V243S accelerometers produced by Mitsutoyo Corporation. The logger manufactured by Hakusan Corporation, with a 24-bit analogue-to-digital (A/D) converter, can digitize acceleration data at every 0.01s. The sampled data from each logger were transmitted to a laptop PC in real time across a

wireless LAN, to store and monitor the records. Coherent microtremors data at frequencies lower than 30 Hz can be well recorded with this observational system. This system is the same used in Grutas & Yamanaka, (2012), Karagoz et al., (2015), Özmen et al., (2017), and Zaineh et al., (2012). Figure 4.2 shows an example of the two array configurations with triangle side lengths of 16-8 m and 4-2 m to measure the vertical microtremors at L1. The lengths of the triangle sides for the arrays at each site are between 1 and 16 m as listed in Table 4.1. It takes around 1.5 to 2 hours to observe the microtremor data at each site, including 15 to 20 minutes to configure the instruments for the one triangle side length array.

Table 4.1 List of site names, coordinates, triangle array side lengths, estimated V1s, estimated gradients, and Vs30s of the microtremor array measurements.

Site	Long (Deg)	Lat (Deg)	Surface geology*	Triangle array side lengths (m)	V1 (m/s)	Gradi-ent (1/sec)	Vs30 (m/s)	Fund. peak freq. (Hz)	Ampl. factor of fund. Peak	Avg. ampl. (0.4-10 Hz)
L1	107.54831	–6.98700	LD	16–2	113	4	166	1.1	5.5	4.0
L2	107.63569	–6.98217	LD	16–2	96	4	148	1.0	5.9	4.2
L3	107.69817	–6.98383	LD	16–2	73	2	100	0.4	6.8	4.5
L4	107.73278	–7.00911	LD	16–2	94	2	122	0.5	6.0	4.2
L5	107.76392	–6.96250	LD	16–2	78	5	140	1.1	6.6	4.5
L6	107.68456	–6.93011	LD	12–1.5	82	5	144	1.2	6.5	4.4
L7	107.80275	–6.97319	LD	16–2	162	2	190	0.7	4.4	3.5
L8	107.551	–6.95297	VD	12–1.5	-	-	-	-	-	-
L9	107.62064	–6.94414	VD	16–2	-	-	-	-	-	-
L10	107.65167	–6.91114	VD	16–2	78	16	243	3.6	6.6	3.7
L11	107.72972	–6.94278	LD	16–2	60	3	98	0.6	7.6	5.0
L12	107.58125	–7.01783	LD	16–2	80	6	153	1.4	6.5	4.4
L13	107.66058	–7.02250	LD	16–2	60	5	120	1.0	7.5	5.0
L14	107.77358	–7.00544	LD	16–2	-	-	-	-	-	-
L15	107.60972	–6.88978	OV	12–1.5	105	23	321	6.1	5.7	3.0
S1	107.62413	–6.85388	OV	16–2	115	18	303	4.9	5.4	3.0
S2	107.52402	–6.86121	VD	12–1.5	125	13	275	3.8	5.2	3.1
S3	107.56903	–6.92402	VD	16–2	103	27	337	7	5.7	2.9
S4	107.56071	–6.97098	LD	8–1	67	39	336	8.3	7.1	3.0
S5	107.60851	–7.01028	LD	16–2	70	7	151	1.5	7	4.5
S6	107.59328	–7.05080	LD	12–1.5	102	7	188	1.8	5.8	3.9
S7	107.54739	–7.04067	LD	12–1.5	91	13	234	3.2	6.1	3.6
S8	107.52989	–7.01270	OV	12–1.5	199	15	369	6.5	3.9	2.6
S9	107.66465	–6.95280	LD	12–1.5	97	19	289	4.8	5.9	3.2
S10	107.72142	–7.02625	LD	12–1.5	88	4	139	0.9	6.2	4.4

Site	Long (Deg)	Lat (Deg)	Surface geology*	Triangle array side lengths (m)	V1 (m/s)	Gradi-ent (1/sec)	Vs30 (m/s)	Fund. peak freq. (Hz)	Ampl. factor of fund. Peak	Avg. ampl. (0.4-10 Hz)
S11	107.75982	–7.06068	LD	16–2	62	13	196	2.7	7.4	4.2
S12	107.76817	–7.03273	LD	16–2	115	3	156	0.8	5.4	4.0
S13	107.72718	–6.97072	LD	16–2	-	-	-	-	-	-
S14	107.74171	–6.93433	YV	12–1.5	164	21	370	7.5	4.4	2.6

*Surface geology: LD: Lake deposit, VD: Volcanic deposit, OV: Old volcanic product, YV: Young volcanic product.

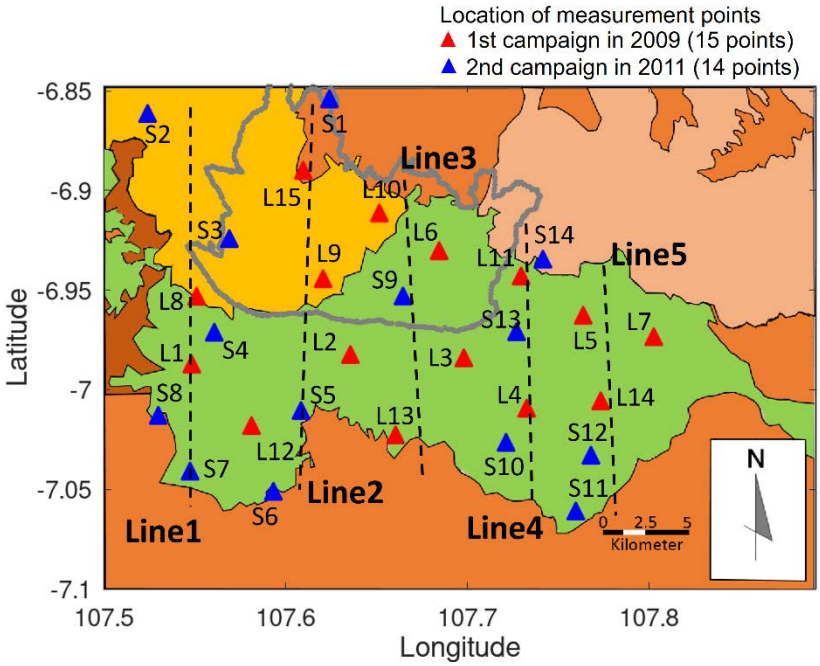

Figure 4.1 The location of microtremor array measurement points on the surface geological map of Bandung basin which represented by triangles. The red and blue triangles represent the measurement points of joint campaigns in 2009 and 2011 between Tokyo Institute of Technology and Bandung Institute of Technology under SATREPS project with the theme of „Multi-disciplinary Hazard Reduction from Earthquakes and Volcanoes in Indonesia“. The legend for the surface geological map can be seen in Figure 1.3. Lines 1 – 5 correspond to the cross-sections of the estimated Vs profiles in Figure 4.6.

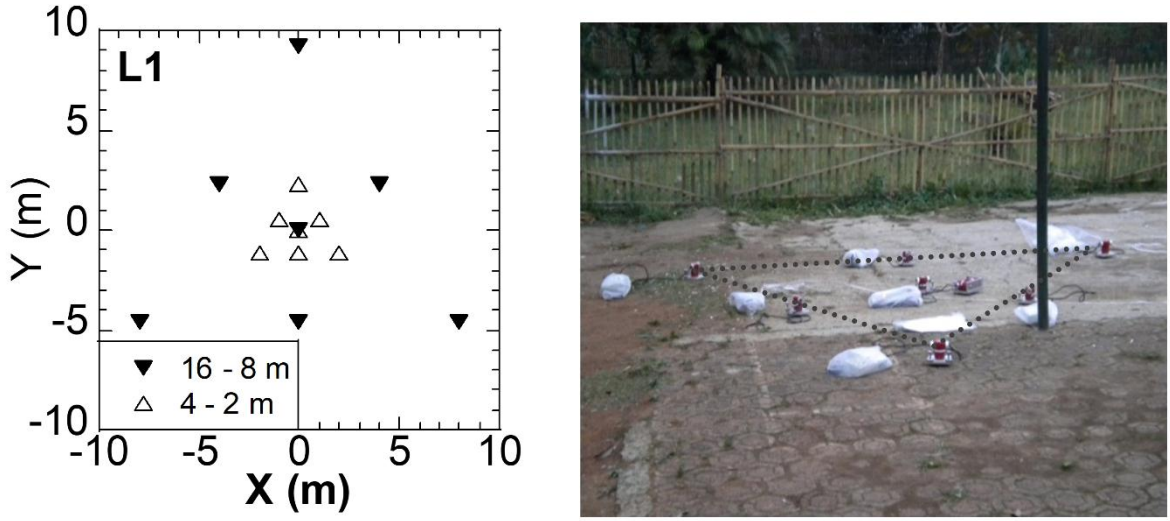

Figure 4.2 Example of the array configuration in microtremor observation (left), and a documentation of an array deployment (right) in one of the site. The photo shows the array with spacing 4–2 m. The array consists of seven vertical microtremor sensors and the loggers (covered by plastic bags) for observation of Rayleigh wave phase velocity.

4.3 Estimation of phase velocity

We applied the spatial autocorrelation (SPAC) method (Okada, 2003) to retrieve phase velocity of Rayleigh waves from the vertical microtremors. The recorded microtremors were divided into time segments with a length of 81.92 seconds after removing parts with artificial noises generated locally from some disturbances such as vehicles moving nearby the sensors during the measurements. An example of a microtremor records segment is shown in Figure 4.3(a). Then, each segment was converted into the frequency domain (ω) to calculate the SPAC coefficient, $\rho(\omega,r)$ using equation 4.1.

$$\rho(\omega,\mathrm{r}) = \frac{1}{n}\sum_{i=1}^{n}\frac{Re(\hat{S}_{0r}(\omega,\mathrm{r}))}{\sqrt{\hat{S}_0(\omega)\hat{S}_r(\omega)}}, \qquad (4.1)$$

where n is the number of station pairs with same inter-station distance, r, and $Re(\hat{S}_{0r}(\omega,r))$ is the real component of the cross-spectra of the microremor records

between the station pairs. $\hat{S}_0(\omega)$ and $\hat{S}_r(\omega)$ are power-spectra of the records used for $\hat{S}_{0r}(\omega, r)$ calculation. After these calculations for all the segments, the SPAC coefficients for the same distances were averaged. We used 8 to 15 segments to obtain averaged SPAC coefficients in our analysis. Figure 4.3(b) shows an example of the SPAC coefficients obtained at L6 with triangle side lengths of 12 and 6 m. A high SPAC coefficient is observed at a frequency of 1.2 Hz. The obtained averaged SPAC coefficients are used further to extract the observed phase velocities the relation of the SPAC coefficient and the Bessel function of the first kind and the order zero ($J_0(x)$).

$$\rho(\omega, r) = J_0\left(\frac{\omega r}{c(\omega)}\right), \qquad (4.2)$$

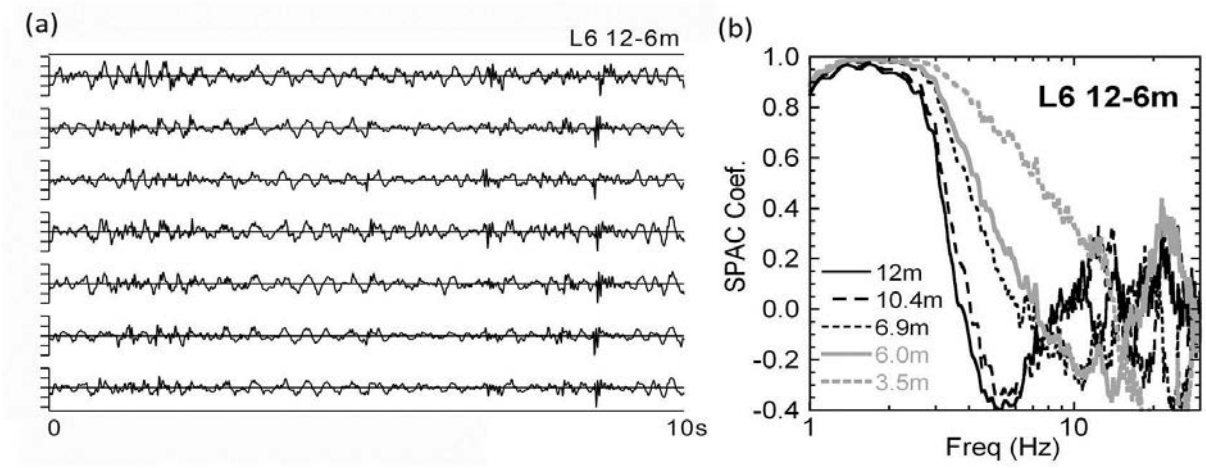

Figure 4.3 (a) An example of the vertical-component records, and (b) Obtained SPAC coefficients at L6 from triangle arrays with a side length of 12 and 6 m.

Observed phase velocities from the microtremor array measurements at the 29 sites are shown in Figure 4.4. The figure contains 5 panels showing the variation of phase velocities in the basin along the cross-section lines in Figure 4.1.

We observe most of the sites along Line 1 have a high phase velocities above 250 m/s in a high frequency range above 5 Hz except for L1 located on the central part. A

highest value of the phase velocity can be observed at S8 because the site is situated on the Beser formation which is the oldest volcanic rock in the basin (Bronto et al., 2006).

The phase velocities in Line 2 are high over 280 m/s at frequencies higher than 9 Hz at S1, L15, and L9 located on the volcanic deposits in the northern part of the basin. Meanwhile, a trend of the phase velocities below 120 m/s at frequency higher than 10 Hz and velocities higher than 200 m/s at frequencies of 2 to 4 Hz are observed at L2, S5, L12, and S6 located on the lacustrine sediments.

The observed phase velocities on the lacustrine and the volcanic deposits can also be seen at Lines 3, 4, and 5. The phase velocity at a frequency of 10 Hz shows that the sites located on the volcanic deposits have a higher value such as at L10 and S14 than those on the lacustrine deposits such as L4 and L14. High phase velocities are obtained at L13, S10, and S11 in the southern edge of the basin.

We further use all the observed phase velocities to evaluate the appropriateness of the linear velocity increase assumption in the Bandung basin. However, we notice that the feature of the observed phase velocities at L8, L9, L14, and S13 having a narrow velocity variation below 50 m/s in the entire frequency range. Such type of observed phase velocities will be difficult to constrain model parameters for the solution in an inversion because the velocity gradient of an estimated profile cannot be well resolved with such limited data. Therefore, we conduct the evaluation at the remained 25 sites.

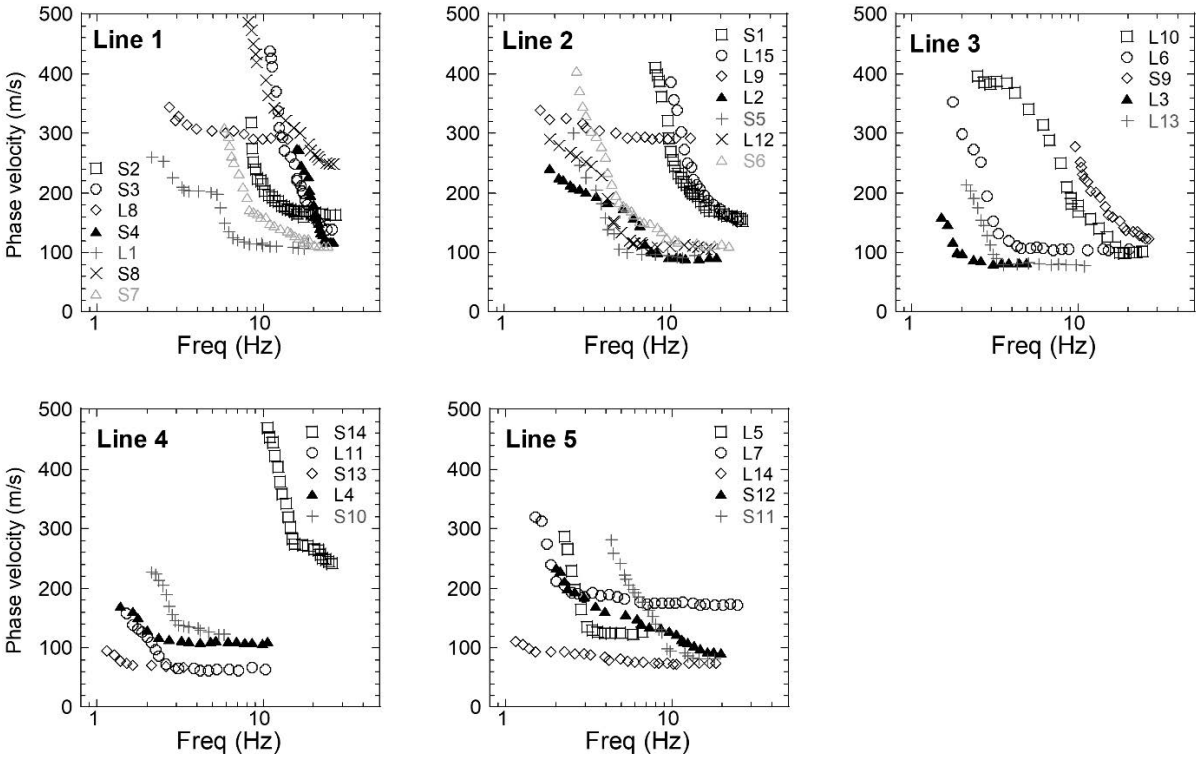

Figure 4.4 Observed phase velocities from the microtremor array surveys in the Bandung Basin. The phase velocities are grouped in Lines 1 to 5. The locations of Lines 1 to 5 are shown in Figure 4.1.

4.4 Evaluation of linear velocity increase assumption

The procedure to evaluate the appropriateness of the Vs profile representation using the linear function in the Bandung basin has been described in the section of 2.3 and 3.4.1. We show the phase velocity comparison between the observed phase velocity and the theoretical one using of the lowest misfit in Figure 4.5. We observed that the theoretical phase velocities of the lowest misfit models at 23 of 25 sites (except at L1, and L2 sites) could fit the observed phase velocities indicating an appropriateness of the Vs profile representation using the linear function in the Bandung basin. Slight discrepancy between the theoretical and the observed phase velocities can be found at frequencies of 4 to 5 Hz at L1 and L2 sites. The observed phase velocities show the plateau features at these frequencies indicating an existence of a thick layer with a

constant velocity. Such features of the models cannot be well fitted by the linear represented profile as described in the section 3.6 of numerical tests. We also show the appropriateness of the defined bedrock velocity of 500 m/s in the basin because the theoretical phase velocities of the estimated profiles could explain sufficiently the observed phase velocities in a low frequency range at most of the sites, such as phase velocity comparisons at L15, S1, S2, and S3 in a frequency range of 8 to 10 Hz.

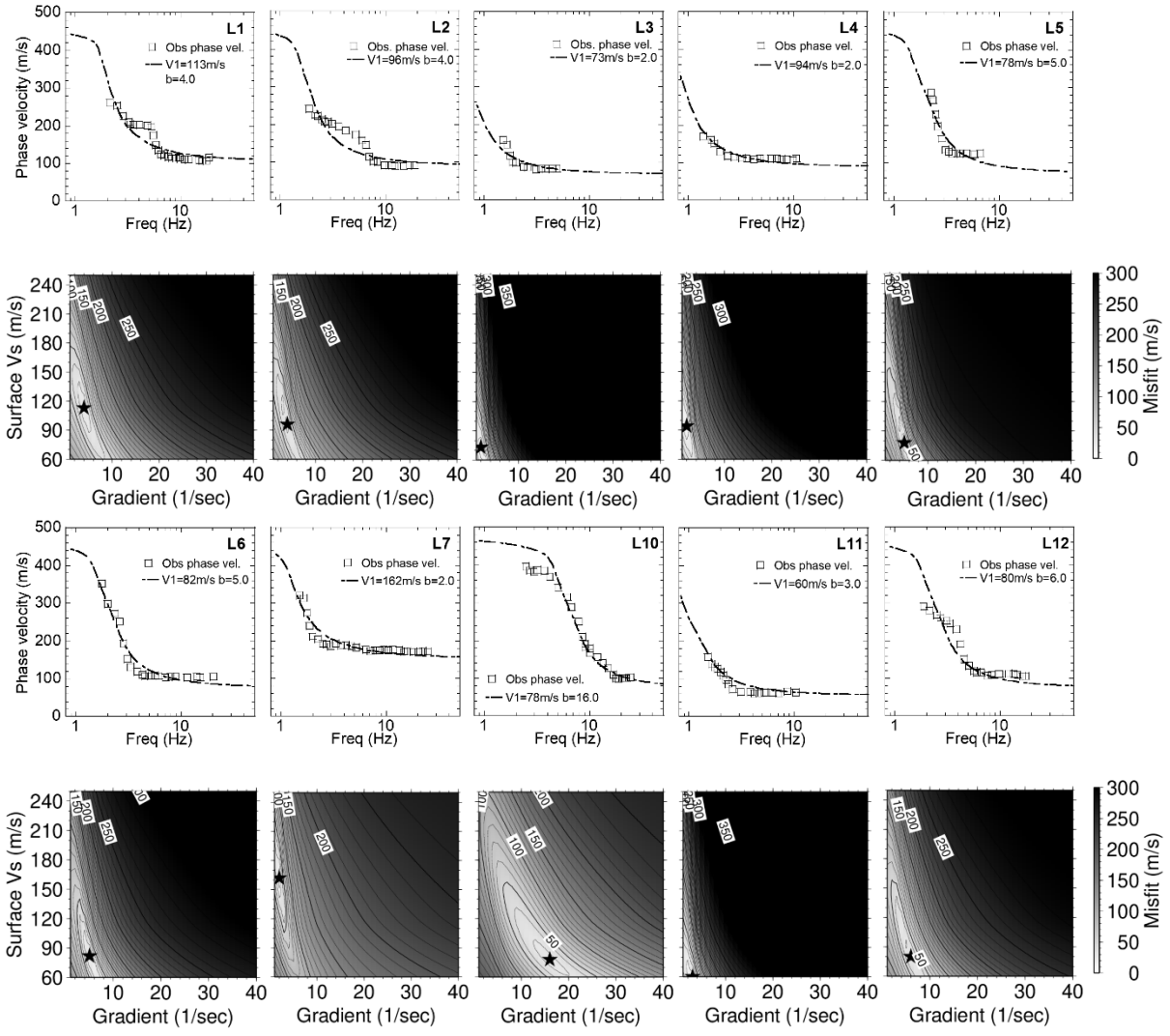

Figure 4.5 (continued)

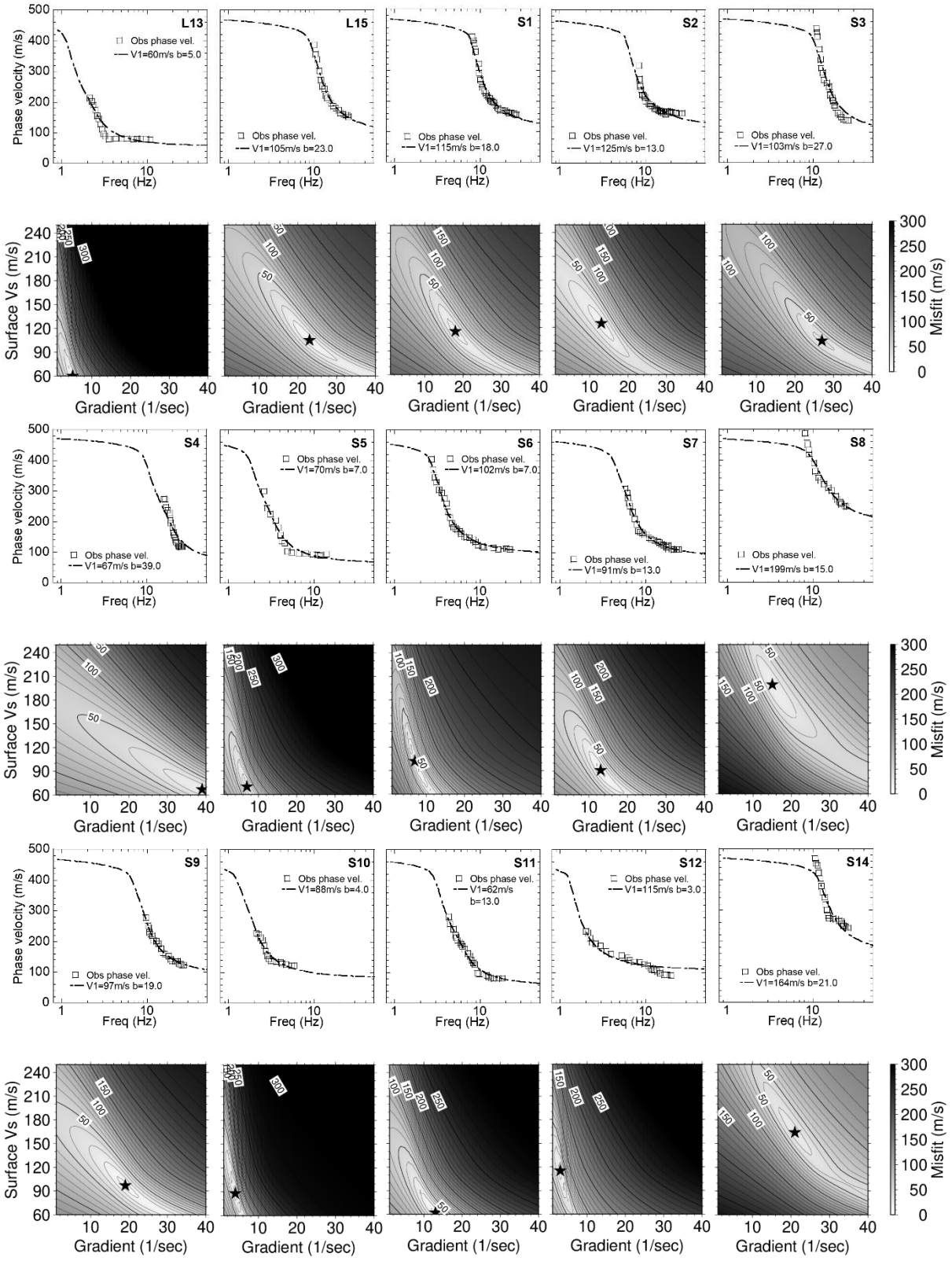

Figure 4.5 Phase velocity comparison (above) between the observed phase velocities from the microtremor array survey and the theoretical phase velocity of the lowest misfit model using grid search evaluation (bottom). Square mark and dashed line in the above figure are observed phase velocity and theoretical phase velocity of the lowest misfit model parameter (V1 and b), respectively. Star mark and countour map indicate the V1-b pair that gives the lowest misfit to the observed phase velocity and distribution of misfit value between the observed phase velocity and the theoretical phase velocity of each V1-b pair.

4.5 Estimated Vs profiles

The V1 and the gradient of the lowest misfit model from the observed phase velocities in the section of 4.4 are decided as the estimated Vs profiles. All the estimated Vs profiles are shown in Figure 4.6.

We observed in Line 1 that the estimated Vs profile has thick sediments only at L1 which is located on the lacustrine deposit in the central part of the basin. For the estimated Vs profiles at the other sites in Line 1 such as S2, S3, and S8 that located in volcanic deposits and S7 that located at edge of basin are characterized with thin sediments. Furthermore, the estimated Vs profile at S4 that located at the boundary between the volcanic and the lacustrine deposits has also thin sediments.

For the estimated Vs profiles in Line 2, we can observed a thin sediment at S1 and L15 that located on the volcanic deposit in the northwestern part of the basin. Then, the sediments become thicker in the central (L2 and S5) and the southern (L12 and S6) parts of the basin.

In the north-south Lines of 3 to 5 in the central to the eastern parts of the basin, the Vs profiles having the thickest sediments in each line are observed at L3, L4, and L7, indicating that lacustrine sedimentation is more dominant in the central and the eastern parts than the western part of the basin. We also observe the Vs profile at S9 has a similar feature to that of S4 located in the boundary between the volcanic and the lacustrine deposits. Even though S9 located on the lacustrine deposit, the Vs profile contains a thin sediment similarly with the sites located on the volcanic deposit.

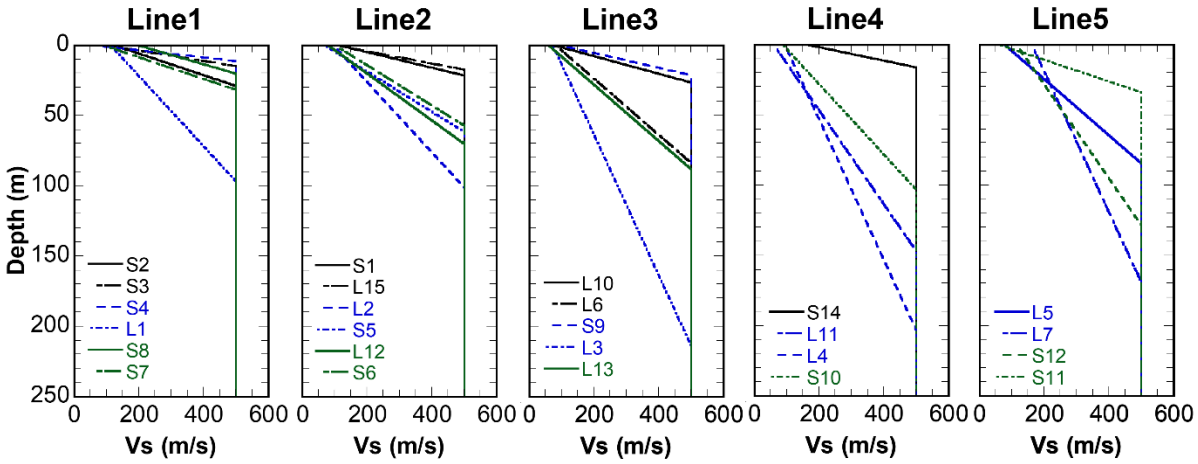

Figure 4.6 Distribution of estimated S-wave velocity profiles in Lines 1 to 5 from microtremor array measurements in the Bandung basin. Distribution of estimated S-wave velocity profiles in Lines 1 to 5 from microtremor array measurements in the Bandung basin. Lines 1 to 5 are located from the western to the eastern part of the basin as shown in Figure 4.1. Black, blue, and green lines correspond to location estimated profiles in the northern, the central, and the southern parts of the basin.

Chapter 5 Application of the proposed method for Vs profiles in Bandung basin

5.1 Objective

5.2 Locations of measurement sites

5.3 Implementation of V1-H/V measurements

5.3.1 Active seismic measurements for surface S-wave velocities

5.3.2 Observation of H/Vs from single-point microtremor measurements

5.4 Results of V1-H/V measurements

5.4.1 Observed surface S-wave velocities

5.4.2 Determination of velocity gradient from observed H/V peak frequencies

5.4.3 Estimated Vs profiles

5.5 Discussion

5.5.1 Comparison of profiles from phase velocities with the obtained ones from surface S-wave velocity and H/V

5.5.2 Effects of instruments reduction on estimation of V1

5.5.3 A guidance to apply the proposed method in other area

5.1 Objective

After confirmation of the profile representation using the linear function and the usage of 500 m/s for the bedrock velocity in the Bandung basin from the observed phase velocities, we applied the proposed method in the Bandung basin through the actual field measurements. We describe the actual field measurement to retrieve the observed V1 and H/V spectrum. Distribution of the observed V1s, the H/V spectra, and the estimated Vs profiles in the Bandung basin will be discussed. We also perform the comparison of the profiles estimated from the conventional and the proposed methods at five sites to evaluate the appropriateness of the estimated profiles using the proposed method.

5.2 Locations of measurement sites

The field measurements to observe V1s and H/Vs in the Bandung basin are conducted at 31 sites. The coordinates and locations of the measurement sites are displayed on the surface geological map of the basin in Figure 5.1 and listed in Table 5.1, respectively. Total 8 sites are located on the volcanic region in the northwestern part, while 23 sites are located on the lacustrine deposits in the western, the central, and the eastern parts of the basin. Since we have 5 sites (P3, P15, P19, P21, and P30) that are located in the same microtremor array measurement sites, we can make a profile comparison for the estimated Vs profiles from the two types of data.

Table 5.1 List of site names, coordinates, observed H/V peak frequencies and its standard deviation (stdev), observed V1s, estimated gradients, and Vs30s from V1-H/V measurements.

Site	Long (Deg)	Lat (Deg)	Surf. Geol. *	H/V peak freq. (Hz)	H/V peak freq. stdev. (Hz)	% of H/V peak freq. stdev.	V1 (m/s)	Gradi-ent (1/sec)	Vs30 (m/s)	Fund. peak freq. (Hz)	Ampl. factor of fund. peak	Avg. ampl. (0.4-10 Hz)	Dist. (m) **
P1	107.6194	-6.8693	OV	3.2	0.2	6	110	10.0	228	2.7	5.5	3.5	-
P2	107.6166	-6.9079	VD	1.2	0.2	15	200	4.0	255	1.8	3.9	3.1	-
P3 (S3)	107.5692	-6.9244	VD	7	1.1	15	140	21.0	347	6.8	4.8	2.8	42
P4	107.5641	-6.9058	VD	10	0.3	3	120	27.0	354	7.8	5.3	2.8	-
P5	107.6083	-6.9527	VD	Not clear	X	X	80	-	-	-	-	-	-
P6	107.6209	-6.9445	VD	6.5	0.6	9	130	19.0	326	5.7	5.1	2.9	-
P7	107.6439	-6.9522	LD	7	0.9	13	95	27.0	328	6.8	6.0	3.0	-
P8	107.6417	-6.9714	LD	4	0.45	11	125	12.0	266	3.5	5.2	3.2	-
P9	107.6529	-6.9880	LD	0.8	0.09	10	108	2.5	142	0.7	5.6	4.1	-
P10	107.6345	-7.0030	LD	0.9	0.04	5	81	4.0	132	0.9	6.5	4.5	-
P11	107.7075	-7.0232	LD	1.4	0.13	9	100	5.0	164	1.3	5.8	4.1	-
P12	107.7089	-7.0364	LD	5	0.3	7	84	21.0	285	5.0	6.4	3.3	-
P13	107.7554	-7.0322	LD	2.5	0.1	4	90	10.0	205	2.4	6.2	3.8	-
P14	107.7258	-7.0114	LD	0.7	0.07	10	100	2.5	134	0.6	5.8	4.2	-
P15 (L4)	107.7328	-7.0091	LD	0.7	0.08	12	70	3	109	0.6	7.0	4.8	3
P16	107.7741	-7.0058	LD	0.5	0.03	7	70	2.5	103	0.5	7.0	4.7	-
P17	107.7922	-7.0338	LD	10	1.3	13	158	32.0	402	11.4	4.5	2.4	-
P18	107.7304	-7.0464	LD	2.8	0.2	7	100	10.0	216	2.6	5.8	3.7	-
P19 (S9)	107.6643	-6.9529	LD	8	0.4	5	120	22.0	332	6.3	5.3	2.9	40
P20	107.6929	-6.9631	LD	0.6	0.06	10	100	2.0	128	0.5	5.8	4.1	-
P21 (L6)	107.6854	-6.9304	LD	0.9	0.1	12	105	3.0	145	0.8	5.7	4.2	100
P22	107.7174	-6.9477	LD	0.8	0.07	8	110	2.5	144	0.7	5.5	4.1	-
P23	107.7547	-6.9561	LD	2	0.14	8	120	5.0	185	1.4	5.3	3.8	-
P24	107.5915	-6.8858	VD	5.5	0.5	10	115	15.0	281	4.2	5.4	3.2	-
P25	107.5981	-6.9851	LD	Not clear	X	X	92	-	-	-	-	-	-
P26	107.5890	-7.0001	LD	0.6	0.06	10	87	2.5	121	0.6	6.3	4.4	-
P27	107.5906	-7.0394	LD	1.3	0.15	13	83	6.0	156	1.4	6.4	4.3	-
P28	107.5669	-7.0159	LD	1.3	0.2	14	150	5.0	216	1.7	4.7	3.4	-
P29	107.5343	-6.9734	LD	5	0.28	5	100	18.0	286	4.6	5.8	3.2	-
P30 (L15)	107.6097	-6.8898	OV	7	0.8	11	150	20.0	352	6.8	4.7	2.7	5
P31	107.7272	-6.9707	LD	0.5	0.02	3	70	2.5	103	0.5	7.0	4.7	-

*Surface geology: LD: Lake deposit, VD: Volcanic deposit, OV: Old volcanic product, YV: Young volcanic product

**Distance of measurement points between array and V1-H/V surveys

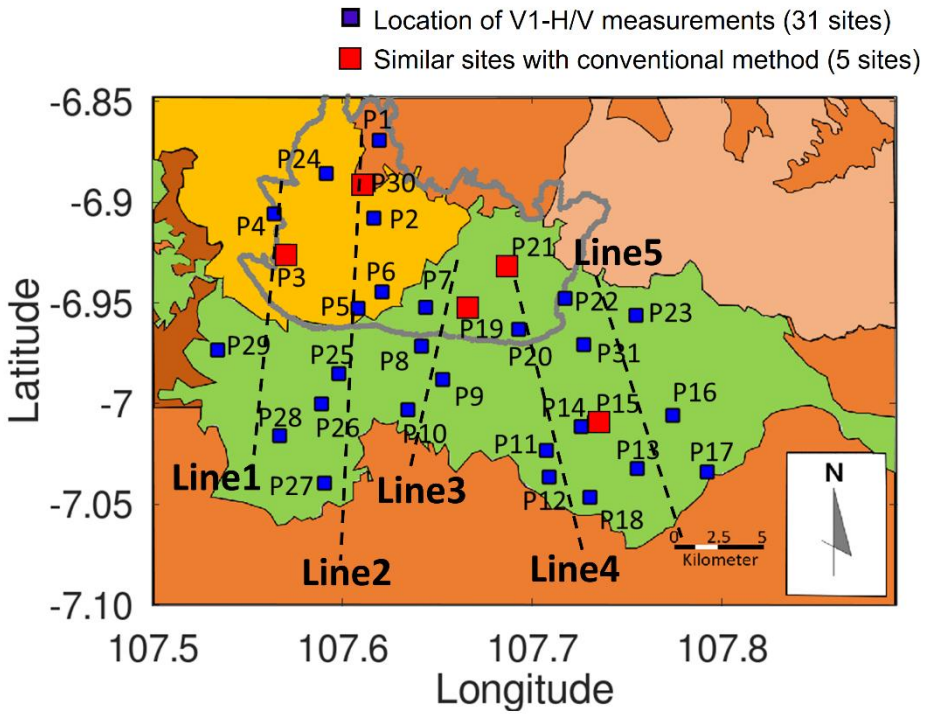

Figure 5.1 Location of the active seismic and single-point microtremor (V1-H/V) measurements on the surface geological map of the Bandung basin. Blue rectangles represent the measurement points. Red rectangles illustrate the similar measurement sites to the microtremor array survey. The legend for the surface geological map can be seen in Figure 1.3. Lines 1 – 5 correspond to cross-sections of estimated Vs profiles in Figure 5.8.

5.3 Implementation of V1-H/V measurements

5.3.1 Active seismic measurement for surface S-wave velocity

We utilized seven geophones that commonly available in Bandung to apply the seismic refraction survey. The geophones were arranged in a line array with 1 m spacing to implement an active seismic measurement for V1 at each site. The line array is expected to record seismic wave with wavelengths of 2 to 6 m to obtain high-frequencies phase velocities considering the active seismic measurement guidelines (e.g. Foti et al., 2018). A vertical impact source was generated using a sledgehammer at a distance of 5 m from the end of the line array to avoid the near-field effects. We recorded the waveforms with sampling of 2 kHz. The observed waveforms in the time-space *(t-x)* domain were transformed into a frequency-wavenumber spectrum *G(f,k)*,

using the frequency-wavenumber (*f-k*) transformation with the 2D Fourier transform (eq. 5.1) to observe the Rayleigh wave phase velocity.

$$G(f,k) = \int_{-\infty}^{+\infty} \int_{-\infty}^{+\infty} g(t,x) e^{-i2\pi(kx+ft)} dx dt \ldots (5.1)$$

where *g(t,x)* is the waveform records. A transformation of *G(f,k)* to frequency-phase velocity *(f-c)* domain is conducted by dividing the frequency with wavenumber. We then could identify the dispersive trend of observed Rayleigh wave phase velocity (i.e. a dispersion curve) from the high amplitude of an *f-c* spectrum. Finally, the V1 could be decided from the minimum value of the observed Rayleigh wave phase velocity.

5.3.2 Observation of H/V from single-point microtremor measurements

After conducting the active seismic measurement to obtain the V1, we also set a three-component sensor at a position close to the line array to perform the microtremors measurement. We recorded microtremors with a sampling rate of 100 Hz for duration of 10 to 15 minutes. We selected several stationary microtremors segments without transient noise with a length of 40.96 or 81.92 seconds to compute the H/V. We calculated the Fourier spectra of the three components at each segment using a Parzen window with a bandwidth of 0.1 Hz for their smoothing. The H/V was obtained by calculating the ratio of quadratic mean of the two horizontal spectra to the vertical spectrum. Finally, we averaged the H/Vs of all segments to obtain the final H/V. An example of instruments set up for actual V1-H/V measurement at P2 is shown in Figure 5.2. The total operation time of the active seismic and single point microtremor measurements at each site was generally about 30 to 35 minutes with two operators, which is one third of required time in the microtremor array measurement.

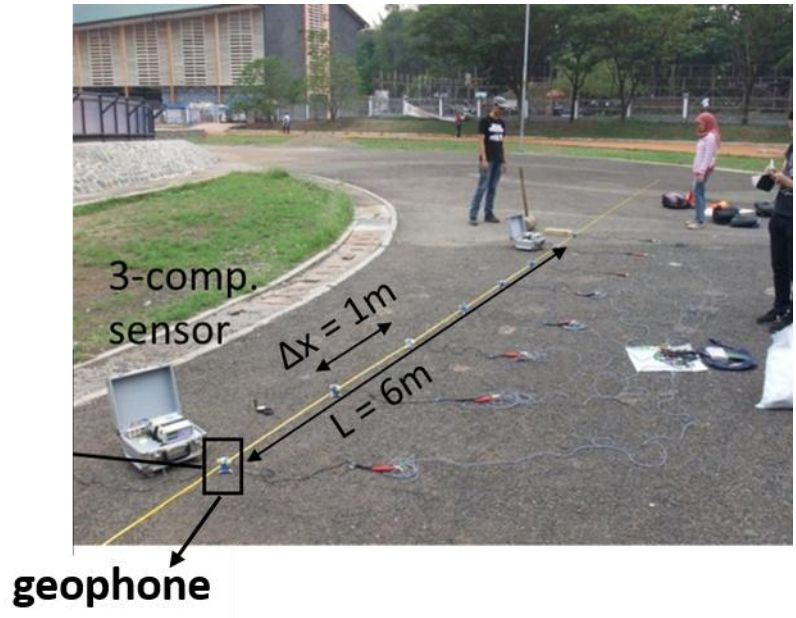

Figure 5.2 Configuration of instruments in short-length active seismic measurement (V1-H/V) consists of seven geophones and a single 3-component seismometer.

5.4 Results of V1-H/V measurements

5.4.1 Observed surface S-wave velocities

Examples of the recorded waveforms from an impact source and its corresponding *f-c* spectra are shown in Figure 5.3. These examples at P2, P8, and P19 sites are the representative phase velocity features from all of the observed *f-c* spectra in the basin to identify a V1. We pick the observed phase velocity from the maximum amplitude of the *f-c* spectra at each frequency as shown by gray circles. Moreover, the *f-c* spectra and the observed V1s for the other sites are shown in Figure 5.4.

At P2, high amplitude of the spectrum shows a clear fundamental mode of Rayleigh wave phase velocity at frequencies of 30 to 100 Hz. We obtained the V1 of 200 m/s from the observed minimum phase velocity at 100 Hz.

However at P8, an inversely dispervise trend of the observed phase velocity was identified in high amplitudes of the spectrum at frequencies higher than 17 Hz. This

trend indicates the domination of higher modes waves (Tokimatsu et al., 1992; Foti et al., 2018). We take the V1 from the minimum value of the observed phase velocity to consider only the fundamental mode of Rayleigh wave. The estimated V1 at P8 is 125 m/s at a frequency of 15 Hz. The inversely dispersive trends in the observed phase velocities also can be observed at P3, P6, P9, P10, P11, P20, P21, P25, P27, and P29.

Meanwhile at P19, we can see high amplitude parts of the spectrum at frequencies of 5 to 50 Hz that correspond to the fundamental mode of Rayleigh wave phase velocity. We also observed highest amplitudes of the spectrum at velocities of 400 to 500 m/s at frequencies of 70 to 90 Hz that corresponding to the higher modes Rayleigh wave phase velocity. To identify the V1 from a continuation of the fundamental mode of Rayleigh wave phase velocity at frequencies higher than 50 Hz, we pick the maximum amplitude of each frequency within a velocity range of 100 to 280 m/s indicated by black dashed lines. The fundamental mode of Rayleigh wave phase velocity is observed until a high-frequency end of 82 Hz. The phase velocity of 120 m/s at a frequency of 82 Hz is used as the V1 at P19. The similar procedure to identify V1 at P19 is also conducted at sites of P1, P4, P5, P6, P15, P26, P30, and P31.

We summarized the distribution of the observed V1s in the Bandung basin in Figure 5.5. We observed that the V1s are relatively low below 120 m/s in the lake deposit area in the central and the eastern parts of the basin except for P17 and P28 with V1s around 150 m/s. On the other hand, the estimated V1s in the volcanic deposit area in the northwestern part are higher than 120 m/s. The highest V1 is observed at P2 with a value of 200 m/s.

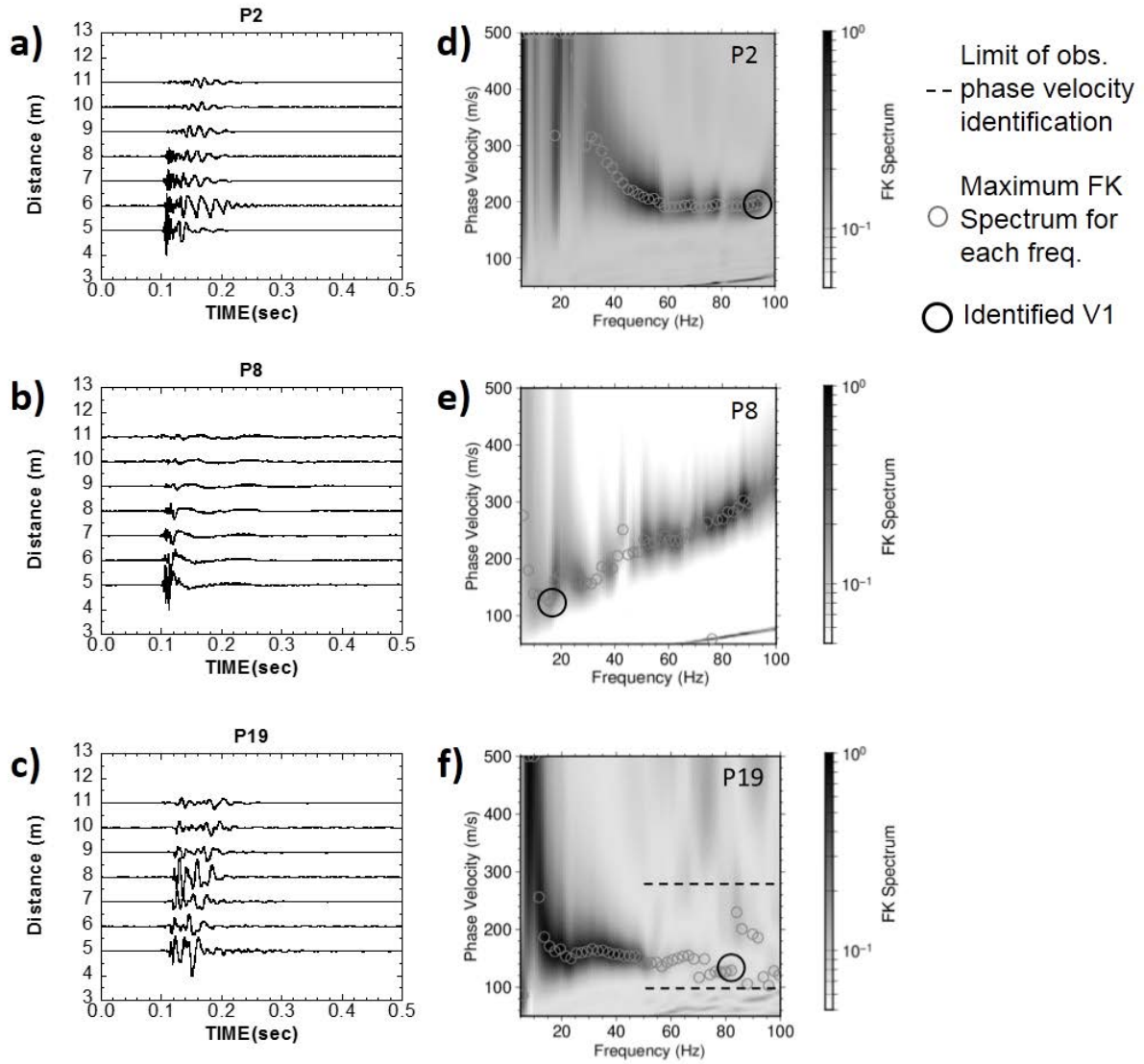

Figure 5.3 Examples of observed waveforms at a) P2, b) P8, and c) P19 and their corresponding observed phase velocities for estimation of V1 from a short-length active seismic measurement d) P2, e) P8, and f) P19

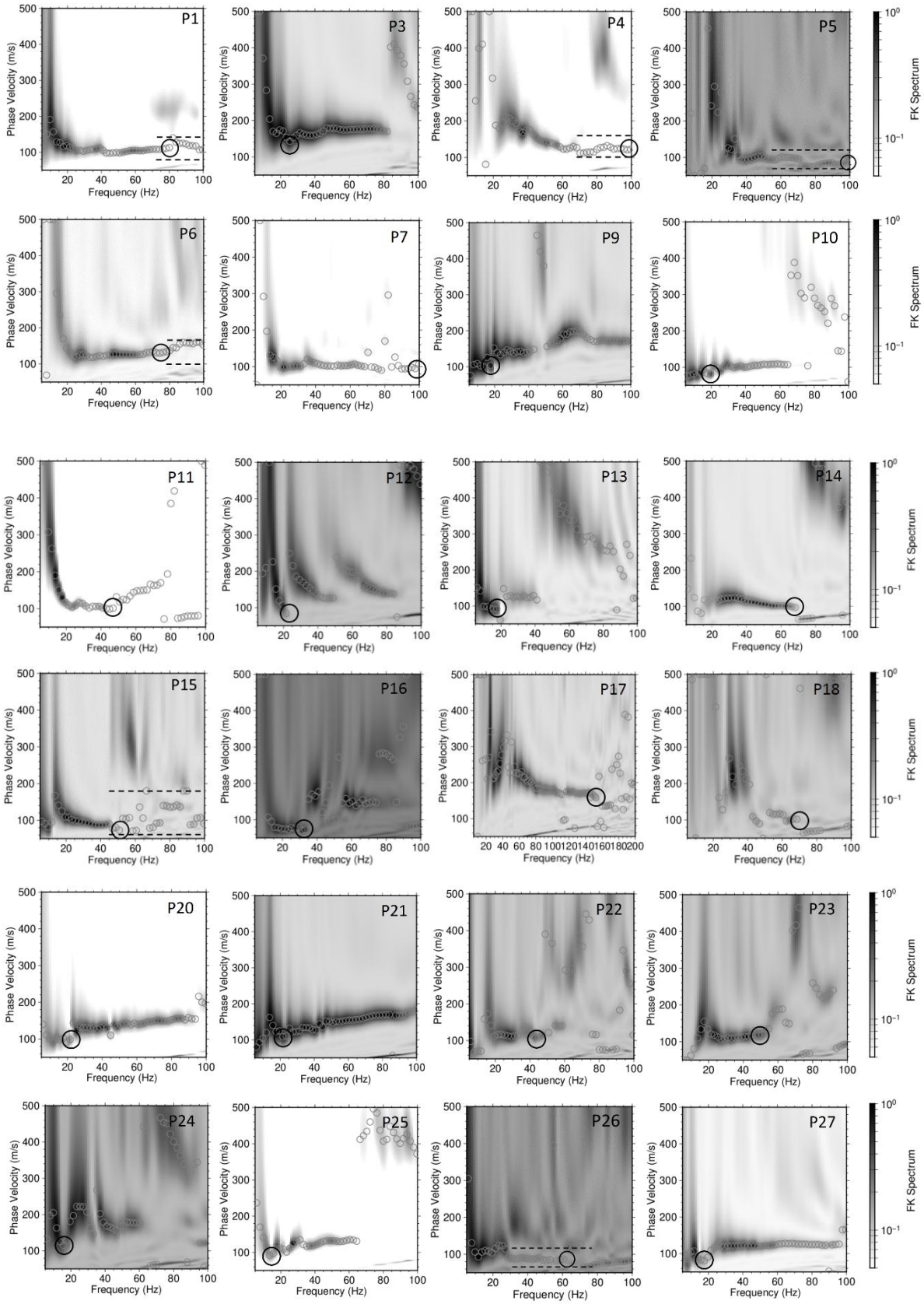

Figure 5.4 (continued)

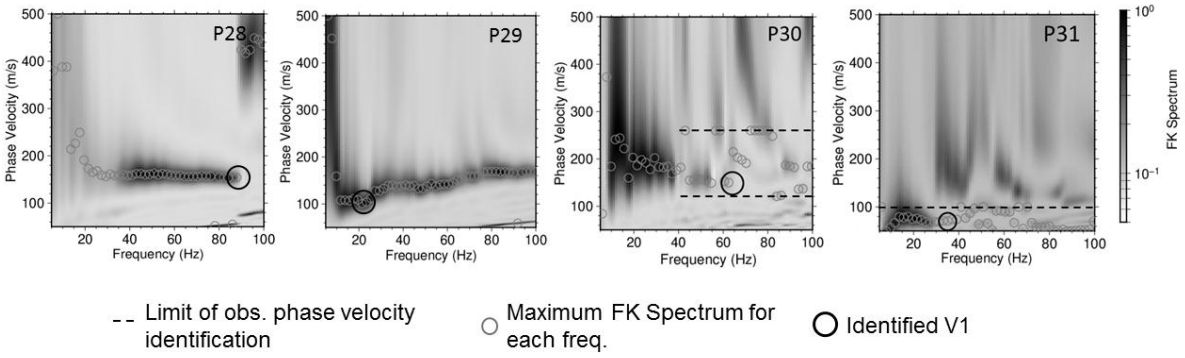

Figure 5.4 Observed frequency-phase velocity (f-c) spectra and observed Rayleigh wave phase velocities from the short-length active seismic measurements in the basin with the estimated V1s**.** Black dashed lines represent *f-c* spectrum area to pick the observed Rayleigh wave phase velocity. Gray circles correspond to the maximum *f-k* spectrum for each frequency to identify the observed Rayleigh wave phase velocity. Black circle indicates the observed V1. Amplitude of *f-k* spectra is illustrated in a grayscale.

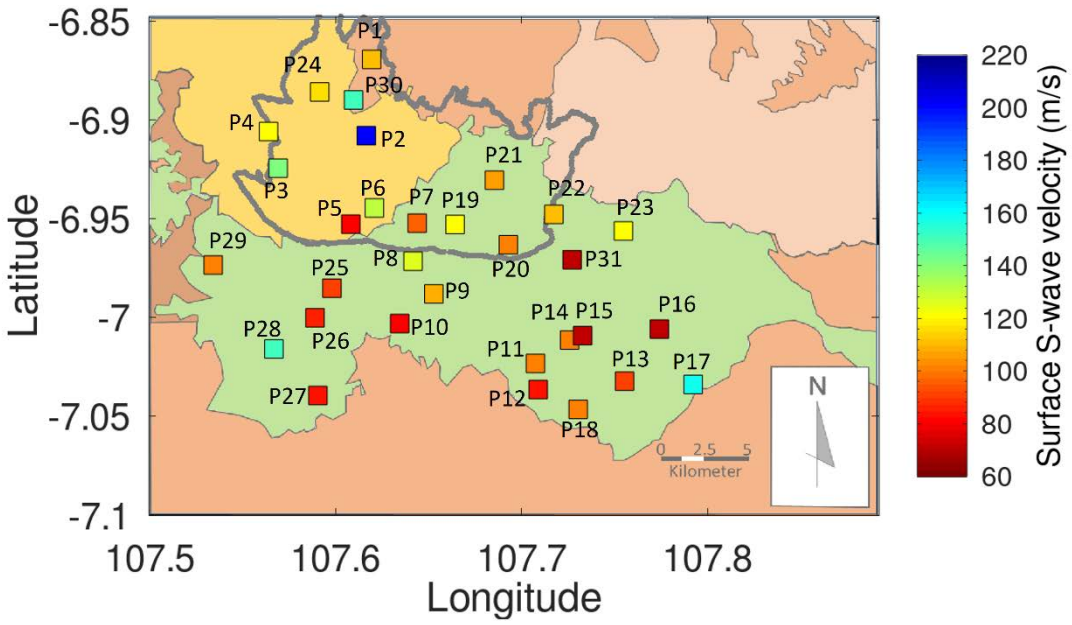

Figure 5.5 Distribution of observed surface S-wave velocities on the surface geological map of the Bandung basin. The legend for the geological map can be seen in Figure 1.3.

5.4.2 Determination of velocity gradients from observed H/V peak frequencies

The observed H/V spectra with their standard deviations from the single-point measurements are shown in Figure 5.6. Almost all the H/V spectra show the peak frequencies clearly, suggesting existences of high velocity contrast in the shallow part

between the layer of lacustrine sediment and the volcanic products bedrock. However, the observed H/V peaks are not prominent at P5 and P25, and we could not estimate the profiles at these two sites. We also observed in Table 5.1 that the percentages of standard deviations of peak frequencies of the observed H/Vs are mostly below 15% which is acceptable considering the result of the numerical test using various random noises. The distribution of the observed H/V peak frequencies in the basin is illustrated in the Figure 5.7a. The figure shows that the H/V peak frequencies at the sites in the volcanic deposit area and the basin edge are identified at frequencies higher than 5 Hz. Meanwhile, the sites situated on lake deposit in the central and the eastern parts of the basin have the H/V peak frequencies at lower than 2 Hz.

We use the peak frequencies of the observed H/V spectra and the measured V1s for determinations of the velocity gradients. The gradients are determined by searching the peak frequency of theoretical ellipticities that agree with the observed H/V ones. The measured V1 and a fixed bedrock velocity with 500 m/s were used in the calculation of the theoretical ellipticities. The theoretical ellipticities of the estimated profiles are illustrated by the dashed gray lines in Figure 5.6 and the distribution of the estimated gradient in the basin is illustrated in the Figure 5.7b. We observed that the distribution of the gradients in the basin is almost similar to the H/V peak frequency distribution. High gradient values more than 10.0 indicated by blue color are concentrated on the volcanic deposit area in the northwestern part and in the basin edge region, whereas the gradients with low values below 4.0 indicated by orange color are centralized on the lake deposit region especially in the central-eastern part.

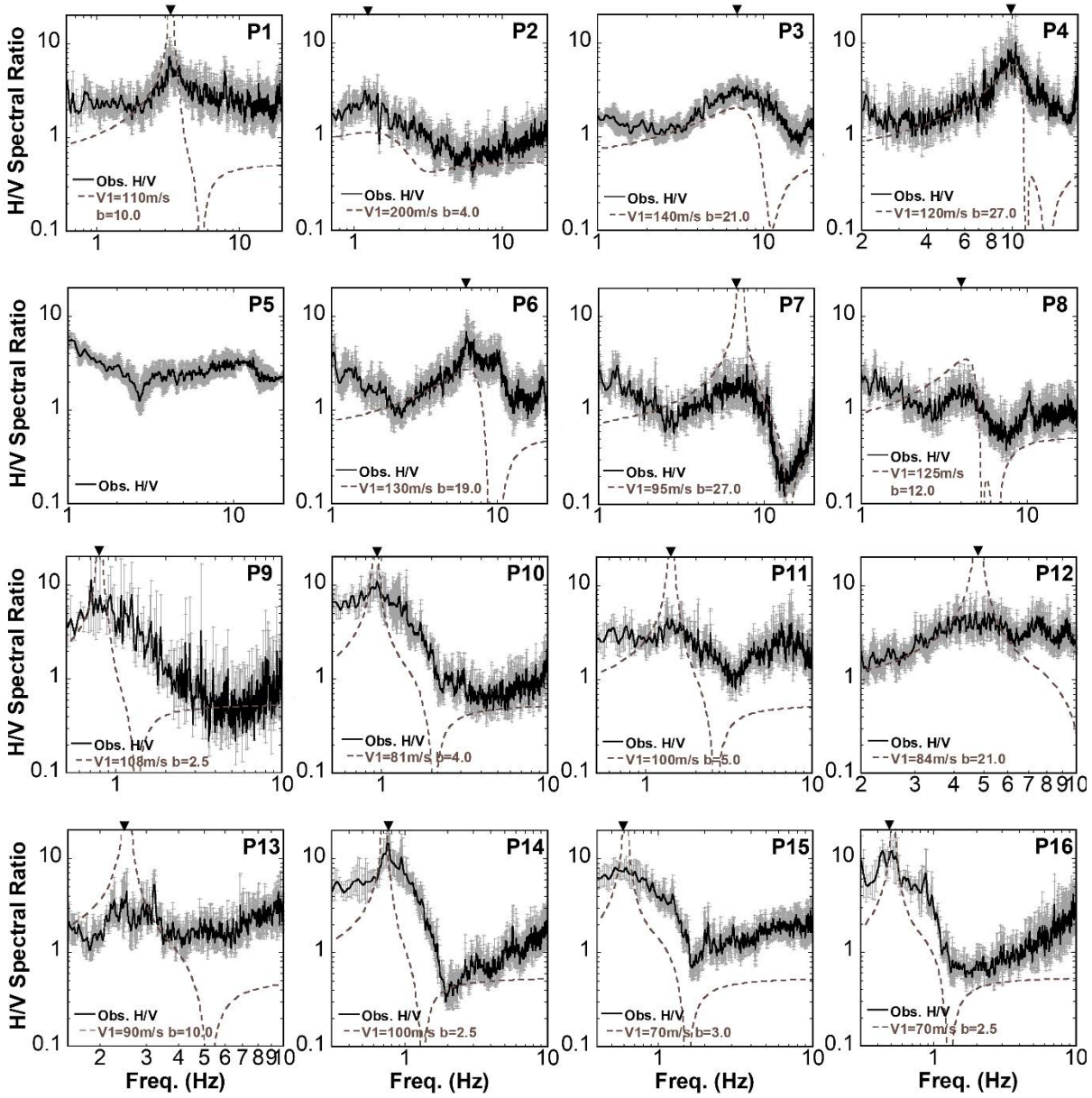

Figure 5.6 (continued)

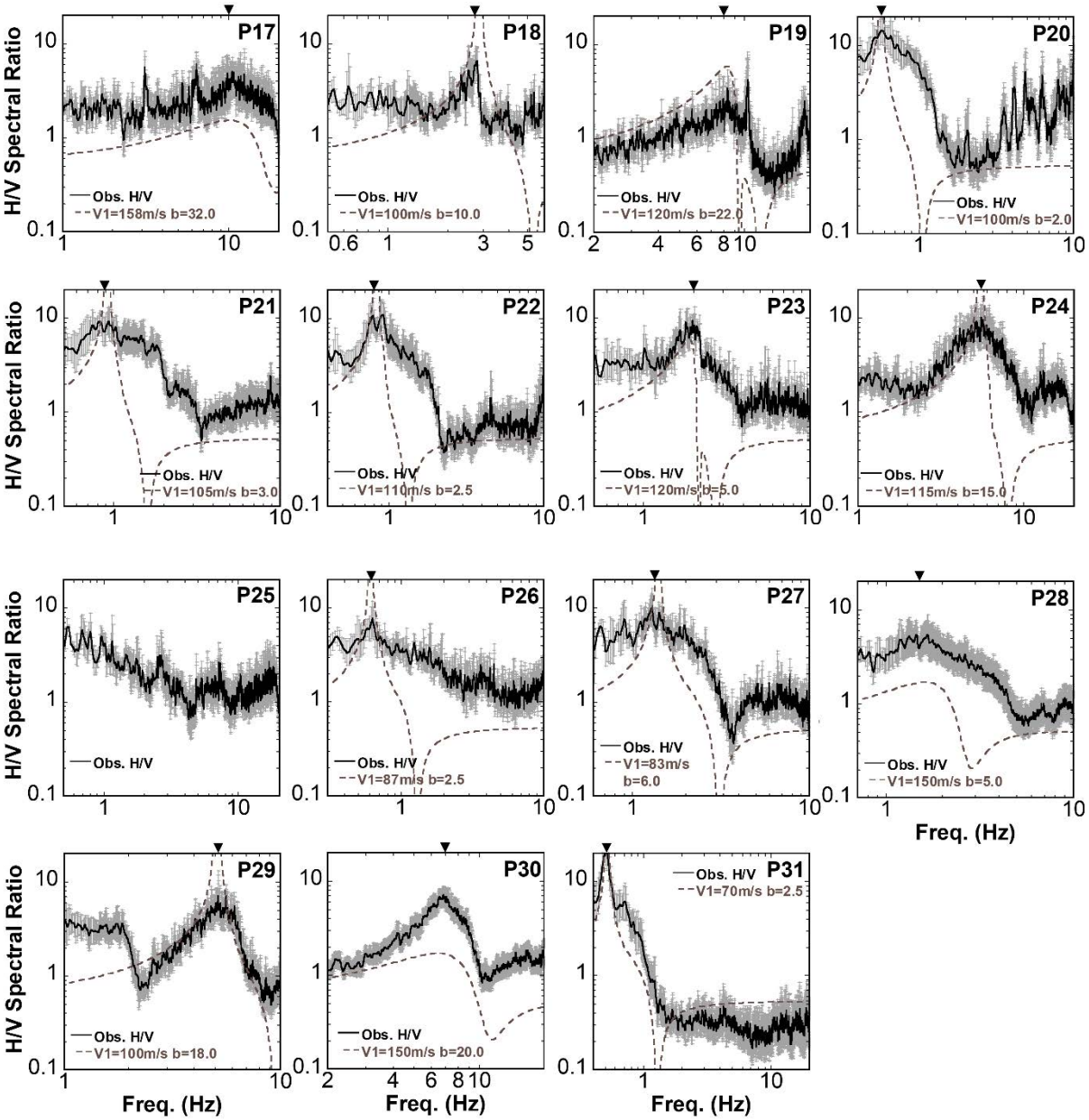

Figure 5.6 Observed H/V spectra from single-point microtremor measurements in the Bandung basin for determination of velocity gradient (b). Solid black and gray lines indicate observed H/Vs with their standard deviations. Gray dashed line represent theoretical fundamental mode Rayleigh wave ellipticity of estimated Vs profile using estimated V1 and *b*. Black reverse triangle indicates peak frequency of observed H/V. There are no *b* estimations at P5 and P25 since H/V peak frequencies are not prominently observed at those sites.

5.4.3 Estimated Vs profiles

The Vs profiles estimated at all the 29 sites are shown in Figure 5.8 along of five north-south oriented lines from the west to the east of the basin. The locations of the

lines can be seen in Figure 5.1. The stations located on the volcanic region (P4 and P3) and on the edge of the basin (P29) in Line 1 are characterized by thin sediments with high gradients above 15.0, while the profile on the lake deposit (P28) has relatively thick sediments with a lower gradient. Even though the Vs profiles on the volcanic region generally have high gradients above 10.0, we also observed small gradient of 4.0 at P2 in Line 2. Meanwhile, Vs profiles in the southern part of Line 2 on the lacustrine deposit have thick sediments at P26 and thin sediments at P27 in the edge of the basin. Moreover, the estimated Vs profiles in the central to the eastern part of the basin are shown in Lines 3, 4, and 5. In Line 3, the Vs profiles at P7, P19, and P8 located close to the volcanic deposit show thinner sediments than those of at P9 and P10 in the central part of the basin. We can also observe the gradation of sediment thickness from thick sediments at P21, P20, P14 in Line 4 and at P22, P31, P15, P16 in Line 5 to thin sediments at P11, P12, P18 in Line 4 and at P13, P17 in Line 5.

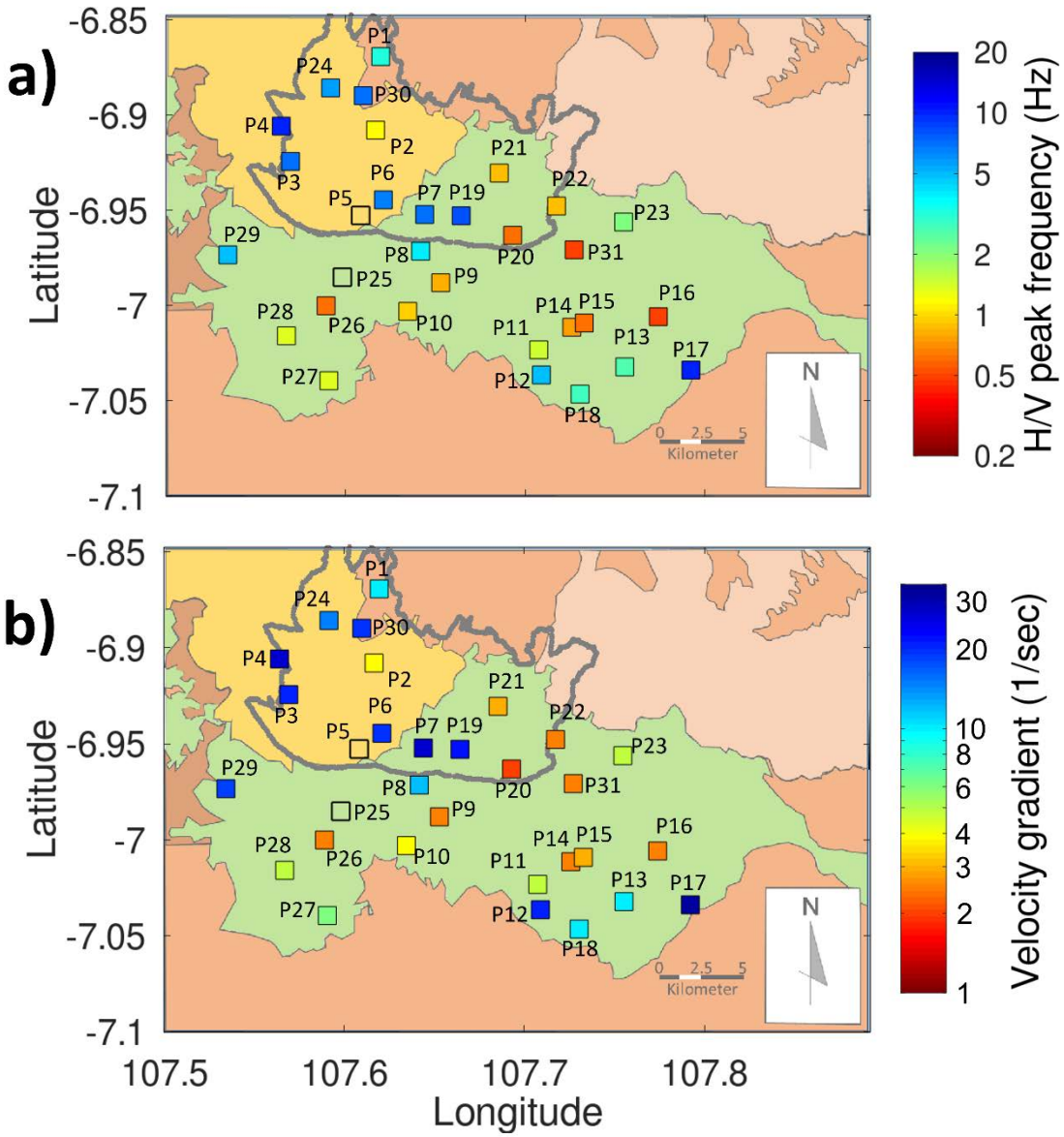

Figure 5.7 Distribution of a) observed H/V peak frequencies, and b) estimated velocity gradients on the surface geological map of the Bandung basin. The values of H/V peak frequencies and velocity gradients are represented by colorscale. The legend for the geological map can be seen in Figure 1.3.

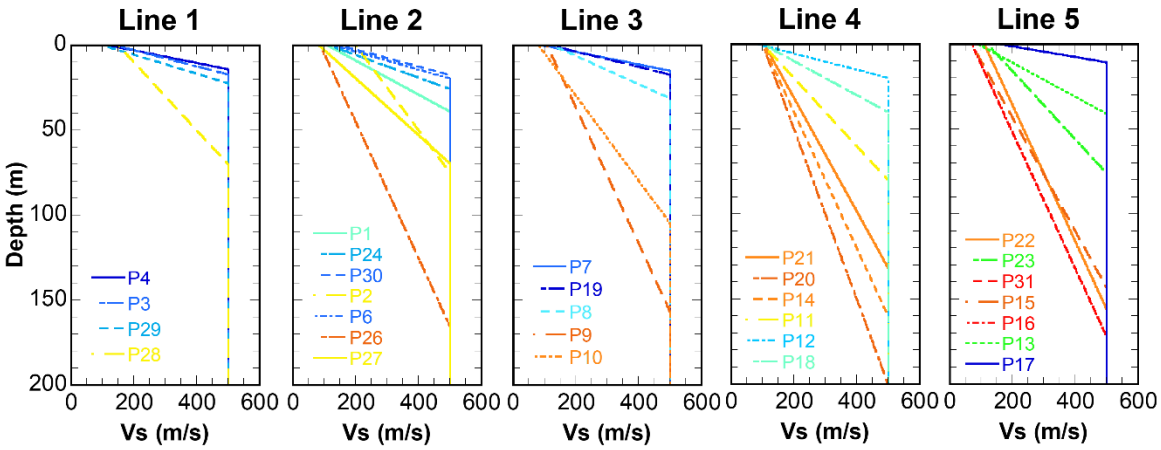

Figure 5.8 Estimated Vs profiles in the Bandung basin from the V1-H/V measurements. Color of the estimated Vs profiles correspond to value of the observed H/V peak frequencies in Figure 5.7a. Location of each line is shown in Figure 5.1.

5.5 Discussion

5.5.1 Comparison of the estimated profiles from phase velocities with obtained ones from surface S-wave velocity-H/V

We compare the Vs profiles estimated from the observed phase velocities (the conventional method) and the obtained ones from the V1-H/V data (the proposed method) for confirmation of their similarity. We have eight microtremor array measurement sites (L4, L6, L9, L14, L15, S3, S9, and S13) are the same as the locations of the V1-H/V measurements. However, we cannot estimate Vs profiles at L9, L14, and S13 due to the non-dispersive feature of the observed phase velocities as explained in the section 4.3. Therefore, the Vs profile comparisons between the two measurements are available at the five sites as shown in Figure 5.9. We also show the phase velocity comparison at the sites in Figure 5.10.

The profile comparison at L4 shows the V1 estimated from the V1-H/V measurement is a slight lower than that from the array measurement. The difference in the V1s could be explained from the phase velocity comparison. We noted that the

maximum frequency of the observed phase velocities from the array measurement is limited at a frequency of 10 Hz with velocity of 100 m/s, whereas those from the active seismic measurement is limited until a frequency of 50 Hz with velocity of 70 m/s. Therefore, the V1 obtained from the active seismic measurement correspond to the velocities of L4‟s profile in shallower depths than those obtained from the array measurement. Moreover, we observe in the profile comparison that the velocities between the both profiles are almost similar at shallow depths of 0 to 50 m. Large discrepancy between the both profiles is only found at deeper parts below depths of 50 m due to accumulations of the slight difference of the gradients between the both profiles become larger by increasing of the depths. However, the phase velocity comparison at L4 shows that the both theoretical phase velocities are similar in the entire frequency range.

The V1 comparison at L6 shows that the V1 estimated from the active seismic measurement are slightly higher (105 m/s) than that from the observed phase velocity (82 m/s). However, the phase velocity comparison is similar because the estimated V1 from the active seismic measurement coincide with the observed phase velocity at the high-frequency end from the array measurement. The both estimated profiles have a similar velocity increases at shallow depths to 30 m. However, the large discrepancy is seen in the depths deeper than 30 m because of the gradient difference between the two estimated profiles. This discrepancy also can be observed in the theoretical phase velocity comparison at frequencies lower than 3 Hz.

We observed the common characteristics of the profile comparison at L15, S3, and S9 with the similar velocity increases. The V1s estimated from the array measurement are lower values than those from the active seismic measurement due to the lack of convergent values of the observed phase velocity from the array

measurement at the high-frequency ends. In the gradient comparisons, we observed the gradient estimated using the proposed method at L15 and S3 sites are lower than those obtained from the array measurement. Therefore, we still found agreements in the theoretical phase velocity comparisons of the two estimated profiles at frequencies of 10-15 Hz at L15 and at frequencies of 10-20 Hz at S3, even though the V1s from the active seismic measurements are higher than those from the array measurements.

However, we show that the gradient estimated from the V1-H/V measurement at S9 has a slight higher value (22.0) than that from the array measurement (19.0). In the phase velocity comparison at S9, the theoretical phase velocity of the estimated Vs profile using the proposed method has a higher phase velocity than the theoretical one using the array measurement in the entire range of frequencies. We also notice a discrepancy of the phase velocities observed from the array measurement (circles) and from the active seismic survey (triangles) at frequencies of 25 to 28 Hz. The phase velocity from the active seismic survey has a higher velocity of 160 m/s than the phase velocity from the microtremor array measurement with velocity of 120 m/s. The discrepancy in the phase velocity comparison indicates the difference of the shallow part of the profiles estimated from the two types of measurement. We realize that the V1-H/V measurement point at S9 is located at a distance of a 40 m apart from the location of the site in the previous array survey, because of new construction around the array measurement point as shown in Figure 5.11. The difference of the measurement points may explain the difference in the shallow part of the profiles obtained from the two types of the measurements.

We can evaluate the agreement of the estimated Vs profiles from the proposed method by calculating the R values. We observed that all of the sites having R-values below 20% indicating the good agreement of the Vs profiles using the proposed

method. This also consistence with the results in the numerical test suggesting a similarity of the profiles estimated with the conventional method (phase velocity) and using the proposed method (V1-H/V). We also observe that the shallow Vs profiles estimated using the proposed method have a good accuracy because the shallow S-wave velocity at each site is constrained by the measured V1.

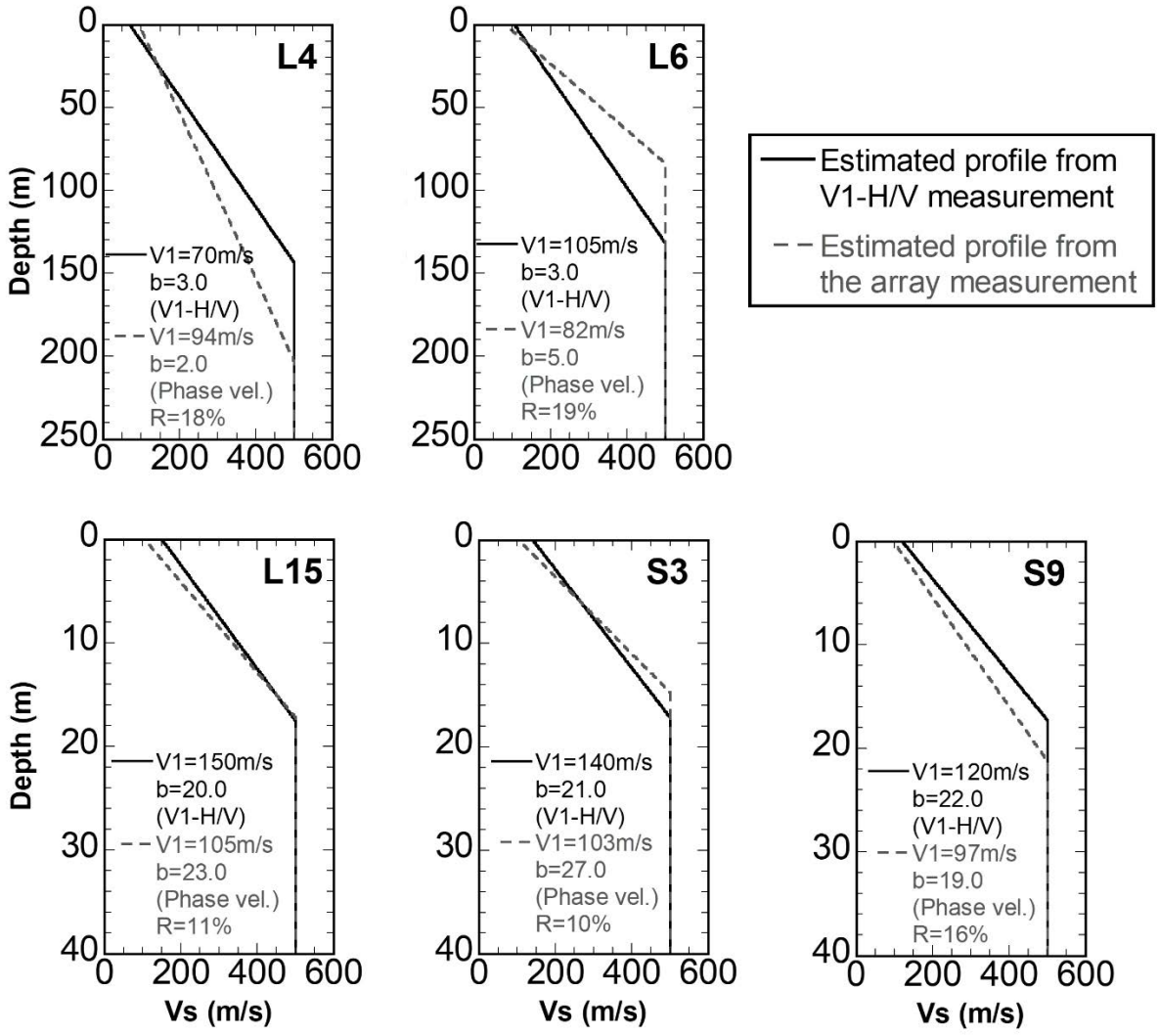

Figure 5.9 Comparison of estimated profiles using the proposed method (V1-H/V) and the conventional method (microtremor array measurements) at the five similar sites. Solid black and dashed gray lines correspond to estimated Vs profile from V1-H/V measurement and estimated Vs profile from microtremor array measurement, respectively. Estimated V1 and gradient are shown for each profile together with average relative difference or R-value between both of estimated profiles.

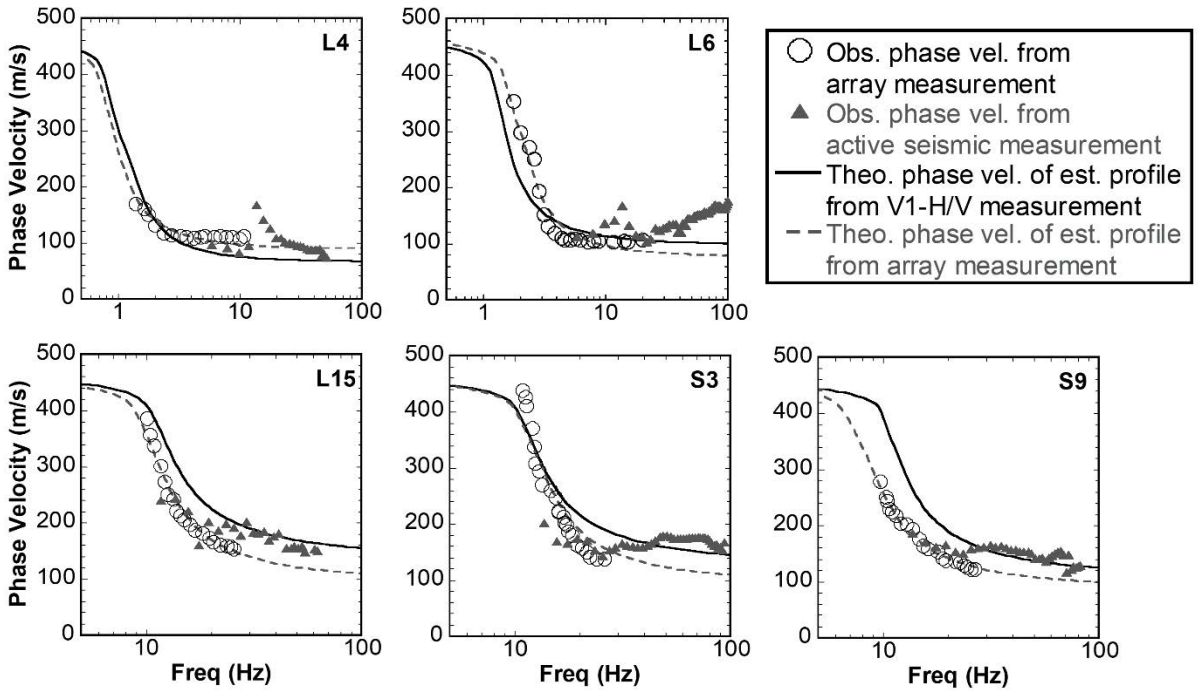

Figure 5.10 Comparison of phase velocity at the five similar sites. Circles and triangles correspond to observed phase velocities from the microtremor array measurement and the active seismic measurement, respectively. Solid black and dashed gray lines are theoretical phase velocities of the estimated profiles based on the observed V1-H/V and the observed phase velocity from the array measurement, respectively. *V1* and *b* of the estimated Vs profiles for the theoretical phase velocities are shown in Figure 5.9.

Figure 5.11 Location of the array and the V1-H/V measurement points at S9. The point of the V1-H/V measurement is move 40 m apart from the point of array measurement since a new construction has been built.

5.5.2 Effects of instruments reduction on estimation of V1

The aim of the proposed method is to provide an S-wave velocity easily with less number and cheap instruments required. Thus far, we use seven geophones in the active seismic measurement to obtain the V1. Therefore, we further investigate a possibility to reduce the number of geophones in estimating the V1. We analyzed the F-K spectrum obtained by using number of geophones less than 7. The investigation is conducted at P2, P14, and P28 sites where the V1s are easily recognized from the phase velocity at high-end frequency. We also consider these sites for the investigation due to the observed dispersion curves are dominated by the fundamental mode of Rayleigh wave as shown in Figure 5.4.

Figure 5.12 shows several F-K spectra estimated based on the number of geophones used. For the F-K spectra obtained by using less than 7 geophones, we involved the waveforms recorded at the nearest geophones from the source to keep a distance of the source and the first geophone with length of 5 m. We should notice that a high amplitude of the F-K spectrum at each frequency indicate a high correlation of the phases in the involved waveforms. Therefore, a high amplitude of F-K spectrum can be used as indicator for the reliable observed phase velocity at a frequency.

Based on the high amplitude of F-K spectrum, we can identify the Rayleigh wave phase velocity of the fundamental mode in each F-K spectrum for estimation of V1. The identified phase velocities for each F-K spectrum are varied in the frequency range and the velocity. For example, the fundamental mode of the Rayleigh wave phase velocity using 3 geophones at P2 is observed from the lowest frequency of 45 Hz, with velocity of 240 m/s to the high-end frequency of 68 Hz with velocity of 160 m/s as the estimated V1, whereas the fundamental mode of Rayleigh wave phase velocity estimated from 7

geophones having the lowest frequency at 30 Hz with velocity of 320 m/s to the high-end frequency at 94 Hz with velocity of 200 m/s as the estimated V1. The difference in the lowest frequency of the observed phase velocity is due to the longer wavelength can be covered by longer array using 7 geophones than that using by the 3 geophones, while variation of the V1 is due to lateral heterogeneity of the shallow subsurface condition at the first 3 geophones and the farther geophones. Figure 5.13 show a confirmation of lateral heterogeneity at P2 by estimating the F-K spectrum using the 3 farthest geophones to the source. We observed the phase velocity of 210 m/s at 68 Hz which is higher than the one obtained by involving 3 geophones close to the source with velocity of 160 m/s. On the other hand, the result at P14 indicate a less lateral heterogeneity in the shallow subsurface than at P2. We obtained that the estimated V1 using 3 geophones has velocity with 90 m/s which is lower than the V1 obtained by using 7 geophones with velocity of 100 m/s. Moreover, the V1s using 4, 5, 6 of geophones have a similar V1 to the 7 geophones around 100 m/s.

We summarized the variation of estimated V1s considering the number of geophones at P2, P14, and P28 in Figure 5.14. Even though the estimated V1 with 3 geophones may deviate 20% to that obtained by using 7 geophones due to the lateral heterogeneity of the shallow subsurface condition along the line array, the results indicate the appropriateness of the estimated V1 from 3 geophones. Therefore, we can reduce the measurement effort to apply the proposed method by utilizing 3 geophones for the estimation of V1.

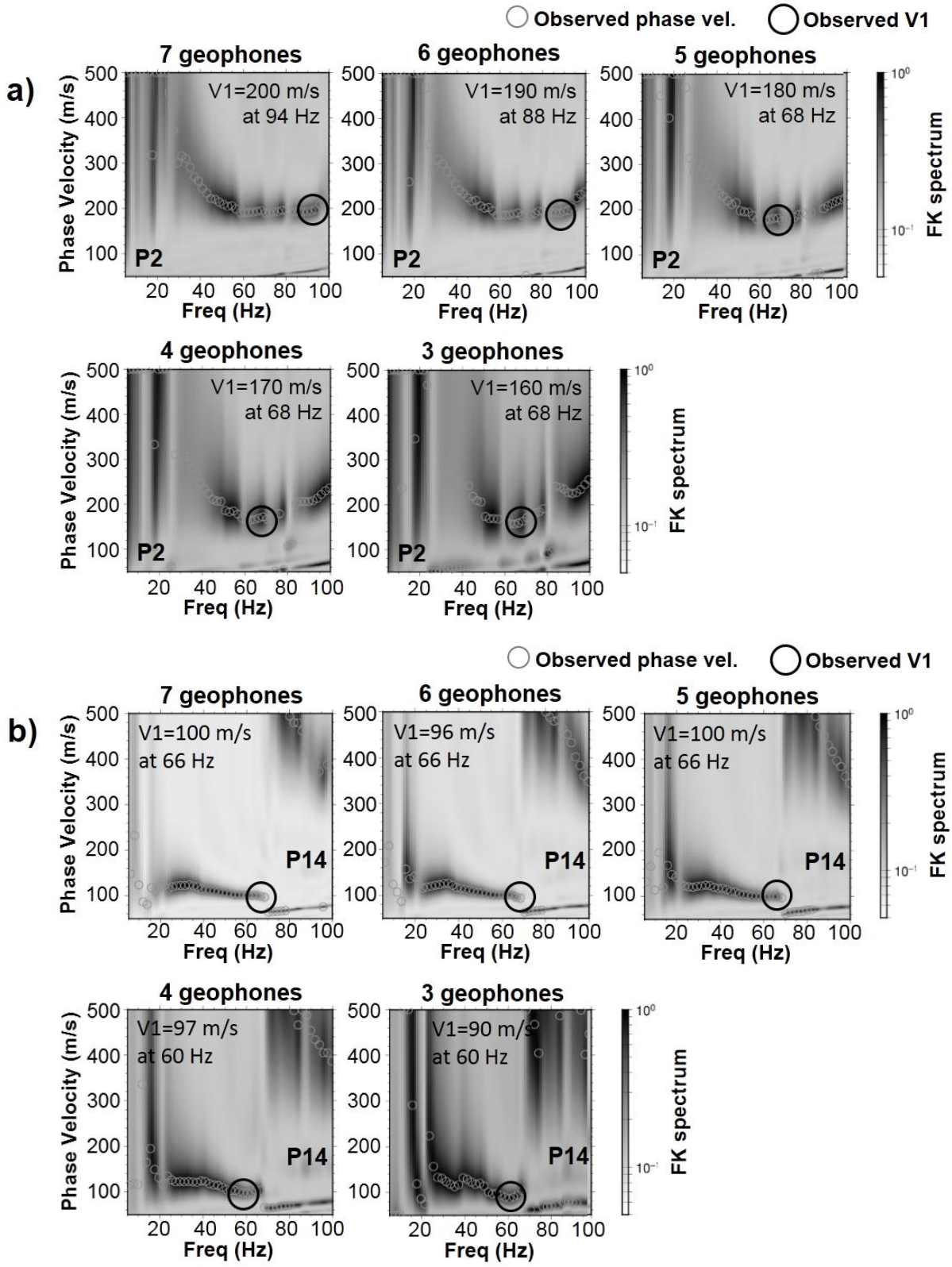

Figure 5.12 (continued)

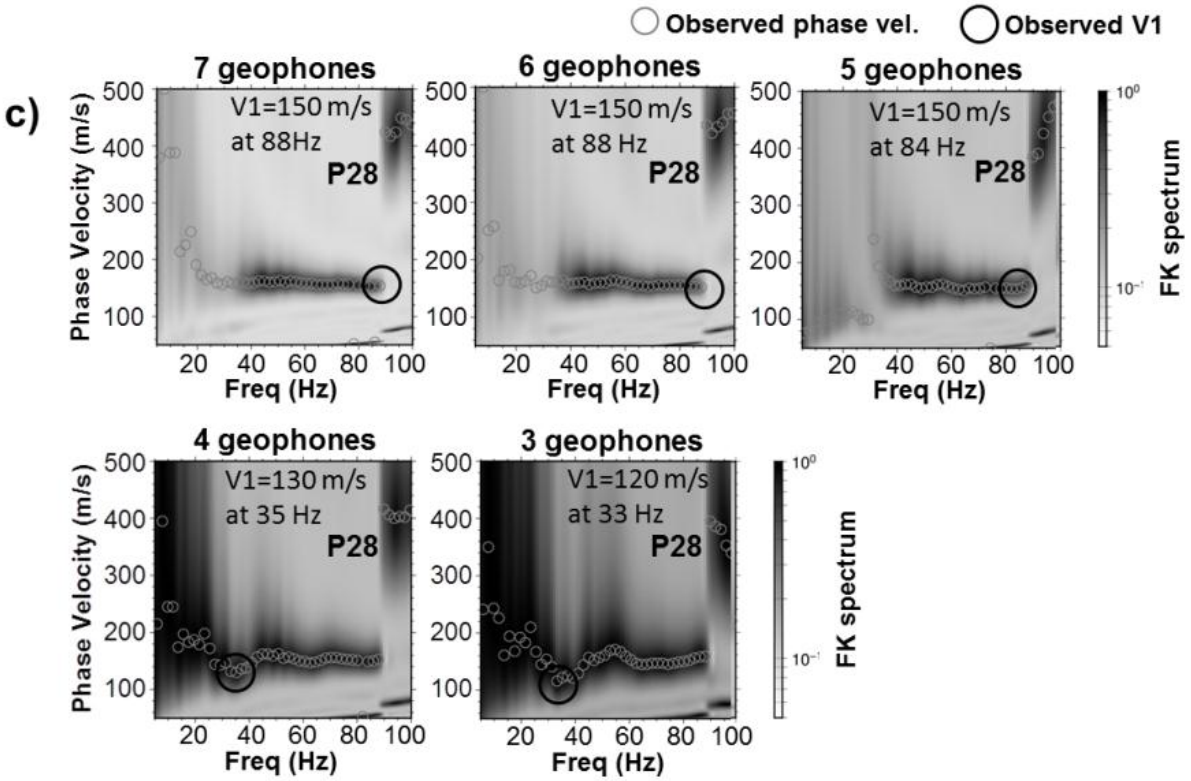

Figure 5.12 Estimated F-K spectra from the recorded waveforms using various number of geophones at **a)** P2, **b)** P14, and **c)** P28 sites. Grayscale color indicates the amplitude of F-K spectrum. Gray and black circles indicate the observed phase velocity and the estimated V1, respectively.

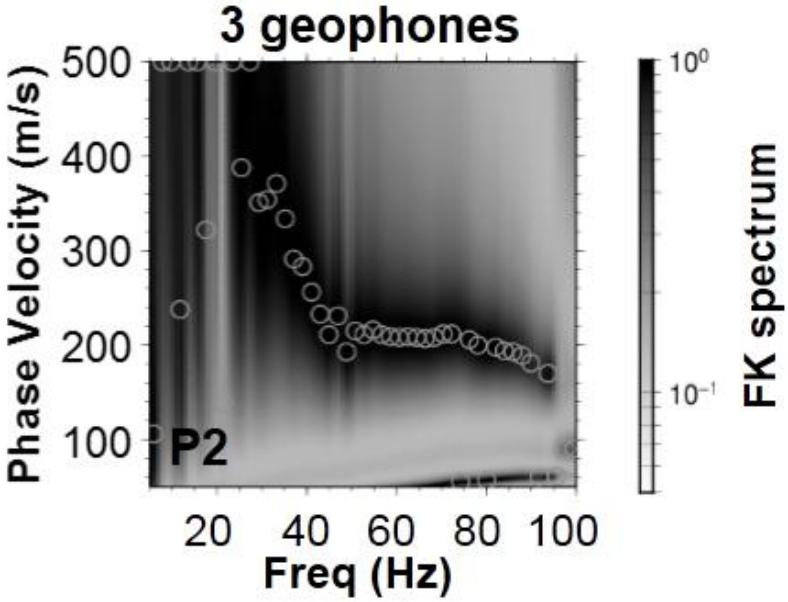

Figure 5.13 F-K spectrum at P2 estimated by using the 3 farthest geophones to the source. Grayscale color indicate the amplitude of F-K spectrum. Gray circles indicate the observed phase velocity based on highest amplitude of F-K spectrum at each frequency.

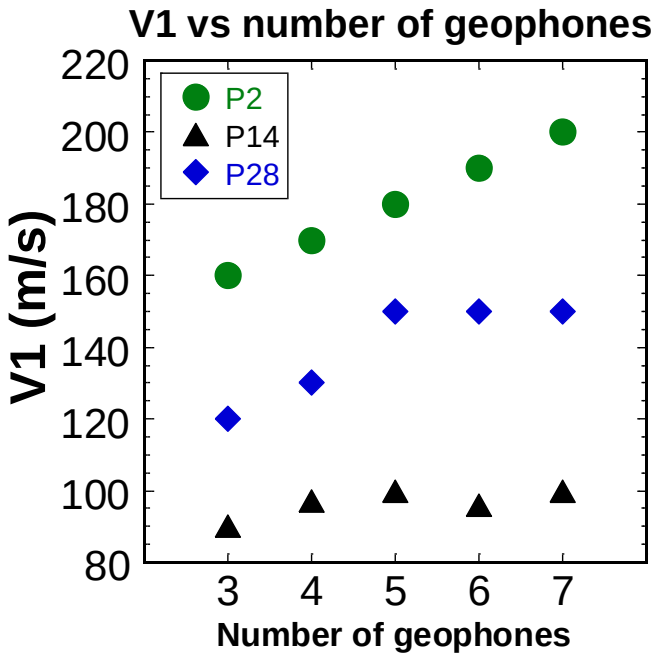

Figure 5.14 Variation of estimated V1 based on the number of geophones. Green, black, and blue marks indicate the estimated V1 based on the number of geophones at P2, P14, P28, respectively.

5.5.3 A guidance to apply the proposed method in other area

We observed that the estimated Vs profiles from the proposed method in the Bandung basin are appropriate because the observed phase velocities from the array measurements can be well approximated using the linear model representation. These results indicate an important of available a priori information such as observed phase velocities in a wide frequency range or borehole (P-S logging) data at representative sites in an investigated area to confirm the appropriateness of the profile representation with the linear function before further application of the proposed method. However, we should consider several cases of the observed phase velocities in an investigated area for confirming the appropriateness of the linear function for the profile representation. The proposed method can be applied if most of the observed phase velocities are sufficiently satisfied by the linear profile representation. Moreover, we may adjust the profile

representation using other functions such as the power-law function or the exponential function if most of the observed phase velocities cannot be satisfied by the linear profile representation. Furthermore, if an investigated area contains several observed phase velocities that can be represented by the linear function and by another function, we should identify the boundary of the region that can be represented by the linear function or another function, such as the dependency of function types with surface geological conditions. If the boundary is difficult to identify, the investigated area is categorized as the difficult case to apply the proposed method.

We should notice the simplicity of the profile representation that only consists of a single gradient in the proposed method. Therefore, we have difficulty to estimate a bedrock depth. We should also consider several difficult cases to apply the proposed method that have been described in the section 3.6 of numerical tests.

Chapter 6 Site characterization in Bandung basin

6.1 Objective

6.2 Comparsion of amplifications estimated from conventional and proposed methods

6.2.1 Vs30s

6.2.2 Site amplification factors

6.3 Distributions of Vs30 and site amplification factor proxies

6.4 Comparison with the previous PGA map

6.1 Objective

We further use the Vs profiles estimated from the conventional method and the proposed method for the characterization of site amplifications in the Bandung basin in this chapter. We first compare Vs30s and the site amplification factors of the Vs profiles estimated from the five same sites. We then discuss the distribution of the Vs30s, and the distributions of several site amplification proxies in the basin. In the last part of this chapter, we discuss a comparison of Vs30s and peak ground accelerations (PGAs) from the previous study and using our results.

6.2 Comparison of amplifications estimated from conventional and proposed methods

6.2.1 Vs30s

The time-averaged S-wave velocities in the top 30 m (Vs30) comparisons between the profiles estimated from the conventional method and the proposed method are listed in Table 6.1. The Vs30 is generally used as a site classification for engineering purposes, such as the National Earthquake Hazards Reduction Program (NEHRP) site classification (Building Seismic Safety Council, 2004). The Vs30 is also used as a proxy of the site effect in a strong-motion attenuation relationship such as in Boore et. al. (1993; 1997). The Vs30 is calculated by:

$$Vs30 = \frac{30}{TT_{(0-30)}} = \frac{30}{\left(\sum_{i=1}^{n} \frac{d_i}{Vs_i}\right)} \quad \ldots (6.1),$$

where TT(0-30) is the travel time from the surface to a depth of 30 m. d_i, Vs_i, and n are the thickness of the i-th layer, the S-wave velocity of the i-th layer, and the total number of layers to a depth of 30 m.

We observe that the Vs30s of the profiles estimated from the proposed method have differences less than 10% to those of the Vs profiles from the conventional method indicating an appropriateness of the Vs30s estimated using the proposed method.

Table 6.1 Comparison of the Vs30s of the Vs profiles estimated using the conventional microtremor array surveys and those estimated by the proposed method.

Site	Vs30 of the Vs profile from the conventional method (m/s)	Vs30 of the estimated Vs profile from the proposed method (m/s)
L4	122	109
L6	144	145
L15	321	352
S3	337	347
S9	289	332

6.2.2 Site amplification factors

We also compare the calculated 1D site amplification factors for the Vs profiles estimated from the conventional method and the proposed method in Figure 6.1. Here the site amplification factors are calculated as the 1D reverberation of vertical incident SH-wave in a layered-model (Kramer, 1996). The amplification factor is defined as a ratio of wave amplitudes on the surface to that of the incident waves in the bottom layer. Therefore, the amplification factor becomes two at low frequency due to the free stress condition on the surface. Since Q-values for the Vs profiles are not determined in this study, we assume that Q-value of each layer is equal to one-fifth of its S-wave velocity in meter per second.

In the site amplification factor comparison in Figure 6.1, we observe that the fundamental peak frequencies of the site amplifications for both profiles are similar because the estimated Vs profiles using the proposed method are derived from the agreement with the observed H/V peak frequencies. Moreover, we also note similar fundamental peak amplitudes in the site amplification comparison. This similarity is

caused by the fact that the estimated Vs profiles from the proposed method and the conventional method have similar velocity contrasts between the bedrock and the top S-wave velocity that control the peak amplitudes of the site amplification factors (Stambouli et al., 2017; Trifunac, 1990). Since the V1 and the bedrock velocity are provided in the proposed method, our Vs profile can well anticipate the peak amplitude of the amplification. We also confirm the similarity of the averaged site amplification factors for the both profiles in a frequency range of 0.4 to 10 Hz as shown in Table 6.2. The frequency range that we considered in the calculation of the averaged site amplification factor is decided from the calculation of the spectrum intensity (Hudson & Housner, 1958). The differences of averaged site amplifications for both profiles are around 10%.

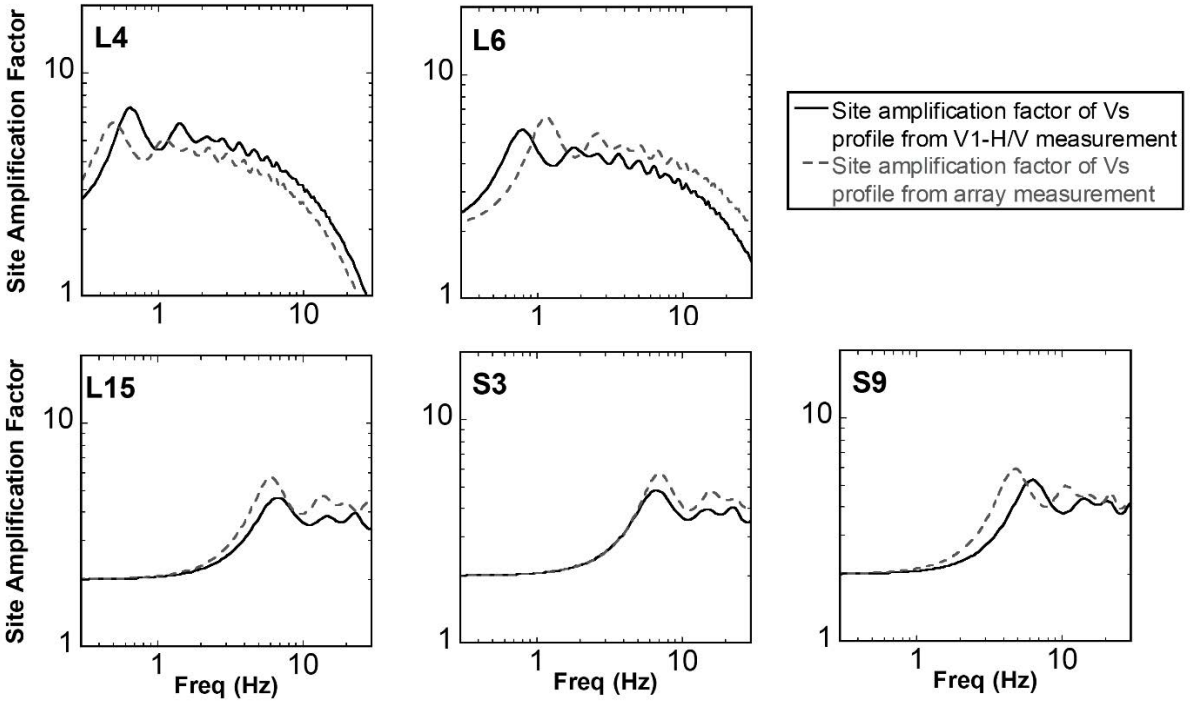

Figure 6.1 Site amplification comparison of estimated profiles from the microtremor array and the V1-H/V measurements at the five similar sites. V1 and b of the estimated Vs profiles for calculation of the site amplification factors are shown in Figure 5.9.

Table 6.2 Comparison of the averaged site amplification factor in a frequency range of 0.4 to 10 Hz of the Vs profiles estimated from the conventional method with those estimated from the proposed method.

Site	Averaged site amplification factor (0.4-10 Hz) from the conventional method	Averaged site amplification factor (0.4-10 Hz) from the proposed method
L4	4.2	4.8
L6	4.4	4.2
L15	3.0	2.7
S3	2.9	2.8
S9	3.2	2.9

6.3 Distributions of Vs30 and site amplification factor proxies

We here discuss the distributions of the Vs30s and the site amplification proxies in the basin. Figure 6.2 illustrates the distributions of the Vs30s, the fundamental peak‟s frequencies, the fundamental peak‟s amplitudes, and the averaged site amplification factors in the basin. For the individual shape of the site amplification factors at each geological unit can be seen in Figure 6.3.

In the distribution of the Vs30s (Figure 6.2a), higher Vs30s of above 250 m/s are observed in the northern part and in the edge of the basin of the southwestern (S8) and the northeastern parts (S14). We also found various distribution of Vs30s in the lake deposit area. Vs30s with higher values of 150 to 200 m/s are observed in the central-western part, whereas Vs30s in the central-eastern part are less than 150 m/s. We also observed several sites in lake deposit part having high Vs30s with velocities of above 250 m/s in the border region in the central and the western parts. Moreover, a high Vs30 more than 300 m/s is observed at P17 in the south-eastern part. The high Vs30 sites located in the lake deposit part which is close to the volcanic region indicate that the profiles consist of a thin lake deposit layer over the bedrock layer. As summaries of the Vs30 distribution in the basin, we found the averaged Vs30 for each geological unit in

Table 6.3. The averaged Vs30s in areas covered with the lake deposit, volcanic deposit, old volcanic product and young volcanic product are 184 m/s, 298 m/s, 313 m/s, and 370 m/s, respectively. Considering the NEHRP site classification, the averaged Vs30s at lake deposit, volcanic deposit, and old volcanic product are categorized as “stiff soil”, while that at young volcanic product corresponds to “very dense soil and soft rock”.

The variation of the 1D site amplifications in the basin is represented by the distributions of the amplification proxies such as the fundamental peak frequency of the amplification, the fundamental peak amplitude, and the averaged amplification at frequencies of 0.4 to 10 Hz. The distributions of the fundamental peak frequencies and amplitudes can be shown in Figures 6.2b and 6.2c. We found low fundamental peak frequencies around 0.6 Hz and high peak amplification with factors around 7 in the north and central-eastern parts of the lake deposit area (P15, P16, P31, L3, and L11). We also found relatively large amplification factors of above 6 at the south-central part (L13 and P10), the central-western part (S4), and the south-western part (L12, S5, P26 and P27) in the lake deposit area because these sites have low V1s below 95 m/s. At the sites situated in the volcanic deposit region especially in the north-western part of the basin, the distribution of the fundamental peak amplifications are characterized by high fundamental peak frequencies from 2 to 8 Hz and amplification factors below 6 due to high V1s for the estimated profiles in this region.

The characteristics of the averaged site amplification in the basin (Figure 6.2d) are similar to that of the Vs30 features in the basin. We observed that the high amplification is occurred in the lake deposit area with averaged factors of above 4. Especially the averaged factors in the central-eastern part of the basin almost reach 5. The low averaged amplifications below 3.5 can be found in the volcanic deposit in the northwestern part and in the basin-edge region.

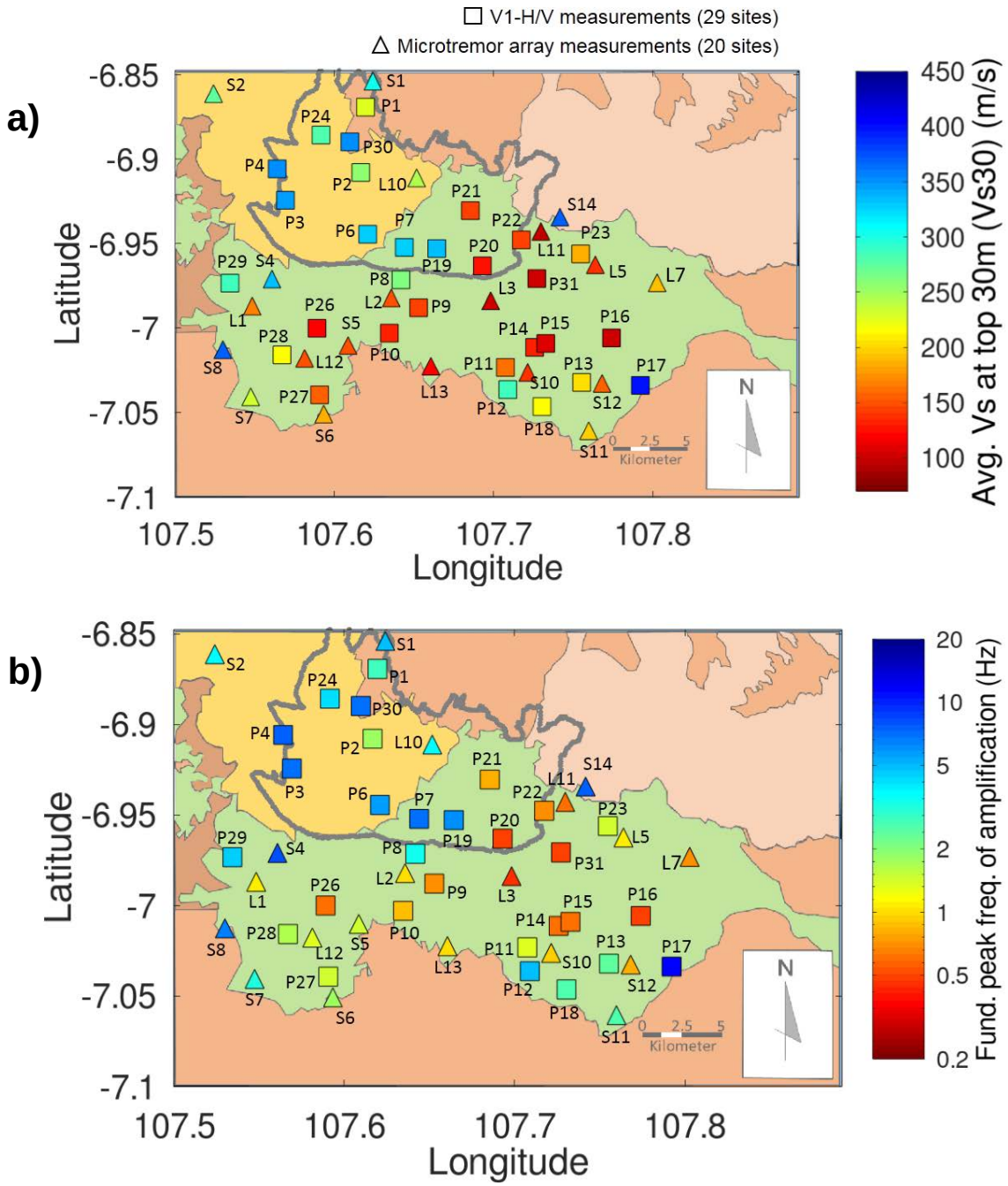

Figure 6.2 (continued)

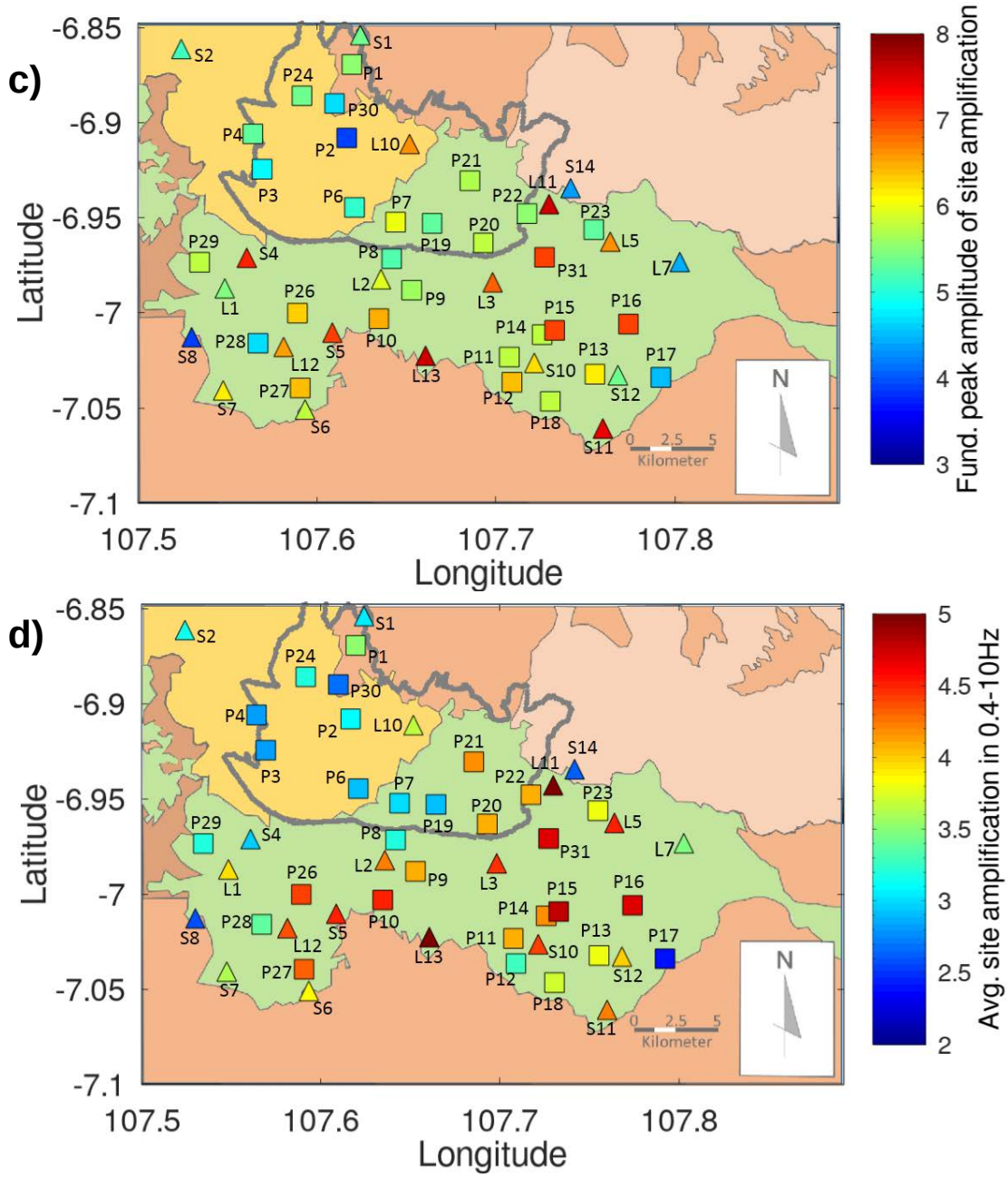

Figure 6.2 Distribution map of (a) Vs30, (b) Fundamental peak frequency of the site amplification factor, (c) Fundamental peak amplitude of the site amplification, and (d) Averaged site amplification factor in a frequency range of 0.4 to 10 Hz from all the measurement points in the Bandung basin. Legend of geological map can be seen in Figure 1.3. The triangle and the square marks are the locations of the microtremor array and the V1-H/V measurements.

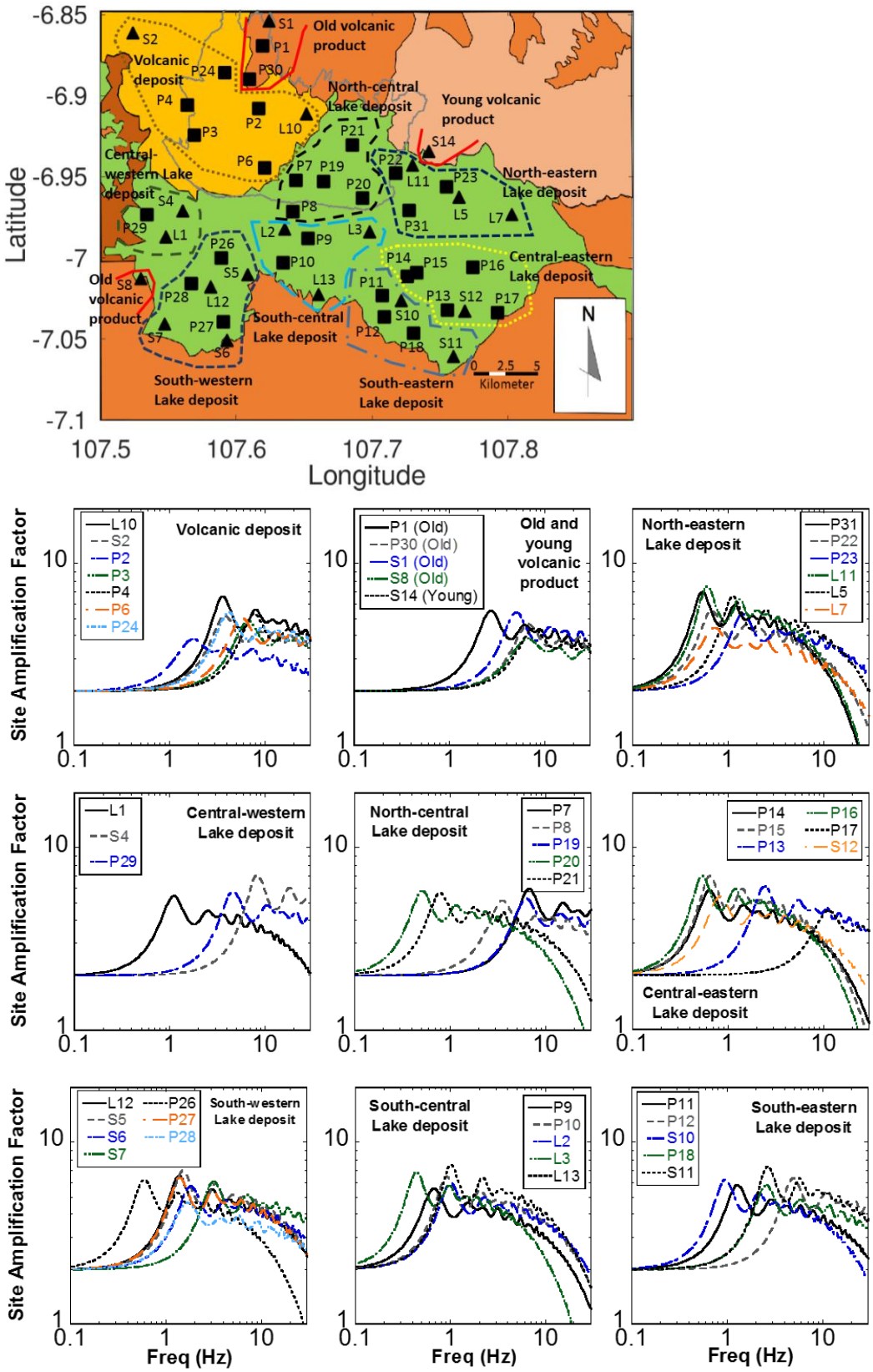

Figure 6.3 Site amplification factor of estimated Vs profile at the array and the V1-H/V measurements in each geological unit in the Bandung basin. Site amplification factor at L4, L6, L15, S3, and S9 are shown in Figure 6.1 and excluded in this figure. The top figure illustrated the location of each measurement point.

Table 6.3 Average and standard deviation of the surface S-wave velocities, and several time-averaged S-wave velocities for the measurement points located at each geological unit in the Bandung basin. The analysed time-averaged S-wave velocities consist of the averaged S-wave velocity in the top 30 m, 20 m, 10 m, and 5 m.

Geology	Number of sites	Vs30 ± Std (m/s)	Vs20 ± Std (m/s)	Vs10 ± Std (m/s)	Vs5 ± Std (m/s)	V1 ± Std (m/s)
Lake deposit	37	184 ± 75	161 ± 64	132 ± 44	115 ± 33	96 ± 25
Volcanic deposit	7	298 ± 41	255 ± 38	199 ± 30	167 ± 29	130 ± 34
Old volcanic product	4	313 ± 55	270 ± 52	212 ± 43	180 ± 39	144 ± 36
Young volcanic product	1	370	327	255	212	164

Furthermore, we evaluate a relation between the Vs30s and the site amplification factors in the Bandung basin. Figure 6.4 shows the relationship of Vs30s and the averaged amplification factors at frequencies of 0.4 to 10 Hz for each geological unit. We also compare the averaged site amplifications with the V1s and other time-averaged S-wave velocities, such as the average Vs to depths of 5 m, 10 m, and 20 m (Vs5, Vs10, Vs20) to investigate the potential of these velocity parameters as proxies for the site amplification in the basin. The appropriateness of each velocity parameters to expect the amplification is evaluated by calculating a linear regression between the velocity parameters and the averaged amplifications. We observed high coefficient correlations (CR) of the regression lines with a value of more than 0.9 for the velocity parameters of Vs30, Vs20, Vs10, and Vs5 in the lake deposit and the old-young volcanic product areas. Meanwhile in the volcanic deposit area, the high CR value with value higher than 0.9 can be only observed for the parameters of Vs20s and Vs10s. The highest and the lowest CR values are obtained from Vs10s, and V1 parameters, respectively. This result suggests that information of the S-wave velocity profiles at depths shallower than 30 m is sufficient for expecting the site amplifications in the Bandung basin. Consequently, the usage of the proposed method become appropriate because the method could provide

an accurate shallow Vs profile as mentioned in the numerical tests and also in the Vs30 comparison to the conventional method. The results of the high correlations between the Vs10s and the site amplifications in the basin is needed to be confirmed in the future task by considering actual site amplification observation.

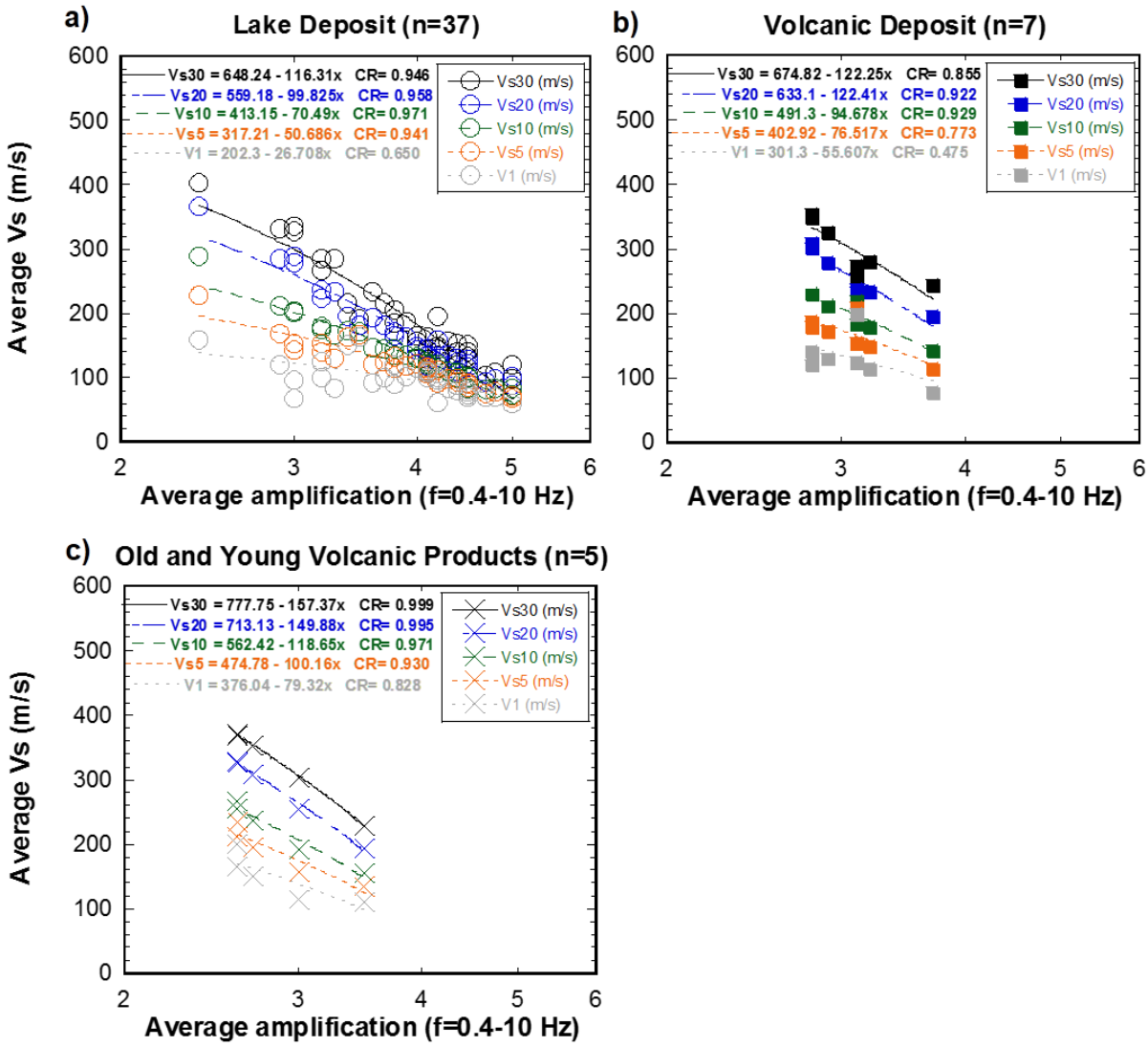

Figure 6.4 Relationship of the surface S-wave velocity, the time-averaged S-wave velocities in the top 5 m, 10 m, 20 m, and 30 m with the average site amplification factor in frequency of 0.4 to 10 Hz at the sites located on **a)** lake deposit, **b)** volcanic deposit, and **c)** old and young volcanic products as represented by circle, filled square, and cross marks, respectively. Gray, orange, green, blue, and black dashed lines correspond to the regression lines obtained by using the surface S-wave velocity, the average S-wave velocities in the top 5, 10, 20, and 30 m, respectively. The coefficient correlation (CR) for each regression line are shown on the upper part of each figure

6.4 Comparison with the previous PGA map

In this section, we compare our results with the previous study from Handayani et al., (2009). The previous study provided the horizontal peak ground acceleration (PGA) map in the basin using an attenuation relationship equation. However, the required Vs30 for the equation was derived from an empirical Vs30-surface geological relation. Therefore, we can compare our estimated Vs30s with their Vs30s, and perform PGA comparison using the Vs30 in each study.

The comparison of the Vs30s on the surface geological map of the basin are illustrated in Figures 6.5. The Vs30 used in their study is defined from the surface geology condition as shown in the bottom part of Figure 6.5. The area covered with lake deposit is classified by group D with a Vs30 range from 180 to 360 m/s, whereas the volcanis deposit areas are classified by groups B, BC, and CD with a Vs30 range of higher than 760 m/s, 555 to 1000 m/s, and 270 to 555 m/s, respectively. We observe that our results provided more various Vs30s than the previous Vs30s in lake deposit area, and lower Vs30s than the previous Vs30s in the volcanic deposit areas.

For the quantitative comparison, we make a cross plot of the our estimated Vs30s and the previous Vs30s as shown in Figure 6.6. The x-axis corresponds to the assumed Vs30s in the previous study, while the y-axis represents the our estimated Vs30s. In the plot, our estimated Vs30 at each site was put in the middle value of each Vs30 category in the previous study. The averaged Vs30s and its standard deviation for each Vs30 category is 184 ± 75 m/s, 369 m/s, 307 ± 46 m/s, and 294 ± 51 m/s for groups D, CD, BC, and B, respectively. On the other hand, the Vs30 ranges for groups D, CD, BC, and B in the previous study are 270 ± 90 m/s, 412.5 ± 142.5m/s, 777.5 ± 222.5 m/s, and higher than 760 m/s, respectively. This result confirms that our estimated Vs30s are

lower than the Vs30s defined in previous study, especially a large difference is observed in the Vs30 comparison at the groups BC and B.

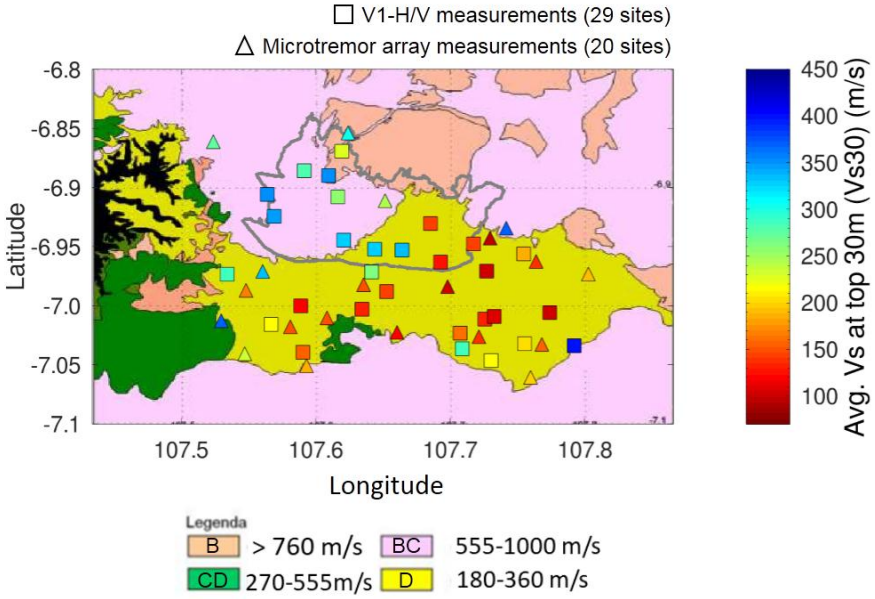

Figure 6.5 Comparison of Vs30s in this study and the previos study by Handayani et al. (2009). The triangle and square marks with colorscale on the right side are the obtained Vs30 from the microtremor array (conventional method) and the V1-H/V measurements (proposed method) in this study. The background colors as described in the colorscale on the bottom side are Vs30 classification in Handayani et al. (2009) derived from the surface geological condition in the basin.

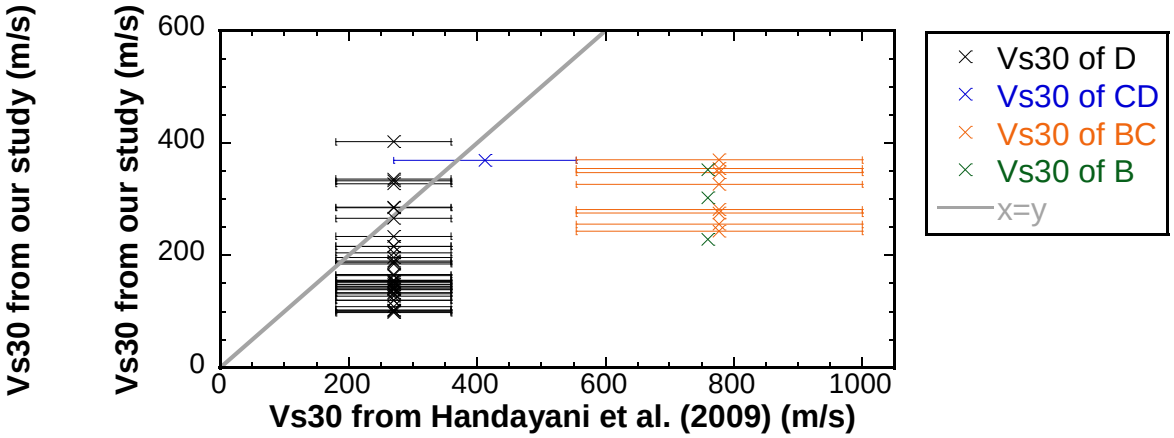

Figure 6.6 Cross-plot of Vs30 comparison between our result and the previous study by Handayani et al (2009). Black, blue, orange, and green colors correspond to the Vs30 classification of group D, CD, BC, and B that used in Handayani et al. (2009), respectively. Error bar in horizontal axis correspond to the range of Vs30 used in Handayani et al. (2009) for each categories. Cross marks indicate the Vs30 comparison between our result and the middle value of the Vs30 range for each category in Handayani et al. (2009). There is no error-bar on Vs30 range of group B due to it only has a minimum value (see Figure 6.5). Solid gray line indicate similiar Vs30 value between our result and the previous study.

We further utilize our estimated Vs30s to calculate the PGA values in the basin by using the same attenuation relationship equation to the previous study. The PGA map in the previous study was established by using the attenuation relationship proposed by Boore et al. (1997):

$$\log Y = b_1 + b_2 (M - 6) + b_3 (M-6)^2 + b_5 \log r + b_v (\log Vs30 - \log V_A) \ldots (6.2)$$

where Y is a horizontal acceleration with unit of g. M is the moment magnitude of an earthquake. $r = \sqrt{d^2 + h^2}$ is distance in km, with d is epicentral distance, h is fictitious depth. Vs30 is averaged S-wave velocity at depths of 0 to 30 m. b_1, b_2, b_3, b_5, h, b_v, V_A are the coefficients that have been determined in Boore et al. (1997) and summarized in Douglas (2001) with values of b_1=-0.105, b_2=0.229, b_3=0, b_5=-0.778, h=5.57, b_v=-0.371, V_A=1400 for the peak ground acceleration case. The previous study simulated an earthquake along the Lembang fault with a moment magnitude (M) of 6.0. In order to compare with the previous result of the PGA distribution, we set all the parameters in the empirical equation using the same value, except the parameter of Vs30.

The comparison of the PGA map in Handayani et al. (2009) and the estimated PGA value using the estimated Vs30s at the measurement points is shown in Figure 6.7. In general, characteristics of PGA value distributions are controlled by the epicentral distances and the Vs30s of the soil condition. We observe a high PGA in the region that close to the source point and the PGA decreases by increasing the distance to the source. Moreover, a higher PGA value can be observed in the area with a low Vs30 than that located in a high Vs30 region.

Since Vs30s in the previous study's map are set depending on the surface geological condition, we observed a gradual decrement of the PGA values in the previous study which is proportional to the epicenter distances in the volcanic region in

the northern part and at the lake deposit area in the central part of the basin. Even though spatial variation of the Vs30s for each category in the previous study is not described, the gradual decrement of the PGA values in the previous study may indicate the usage of a constant Vs30 for each geological region. We also observed a sudden increment of the PGA value in the previous map in boundaries area of the volcanic region and the lake deposit in the central part due to changing of the Vs30s from a high value in the volcanic region area to a low Vs30 in the lake deposit area. The high PGA region having the lake deposits is observed in the north-central part with a PGA of 0.2 g.

In the other hand, the distribution of our PGA values at the measurement points is not strongly depended on the epicentral distances due to the various values of the estimated Vs30s in our results even in the same surface geological condition. For example, we observed the different PGA values at P2 and P4 sites even though they are located in the volcanic deposit area with similar epicentral distances. The similar case can be found at S4 and P20 sites that located in the lake deposit region. The PGA at P20 is higher than that at S4 even though their epicentral distance is almost same. The most prominent differences in the PGA map comparison show that the PGA values in our study are higher than those of the previous PGA map. This is due to our estimated Vs30s lower than that used in the previous study. We found the higher PGA values in our result than the previous one at all the measurement points in the volcanic region. We also found in the volcanic region that the high PGA zone with values higher than 0.2 g indicated by orange to red colors are concentrated in areas close to the epicenter in the previous study. However, our result shows that the high PGA values with values higher than 0.2 g are still found in the far regions such as at S2, P24, P30, P2, and L10 sites. Furthermore, we found in our results that the PGA values higher than 0.18 g area are seen at P26 in the western part, at L2, P9, P10 in the central part, and at P21, P22, P20,

L3, L11, P31 in the eastern part. On contrary, the PGAs higher than 0.18 g are only found in the north-central part covered with the lake deposit in the previous map. Other prominent differences can be observed in the central part at longitudes of 107.65 and latitudes of -6.95. The previous PGA map shows a reduction of the PGA from 0.2 g in the central part to 0.15 g value in the southern part. However, our results indicate an increment of the PGA from 0.15 g at P7 and P8 in the central part to 0.18 g at L2 in the southern part.

Furthermore, the quantitative comparison of the PGA map is illustrated by a cross-plot in Figure 6.8. Our results provide wider PGA distributions than the previous PGA distribution, since the spatial variation of the Vs30s is accommodated by actual observations with the proposed method. Moreover, we observe that most of our estimated PGAs overestimate with values 1.3 times higher than those of the previous study. Therefore, we also disclose a higher potential of the seismic hazard in the basin as compared to the previous study.

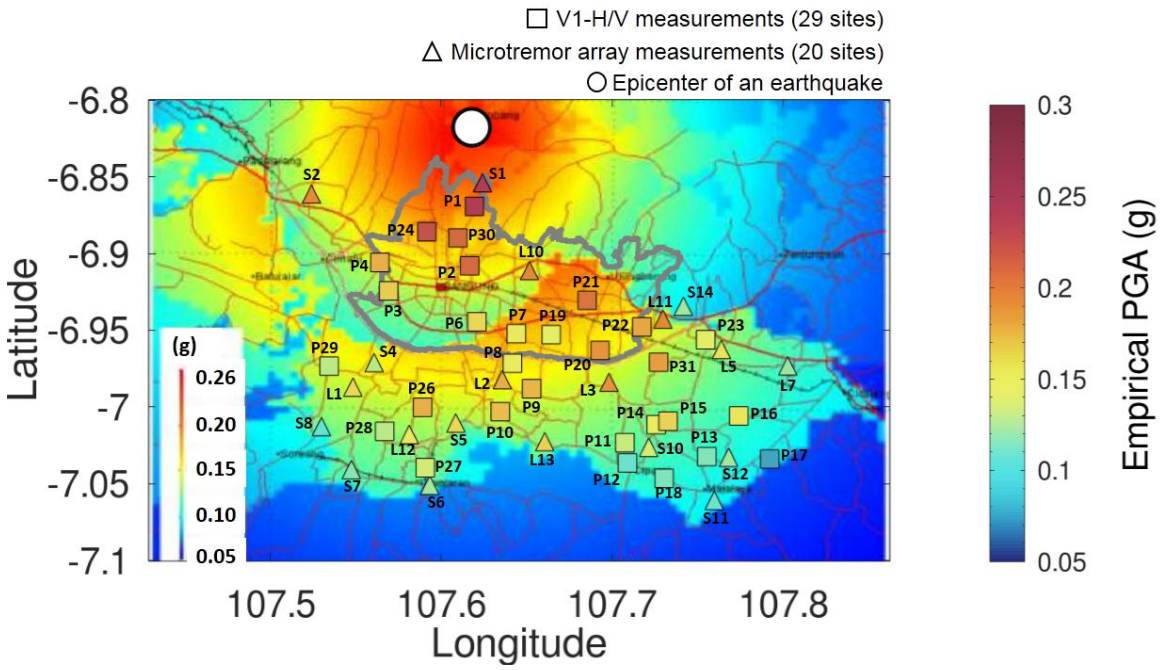

Figure 6.7 Comparison of the PGA values from our study and the previous study in Handayani et al. (2009). The triangles and squares marks are correspond with the PGA values considering the Vs30 of the estimated Vs profile from the array and the V1-H/V measurements. The background color corresponds with the PGA values obtained in the previous study in Handayani et al. (2009). White circle mark correspond the epicenter of the earthquake.

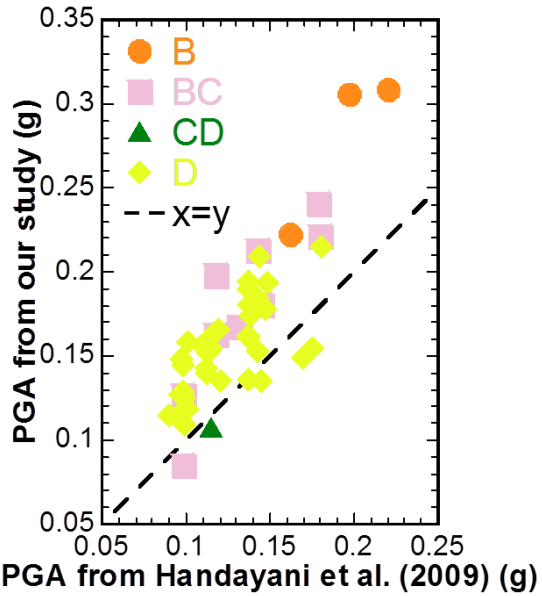

Figure 6.8 Cross-plot of PGA comparison between our result and provided in Handayani et al (2009). Orange, pink, green, and yellow marks indicate the PGA comparison located at B, BC, CD, and D groups of the Vs30 categories in Handayani et al. (2009), respectively. The dashed line indicates similar PGA value between our result and the previous study.

Chapter 7 Conclusions and future tasks

7.1 Conclusions

7.2 Future tasks

7.1 Conclusions

We have proposed a simplified method to estimate 1D S-wave velocity (Vs) profiles in the Bandung basin, Indonesia, using observed surface S-wave velocities (V1) and a peak frequency of microtremor H/Vs. In the proposed method, we represent a profile using a linear velocity function with a depth over a bedrock layer that has a given constant S-wave velocity. Therefore, the profile can be parameterized with a V1 and a velocity gradient of the velocity function. Since a V1 is provided from a field measurement, a profile is uniquely estimated by determining a gradient from an agreement of the peak frequencies between an observed H/V and a theoretical ellipticity of the fundamental mode Rayleigh wave. Since the data acquisition for the proposed method requires less number of the instruments, the method can be conducted in shorter measuement time than the conventional method.

We have evaluated the applicability of the proposed method through the numerical tests using the borehole profiles in the Bandung basin. The estimated Vs profiles from the proposed method are in a good agreement to the borehole profiles with the average relative differences (R-values) below 20%. The appropriateness of the Vs profiles estimated from the proposed method is also confirmed because those profiles are similar to the ones obtained from the conventional method using phase velocity data. The different assumption of the bedrock velocities causes a slight difference in the estimated Vs profiles. A bedrock velocity difference of 200 m/s to the true bedrock velocity causes an additional R-value below 20% to the estimated profile. However, we observed that the influence of the different bedrock velocities is insignificant for the estimated profiles at shallower depths. Contamination of noise in the ellipticity peak frequency has more significant influence to the errors of the estimated profile than noise contamination in the V1. We also show the limitation of the proposed method in the numerical tests. The

proposed method could not retrieve an appropriate bedrock depth. It is also indicated that the method has a difficulty to retrieve the true model having a thick layer with a constant velocity. We can identify the existence of such thick constant velocity layer from the plateau feature of the observed Rayleigh-wave phase velocity. The unappropriateness of the profile representation using the linear function can be understood by the phase velocity comparison between the observed phase velocity and the theoretical one from the estimated profile. Therefore, available phase velocity sample can be used to judge the applicability of the method.

The appropriateness of the proposed method in the Bandung basin has been evaluated using the observed Rayleigh-wave phase velocities from the conventional microtremor array measurements. We observed that the observed phase velocities at 23 of 25 sites can be well explained by the theoretical phase velocities using the linear profile representation. We also found the appropriateness of the bedrock velocity in the basin using 500 m/s from the evaluation of the observed phase velocities.

We then applied the proposed method at 29 sites in the basin with the actual V1 and H/V measurements. The profiles from the proposed method have a good agreement with the profiles obtained from the conventional method with R values less than 20%. We found that the profiles estimated from proposed method have a good accuracy to provide the Vs30s because the appropriateness of the linear velocity function with a depth can be well satisfied in the basin. The proposed method also can provide a profile with an accurate fundamental peak frequency of the site amplification because the estimated profile is derived from the agreement in the observed H/V peak. Moreover, the profile from the proposed method can well anticipate the fundamental peak amplitude of the site amplification since the velocity contrast between the bedrock and the surface are provided in the proposed method.

The estimated Vs profiles from the array explorations and the V1-H/V measurements were used to delineate the site amplification factor features in the basin. The low Vs30 zone having values below 150 m/s and the fundamental peak frequencies below 1 Hz are found in the central-eastern part of the basin covered with the lake deposits. Meanwhile, higher Vs30s with values above 250 m/s with the site amplification characterized by peak frequencies of 2 to 8 Hz and amplification factor below 6 are observed in the volcanic region in the northern part and in the edge of the basin. We also found that our estimated Vs30s are lower than those assumed in the previous study in Handayani et al (2009). Therefore, our results reveal a higher potential of the seismic hazard in the Bandung basin than the previous study.

In order to apply the proposed method at the other areas, the appropriateness of a Vs profile representation using the linear function of S-wave velocity depth distribution must be confirmed from observed Rayleigh-wave phase velocities, or borehole profiles at a few representative sites in the area before the further usage of the proposed method.

7.2 Future tasks

We consider several future tasks from the results of this study. There are some regions in the Bandung basin that are not covered by the measurement points, such as the western part of the basin and the surrounding area of the Lembang fault. Therefore, we consider increasing the V1-H/V measurements to provide Vs profiles of the basin structure for the purpose of ground motion predictions. Futhermore, we found in this study that the Vs10 can be used for the site amplification proxies in the basin. Hence, further investigation to confirm the usage of Vs10 as amplification proxies is considerd by using actual site amplification observation.

We also consider to apply the proposed method in other areas, especially in areas that having P-S logging data to evaluate the appropriate profile representation. Since

many regions in Indonesia are lacking in the shallow S-wave velcoity profiles information, the future study to apply of the proposed method in other regions in Indonesia will be considered.

We consider to broaden the application of the proposed method from the current limitation. For example, the feature of the proposed method for bedrock depth estimation will be investigated.

References

Afnimar. (2014). Estimation of SH-wave amplification in the bandung basin using Haskell‟s method. *Journal of Engineering and Technological Sciences*, *46 B*(1), 93–101. https://doi.org/10.5614/j.eng.technol.sci.2014.46.1.6

Afnimar, Yulianto, E., & Rasmid. (2015). Geological and tectonic implications obtained from first seismic activity investigation around Lembang fault. *Geoscience Letters*, *2*(1). https://doi.org/10.1186/s40562-015-0020-5

Aki, K. (1957). Space and time spectra of stationary stochastic waves, with special reference to microtremors. *Bulletin of the Earthquake Research Institute*, *35*, 415–456.

Al-Chalabi, M. (1997). Time-depth relationships for multilayer depth conversion. *Geophysical Prospecting*, *45*(4), 715–720. https://doi.org/10.1046/j.1365-2478.1997.520293.x

Arai, H, & Tokimatsu, K. (2000). Effects of Rayleigh and Love waves on microtremor H/V spectra, paper presented at 12th World Conference on Earthquake Engineering. *NZ Soc. for Earthquake Eng, Auckland*.

Badan Nasional Penanggulangan Bencana (BNBP) (2014). Rencana Strategis Badan Nasional Penanggulangan Bencana 2015–2019.

Bandung City Statistics. (2021). *Populations of Bandung city in 2019*. https://bandungkota.bps.go.id/statictable/2021/03/18/1437/jumlah-penduduk-dan-keluarga-menurut-kecamatan-di-kota-bandung-2018-dan-2019.html

Boore, D M, Joyner, W. B., & Fumal, T. E. (1993). *Estimation of response spectra and peak accelerations from Western North American earthquakes: An interim report Part 2*. https://doi.org/10.3133/OFR93509

Boore, David M. (2003). Simulation of ground motion using the stochastic method. *Pure and Applied Geophysics*, *160*(3–4), 635–676. https://doi.org/10.1007/PL00012553

Boore, David M, Joyner, W. B., & Fumal, T. E. (1997). Equations for Estimating Horizontal Response Spectra and Peak Acceleration from Western North American Earthquakes: A Summary of Recent Work. *Seismological Research Letters*, *68*(1), 128–153. https://doi.org/10.1785/gssrl.68.1.128

Brahmantyo, B. (2005). *Geologi cekungan Bandung*. Institut Teknologi Bandung (in Indonesian).

Bronto, S. (2006). Stratigrafi gunung api daerah Bandung Selatan, Jawa Barat. *Indonesian Journal on Geoscience*, *1*(2), 89–101. https://doi.org/10.17014/ijog.vol1no2.20064

Building Seismic Safety Council (2004). *NEHRP Recommended Provisions for Seismic Regulations for New Buildings and Other Structures (FEMA 450)*. National Institute of Building Sciences Washington, DC.

Bullen, K. E. (1965). Allowance for seismic velocity gradient in a horizontally layered flat Earth. *Geophysical Journal International*, *10*(1), 45–49.

Capon, J. (1969). High-resolution frequency-wavenumber spectrum analysis. *Proceedings of the IEEE*, *57*(8), 1408–1418. https://doi.org/10.1109/PROC.1969.7278

D‟Amico, V., Picozzi, M., Baliva, F., & Albarello, D. (2008). Ambient noise measurements for preliminary site-effects characterization in the urban area of Florence, Italy. *Bulletin of the Seismological Society of America*, *98*(3), 1373-1388.

Dal Moro, G. (2014). *Surface wave analysis for near surface applications*. Elsevier.

Dam, M. A. C., & Suparan, P. (1992). *Geology of the Bandung Basin. Report with the 1: 50.000 Quaternary geological map of the Bandung Basin*.

Dam, M. A. C., Suparan, P., Nossin, J. J., Voskuil, R. P. G. A., & Group, G. T. L. (1996). A chronology for geomorphological developments in the greater Bandung area, West-Java, Indonesia. *Journal of Southeast Asian Earth Sciences*, *14*(1–2), 101–115. https://doi.org/10.1016/S0743-9547(96)00069-4

Daryono, M. R., Natawidjaja, D. H., Sapiie, B., & Cummins, P. (2019). Earthquake Geology of the Lembang Fault, West Java, Indonesia. *Tectonophysics*, *751*(December 2018), 180–191. https://doi.org/10.1016/j.tecto.2018.12.014

Delinom, R. M. (2009). Structural geology controls on groundwater flow: Lembang fault case study, West Java, Indonesia. *Hydrogeology Journal*, *17*(4), 1011–1023. https://doi.org/10.1007/s10040-009-0453-z

Desiani, A., & Rahardjo, P. P. (2017). Characterization of Bandung Soft Clay. *Electronic Journal of Geotechnical Engineering*, *22*(11), 4377–4393.

Douglas, J. (2001). A comprehensive worldwide summary of strong-motion attenuation relationships for peak ground acceleration and spectral ordinates (1969 to 2000). *ESEE Report*, *01–1*, 1–138.

Fäh, D., Kind, F., & Giardini, D. (2001). A theoretical investigation of average HIV ratios. *Geophysical Journal International*, *145*(2), 535–549. https://doi.org/10.1046/j.0956-540X.2001.01406.x

Fäh, Donat, Kind, F., & Giardini, D. (2003). Inversion of local S-wave velocity structures from average H/V ratios, and their use for the estimation of site-effects. *Journal of Seismology*, *7*(4), 449–467. https://doi.org/10.1023/B:JOSE.0000005712.86058.42

Foti, S., Hollender, F., Garofalo, F., Albarello, D., Asten, M., Bard, P. Y., Comina, C., Cornou, C., Cox, B., Di Giulio, G., Forbriger, T., Hayashi, K., Lunedei, E., Martin, A.,

Mercerat, D., Ohrnberger, M., Poggi, V., Renalier, F., Sicilia, D., & Socco, V. (2018). Guidelines for the good practice of surface wave analysis: a product of the InterPACIFIC project. In *Bulletin of Earthquake Engineering* (Vol. 16, Issue 6). https://doi.org/10.1007/s10518-017-0206-7

Foti, S., Lai, C., Rix, G. J., & Strobbia, C. (2014). Surface Wave Methods for Near-Surface Site Characterization. In *Surface Wave Methods for Near-Surface Site Characterization*. https://doi.org/10.1201/b17268

Foti, S., Parolai, S., Albarello, D., & Picozzi, M. (2011). Application of Surface-Wave Methods for Seismic Site Characterization. *Surveys in Geophysics*, *32*(6), 777–825. https://doi.org/10.1007/s10712-011-9134-2

Glass, C. E. (1989). A focus on the September 1985 Michoacan earthquakes. *International Journal of Mining and Geological Engineering*, *7*(1), 1–8. https://doi.org/10.1007/BF01552834

Govindaraju, L., & Bhattacharya, S. (2012). Site-specific earthquake response study for hazard assessment in Kolkata city, India. *Natural Hazards*, *61*(3), 943–965. https://doi.org/10.1007/s11069-011-9940-3

Grutas, R., & Yamanaka, H. (2012). Shallow shear-wave velocity profiles and site response characteristics from microtremor array measurements in Metro Manila, the Philippines. *Exploration Geophysics*, *43*(4), 255–266. https://doi.org/10.1071/EG12031

Hall, R. (2002). Cenozoic geological and plate tectonic evolution of SE Asia and the SW Pacific: Computer-based reconstructions, model and animations. *Journal of Asian Earth Sciences*, *20*(4), 353–431. https://doi.org/10.1016/S1367-9120(01)00069-4

Handayani, L., Mulyadi, D., Wardhana, D. D., & Nur, W. H. (2009). Percepatan Pergerakan

Tanah Maksimum Daerah Cekungan Bandung: Studi Kasus Gempa Sesar Lembang. *Jurnal Geologi Dan Sumberdaya Mineral*, *19*(5), 333–337.

Haskell, N. A. (1953). The dispersion of surface waves on multilayered media*. *Bulletin of the Seismological Society of America*, *43*(1), 17–34.

Hauksson, E., Jones, L. M., & Hutton, K. (1995). The 1994 Northridge earthquake sequence in California: seimological and tectonic aspects. *Journal of Geophysical Research*, *100*(B7). https://doi.org/10.1029/95jb00865

Holzer, T. L., Bennett, M. J., Noce, T. E., & Tinsley III, J. C. (2005). Shear-wave velocity of surficial geologic sediments in northern California: statistical distributions and depth dependence. *Earthquake Spectra*, *21*(1), 161–177.

Hudson, D. E., & Housner, G. W. (1958). An analysis of strong-motion accelerometer data from the San Francisco earthquake of March 22, 1957. *Bull. Seismol. Soc. Am.*, *48*(July), 253-268.

Ibs-von Seht, M., & Wohlenberg, J. (1999). Microtremor measurements used to map thickness of soft sediments. *Bulletin of the Seismological Society of America*, *89*(1), 250-259.

Jafari, M. K., Ghayamghamian, M. R., Davoodi, M., Kamalian, M., & Sohrabi-Bidar, A. (2005). Site effects of the 2003 Bam, Iran, earthquake. *Earthquake Spectra*, *21*(SUPPL. 1), 125–136. https://doi.org/10.1193/1.2098266

Karagoz, O., Chimoto, K., Citak, S., Ozel, O., Yamanaka, H., & Hatayama, K. (2015). Estimation of shallow S-wave velocity structure and site response characteristics by microtremor array measurements in Tekirdag region, NW Turkey. *Earth, Planets and Space*, *67*(1), 1–17. https://doi.org/10.1186/s40623-015-0320-1

Katili, J. A. (2018). *Plate Tectonics of Indonesia with Special Reference to the Sundaland Area*. *June 1972*, 2006. https://doi.org/10.29118/ipa.1921.57.61

Kitsunezaki, C., Goto, N., Kobayashi, Y., Ikawa, T., Horike, M., Saito, T., Kurota, T., Yamane, K., & Okuzumi, K. (1990). Estimation of P- and S- wave velocities in deep soil deposits for evaluating ground vibrations in earthquake. *Journal of Japan Society for Natural Disaster Science*, *9*(3), 1–17.

Konno, K., & Ohmachi, T. (1998). Ground-motion characteristics estimated from spectral ratio between horizontal and vertical components of microtremor. *Bulletin of the Seismological Society of America*, *88*(1), 228–241.

Kramer, S. L. (1996). Geotechnical earthquake engineering. Upper Suddle RIver, New Jersey, Prentice Hall (p. 376).

Lontsi, A. M., Ohrnberger, M., Krüger, F., & Sánchez-Sesma, F. J. (2016). Combining surface-wave phase-velocity dispersion curves and full microtremor horizontal-to-vertical spectral ratio for subsurface sedimentary site characterization. *Interpretation*, *4*(4), SQ41–SQ49. https://doi.org/10.1190/INT-2016-0021.1

Meilano, I., Abidin, H. Z., Andreas, H., Gumilar, I., Sarsito, D., Rahma, H., Rino, Harjono, H., Kato, T., Kimata, F., & Fukuda, Y. (2012). Slip rate estimation of the lembang fault west java from geodetic observation. *Journal of Disaster Research*, *7*(1), 12–18. https://doi.org/10.20965/jdr.2012.p0012

Ohta, Y., & Goto, N. (1978). Empirical shear wave velocity equations in terms of characteristic soil indexes. *Earthquake Engineering & Structural Dynamics*, *6*(2), 167–187. https://doi.org/10.1002/eqe.4290060205

Okada, H. (2003). The Microtremor Survey Method. *Geophysical Monograph Series*, *12*.

Özmen, Ö. T., Yamanaka, H., Chimoto, K., Çeken, U., Alkan, M. A., Tekin, K., & Ateş, E. (2017). Microtremor exploration for shallow S-wave velocity profiles at stations in local strong motion network in Bursa, Yalova, and Kocaeli in north-western Turkey. *Exploration Geophysics*, *48*(3), 255–263. https://doi.org/10.1071/EG16036

Park, C B, Miller, R. D., Ryden, N., Xia, J., & Ivanov, J. (2005). Combined Use of Active and Passive Surface Waves. *Journal of Environmental and Engineering Geophysics*, *10*(3), 323–334. https://doi.org/10.2113/JEEG10.3.323

Park, Choon B., Miller, R. D., & Xia, J. (1999). Multichannel analysis of surface waves. *Geophysics*, *64*(3), 800–808. https://doi.org/10.1190/1.1444590

Parolai, S., Bormann, P., & Milkereit, C. (2002). New relationships between Vs, thickness of sediments, and resonance frequency calculated by the H/V ratio of seismic noise for the cologne area (Germany). *Bulletin of the Seismological Society of America*, *92*(6), 2521–2527. https://doi.org/10.1785/0120010248

Parolai, Stefano, Maesano, F. E., Basili, R., Silacheva, N., Boxberger, T., & Pilz, M. (2019). Fingerprint Identification Using Noise in the Horizontal-to-Vertical Spectral Ratio: Retrieving the Impedance Contrast Structure for the Almaty Basin (Kazakhstan) . In *Frontiers in Earth Science* (Vol. 7, p. 336). https://www.frontiersin.org/article/10.3389/feart.2019.00336

Pranata, B., Yudistira, T., Widiyantoro, S., Brahmantyo, B., Cummins, P. R., Saygin, E., Zulfakriza, Z., Rosalia, S., & Cipta, A. (2020). Shear wave velocity structure beneath Bandung basin, West Java, Indonesia from ambient noise tomography. *Geophysical Journal International*, *220*(2), 1045–1054. https://doi.org/10.1093/gji/ggz493

Quispe, S., Chimoto, K., Yamanaka, H., Tavera, H., Lazares, F., & Aguilar, Z. (2014). Estimation of S-wave velocity profiles at lima city, peru using microtremor arrays.

Journal of Disaster Research, *9*(6), 931–938. https://doi.org/10.20965/jdr.2014.p0931

Satoh, T., Kawase, H., & Matsushima, S. (2001). Estimation of S-wave velocity structures in and around the Sendai Basin, Japan, using array records of microtremors. *Bulletin of the Seismological Society of America*, *91*(2), 206–218. https://doi.org/10.1785/0119990148

Scherbaum, F., Hinzen, K. G., & Ohrnberger, M. (2003). Determination of shallow shear wave velocity profiles in the Cologne, Germany area using ambient vibrations. *Geophysical Journal International*, *152*(3), 597-612.

Slotnick, M. M. (1936). On seismic computations, with applications, II. *Geophysics*, *1*(3), 299–305. https://doi.org/10.1190/1.1437111

Stambouli, A. B., Zendagui, D., Bard, P. Y., & Derras, B. (2017). Deriving amplification factors from simple site parameters using generalized regression neural networks: implications for relevant site proxies. *Earth, Planets and Space*, *69*(1), 1-26.

Surahman, A. (2000). Earthquake Vulnerability Evaluation of Building in Bandung Municipality. *12Wcee*, *0182*, 1–7. http://www.iitk.ac.in/nicee/wcee/article/0182.pdf

Syalsabilla, L. L., Haryanto, I., & Sukiyah, E. (2020). The Levels of Lembang Fault Activity Based on Geomorphic Indexes on Around The Cikapundung Watershed, West Java. *Journal of Geological Sciences and Applied Geology*, *4*(1), 1–9.

Tokimatsu, K., Tamura, S., & Kojima, H. (1992). Effects of multiple modes on Rayleigh wave dispersion characteristics. *Journal of geotechnical engineering*, *118*(10), 1529-1543.

Trifunac, M. D. (1990). How to model amplification of strong earthquake motions by local soil and geologic site conditions. *Earthquake Engineering & Structural Dynamics*, *19*(6), 833–846. https://doi.org/10.1002/eqe.4290190605

Tsuda, K., Steidl, J., Archuleta, R. J., & Assimaki, D. (2006). Site-response estimation for the 2003 Miyagi-Oki earthquake sequence considering nonlinear site response. *Bulletin of the Seismological Society of America*, *96*(4 A), 1474–1482. https://doi.org/10.1785/0120050160

Tuan, T. T., Scherbaum, F., & Malischewsky, P. G. (2011). On the relationship of peaks and troughs of the ellipticity (H/V) of Rayleigh waves and the transmission response of single layer over half-space models. *Geophysical Journal International*, *184*(2), 793–800. https://doi.org/10.1111/j.1365-246X.2010.04863.x

United States Geological Survey (USGS), (2020). *Indonesian earthquake catalog in 2010-2020*. https://earthquake.usgs.gov/earthquakes/search/

Vrettos, C. (1996). Simple inversion procedure for shallow seismic refraction in continuously nonhomogeneous soils. *Soil Dynamics and Earthquake Engineering*, *15*(6), 381-386.

Wang, S. Y., Shi, Y., Jiang, W. P., Yao, E. L., & Miao, Y. (2018). Estimating site fundamental period from shear-wave velocity profile. *Bulletin of the Seismological Society of America*, *108*(6), 3431–3445. https://doi.org/10.1785/0120180103

Wang, S. Y., & Wang, H. Y. (2016). Site-dependent shear-wave velocity equations versus depth in California and Japan. *Soil Dynamics and Earthquake Engineering*, *88*, 8–14. https://doi.org/10.1016/j.soildyn.2016.05.001

Wathelet, M., Jongmans, D., & Ohrnberger, M. (2004). Surface-wave inversion using a direct search algorithm and its application to ambient vibration measurements. *Near Surface Geophysics*, *2*(4), 211–221.

Wells, D. L., & Coppersmith, K. J. (1994). New empirical relationships among magnitude, rupture length, rupture width, rupture area, and surface displacement. *Bulletin of the*

Seismological Society of America, *84*(4), 974–1002.

Wills, C. J., Petersen, M., Bryant, W. A., Reichle, M., Saucedo, G. J., Tan, S., Taylor, G., & Treiman, J. (2000). A site-conditions map for California based on geology and shear-wave velocity. *Bulletin of the Seismological Society of America*, *90*, 187–208. https://doi.org/10.1785/0120000503

Xia, J., Miller, R. D., Park, C. B., Hunter, J. A., & Harris, J. B. (2000). Comparing shear-wave velocity profiles from MASW with borehole measurements in unconsolidated sediments, Fraser River Delta, BC, Canada. *Journal of Environmental & Engineering Geophysics*, *5*(3), 1–13.

Yamamizu, F., Goto, N., Ohta, Y., & Takahashi, H. (1983). Attenuation of shear waves in deep soil deposits as revealed by down-hole measurements in the 2,300 meter-borehole of the Shimohsa observartory, Japan. *Journal of Physics of the Earth*, *31*(2), 139–157. https://doi.org/10.4294/jpe1952.31.139

Yamanaka, H., Takemura, M., Ishida, H., & Niwa, M. (1994). Characteristics of long-period microtremors and their applicability in exploration of deep sedimentary layers. *Bulletin - Seismological Society of America*, *84*(6), 1831–1841. https://doi.org/10.1016/0148-9062(95)99176-x

Zaineh, H. E., Yamanaka, H., Dakkak, R., Khalil, A., & Daoud, M. (2012). Estimation of Shallow S-Wave Velocity Structure in Damascus City, Syria, Using Microtremor Exploration. *Soil Dynamics and Earthquake Engineering*, *39*, 88–99. https://doi.org/10.1016/j.soildyn.2012.03.003

Zeng, X. (1996). A simple procedure to calculate the fundamental frequency of horizontal soil layers. *Geotechnique*, *46(4)*, 757–760.